**The Dissertation Committee for Jing Yang Certifies that this is the approved version of the following dissertation:**

# Sound Velocity Profiles of Lower Mantle Minerals: Implications to Geophysics and Geochemistry of the Deep Earth

**Committee:**

Jung-Fu Lin, Supervisor

Stephen P. Grand

Donald D. Blankenship

John C. Lassiter

Xiaoqin Li

# Sound Velocity Profiles of Lower Mantle Minerals: Implications to Geophysics and Geochemistry of the Deep Earth

**by**

**Jing Yang, B.S.; M.S.**

**Dissertation**

Presented to the Faculty of the Graduate School of

The University of Texas at Austin

in Partial Fulfillment

of the Requirements

for the Degree of

**Doctor of Philosophy**

**The University of Texas at Austin**

**May 2017**

# Dedication

To my husband Ian En-Hsu Yen

and my parents Xinhong Yang and Xia Min

## Acknowledgements

Firstly, I would like to thank my supervisor Jung-Fu Lin for his educational and financial support. His creative thinking in science, strategic design in experiments help me in every way to accomplish this work. I greatly appreciate his patience and critical comments on revisions of every single of manuscript. I thank Stephen P. Grand, John C. Lassiter, Donald D. Blankenship, and Xiaoqin Li, for serving as my committee members and sharing with me the bright ideas. I want to thank former post-doctoral fellow, Zhu Mao, who helped me initiate the research of single-crystal elasticity study. I am extremely grateful to my collaborators, Shun-ichiro Karato at Yale University and Steve D. Jacobsen at Northwestern University for their constructive discussions for improving this work. I thank Vitali Prakapenka, and Sergey Tkachev, at Advanced Photon Source (APS), Argonne National Lab (ANL) for the synchrotron experimental assistance. Many thanks should go to former and current group members: Xiang Wu, Jin Liu, Chang Lu, Jennifer Beam, Nikki Seymour, Dawe Fan, Maoshuang Song, Juejie Wu, Megan Matheney, Ye Wu, Xinyue Tong, Jason Kim, Rusty Roberts, Xianghai Meng, Stephen Armstrong, Jiachao Liu and Suyu Fu for their help and friendship. I want to thank my parents for their unconditional supports over the years. Lastly, I express my special thanks to my husband, who is also a Ph.D, for his continued encouragement and inspiration to let me pursue a life that I dream for.

# Sound Velocity Profiles of Lower Mantle Minerals: Implications to Geophysics and Geochemistry of the Deep Earth

Jing Yang, Ph.D.

The University of Texas at Austin, 2017

Supervisor: Jung-Fu Lin

Abstract

In this dissertation, I used heated diamond-anvil-cell techniques to simulate the environment of the Earth interior. Spectroscopic measurements, including Brillouin Light Scattering, Impulsive Stimulated Light Scattering and X-ray diffraction were performed to obtain elastic parameters of candidate lower mantle minerals, ferropericlase, bridgmanite and post-perovskite in a diamond anvil cell. Obtained single-crystal elastic constants, density, bulk and shear moduli allow us to derive seismic velocities, anisotropy, and lateral heterogeneity ratio to be compared with seismic observations. The results in this dissertation shed light on the observed seismic heterogeneity, anisotropy, and discontinuity within the Earth's lower mantle.

Thermoelastic modelling based on high P-T elasticity data from ferropericlase suggested that thermal perturbation dominates the lateral heterogeneity in upper part of the lower-mantle, but is not sufficient to explain the high lateral heterogeneity ratio in the lower-part of lower mantle. Chemical perturbations and/or spin transition effects can be the potential cause of seismic heterogeneity towards the lower part of lower mantle. By investigating the spin transition effects on the single-crystal elasticity of ferropericlase, we

found drastically softened $C_{11}$ and $C_{12}$ within the spin transition, while $C_{44}$ is not affected. This leads to significant $V_P/V_S$ reduction in the mid-lower mantle.

Single-crystal elastic constants of two Al, Fe-bearing bridgmanite have been reliably resolved at high pressures. Our results suggested that coupled Fe and Al substitution can greatly reduce the $V_S$ and slightly affect $V_P$ and $V_\Phi$ of bridgmanite. In addition, the enhanced $V_S$ anisotropy of Fe and Al enriched bridgmanite may contribute to the seismic anisotropy in Earth's lower mantle. The presence of Fe, Al enriched bridgmanite could exhibit distinct seismic features in Earth's lower mantle.

The existence of post-perovskite in the D" region is still uncertain. Direct $V_P$ and $V_S$ measurements performed on Fe-bearing post-perovskite that compared with extrapolated velocities of bridgmanite showed a $V_S$ increase and $V_P$ decrease across the phase boundary, which are consistent with the seismic discontinuities especially observed beneath the Cocos Plate to the first order. The measured velocity profiles of post-perovskite provide strong mineral physics constraints on the velocity profiles for the existence of Fe-bearing post-perovskite in the D" layer.

# Table of Contents

# List of Tables

# List of Figures

# Chapter 1: Introduction

Earth's lower mantle is typically defined as the region ranging from a depth of 660 km down to the Earth's core-mantle-boundary, and is the most voluminous layer of the Earth's interior. Seismic studies offer the most direct way to probe the properties of Earth's lower mantle. Strong constraints on the chemical and physical states of the lower mantle can be placed if mineral physics predications on constitute lower mantle minerals are compared with seismic observations. Therefore, knowledge of the elastic properties of candidate lower mantle minerals with various chemical compositions is essential to understand lower mantle mineralogy, and potential seismic and chemical heterogeneity within the lower mantle, and can ultimately provide insights to deep mantle convection, as well as thermal and chemical evolution of the Earth.

## 1.1 Seismic Structures of Earth's Lower Mantle

Most of the 1-dimensional seismic studies, which describe velocity variations with depth, show a relatively homogeneous lower mantle (PREM, AK135) [*Dziewonski and Anderson*, 1981; *Kennett et al.*, 1995]. The compressional ($V_P$) and shear wave ($V_S$) velocities increase smoothly and monotonically with depth, without any observed discontinuity until ~300 km above the CMB, which is referred to as the D" layer. In this layer, a significant $V_S$ discontinuity has been found in various locations, e.g., beneath Cocos Plate, Southeast Asia, Central Pacific [*Chaloner et al.*, 2009; *Ding and Helmberger*, 1997; *Hutko et al.*, 2008; *Kito et al.*, 2007; *Russell et al.*, 2001]. With more detailed tomographic studies, it has been shown that this few hundred kilometers above the CMB is much more complex seismically than originally thought [*Garnero and McNamara*, 2008].

Regional seismic studies in the D" region not only reveal a discontinuity increase in $V_S$ ~1-3%, but also a seismic anisotropy, where horizontally polarized shear velocity

($V_{SH}$) travels with a different speed compared to the vertical polarized component ($V_{SV}$). The majority of the seismic observations show that $V_{SH} > V_{SV,}$ with a difference of 0.5-3% between the horizontal and vertical components. Seismic anisotropy is especially prominent in the locations with higher-than-average $V_S$, for example, the area around the circum-Pacific rim [*Lay et al.*, 1998; *Matzel et al.*, 1996]. In other studies, however, it has been also suggested that $V_{SV} > V_{SH}$ beneath the central Pacific [*Pulliam and Sen*, 1998].

Long-wavelength seismic studies with a typical resolution of 1000 km revealed two broad regions with lower-than-average $V_S$ and a slightly elevated density beneath the central Pacific and Africa, which are referred as large-low-shear-velocity provinces (LLSVPs) [*Ishii and Tromp*, 2004; *Trampert et al.*, 2004]. These two massive regions, which cover ~50% of the CMB topography and extend up to ~1200 km above the CMB, are surrounded by the cold and dense subducted rocks that are composed of ancient oceanic plate [*Garnero et al.*, 2016]. The origins of LLSVPs can be attributed to either thermal or chemical anomalies [*Davies et al.*, 2015]. However, it has been shown that the temperature alone cannot satisfactorily explain the seismic heterogeneity within the LLSVPs due to the observed anti-correlated $V_S$ and bulk sound velocity ($V_\Phi$). Strong lateral variations in $V_S$ were found at the margins of LLSVPs, which suggests that LLSVPs may be compositionally distinct [*Ritsema et al.*, 2011]. However, the origin, evolution, and stability of LLSVPs are still not well understood. With high resolution seismic studies, thin patches with strong $V_P$ and $V_S$ reductions were found within and near the margins of LLVSPs [*McNamara et al.*, 2010]. The small-scale heterogeneity with ~10% $V_P$ and ~30% $V_S$ reduction, referred to ultra-low-velocity-zones (ULVZs), are typically interpreted as Fe-enriched materials [*Mao et al.*, 2006] or partial melting [*Lay et al.*, 2004b].

The distinct seismic structures in the lower mantle reveal complex chemical and/or thermal structure compared to the background lower mantle, the origins of which remain

uncertain. Therefore, thermal properties and elastic parameters of candidate minerals at relevant lower-mantle pressure (P) and temperature (T) conditions are needed to reconcile the recent geophysical, geochemical, and geodynamic studies.

### 1.2 Elasticity Studies of Lower Mantle Minerals

Earth's lower mantle is believed to consist of ferropericlase (Fp) [(Mg,Fe)O], bridgmanite (Bgm) [(Mg,Fe)(Al,Si)$O_3$] and small amounts of calcium silicate perovskite (Ca-Pv) [$CaSiO_3$]. This is based on laboratory phase transformation studies, which show ringwoodite and majorite garnet dissociate into Bgm, Fp and Ca-Pv at 660 km P-T conditions. Bgm is eventually transformed to its polymorph post-perovskite (PPv) at 125 GPa and ~2000 K, which is relevant to the D" P-T conditions [*Murakami et al.*, 2004; *Ono and Oganov*, 2005]. However, the existence of PPv in the D" layer remains to be examined due to the inconsistency of P-T ranges of this phase transition among recent studies [*Grocholski et al.*, 2012; *Hirose et al.*, 2006]. Knowledge of the elasticity and density of lower-mantle minerals provide strong constraints on the composition of the lower mantle when compared with observed seismic data [*Irifune et al.*, 2010; *Murakami et al.*, 2012; *Wang et al.*, 2015]. Earth's lower mantle is considered to be pyrolitic with ~75 vol.% of Bgm, 20 vol.% of Fp and 5 vol.% of Ca-Pv based on combined laboratory data on phase transformations, sound velocity, chemical composition, and density in these materials, which show consistency with typical seismic models. These data suggest an isochemical lower mantle [*Irifune*, 1994; *Irifune et al.*, 2010]. A perovskitic lower mantle with ~ 93% Bgm was proposed based on high P-T $V_S$ data of polycrystalline Fp and Bgm samples, which indicated that the lower mantle may be rich in Si, suggesting a chemically distinct lower mantle with layered lower mantle convection [*Murakami et al.*, 2012]. A recent study on the single-crystal elasticity of Al and Fe-bearing Bgm showed the pyrolite model only

applies to the upper lower mantle to a depth of ~1200 km with a high $Fe^{3+}/Fe^{2+}$ ratio, implying the presence of metallic Fe in an isochemical mantle. In the context of this study, the chemical composition in the lower part of lower mantle remains unclear [*Kurnosov et al.*, 2017]. In sum, elasticity studies are thus far not in agreement about the chemical composition of the Earth's lower mantle. Therefore, accurate experimentally determined elasticity of candidate lower mantle minerals should be extensively investigated.

Fp [(Mg,Fe)O], the second most abundant mineral in the Earth's lower mantle, exhibits several interesting phenomenon under lower mantle P-T conditions and may greatly influence our understanding of Earth's interior. For example, the Fe electronic spin transition in Fp that occurs ~ 40-50 GPa from high spin state (spin number = 2) to low spin state (spin number = 0), is reported to have a significant effect on the density, bulk moduli, thermal expansion, electronic conductivity, and viscosity under lower-mantle conditions [*Lin et al.*, 2005; *Lin et al.*, 2007c; *Mao et al.*, 2011b; *Wentzcovitch et al.*, 2009]. Of foremost importance is the Fe spin transition effect on the elasticity of Fp, as it directly affects our interpretation of seismic observations for the Earth's lower mantle.

Here we focus on single-crystal elasticity study of Fp, as the full set of elastic constants of a crystal provide thorough information of its physical properties. With cubic crystal structure, Fp has three elastic constants, $C_{11}$, $C_{12}$ and $C_{44}$. A single-crystal elasticity study of Fp by using Impulsive Stimulated Light Scattering (ISS) up to 60 GPa at 300 K shows reductions of all three elastic constants across the Fe-spin transition pressure region, resulting in remarkable softening of both $V_P$ and $V_S$ [*Crowhurst et al.*, 2008]. In this study, however, the elastic constants of low-spin state ferropericlase were not provided; these are essential pieces of information because low-spin ferropericlase may exhibit distinct behaviors that affect seismic interpretation of the lower part of the lower mantle. Another study using inelastic X-ray scattering (IXS) up 70 GPa at 300 K observed only $C_{44}$

reduction across the spin transition pressure range from 40-60 GPa, suggesting at lower mantle conditions both $V_P$ and $V_S$ are unaffected by the spin transition [*Antonangeli et al.*, 2011]. This study implies that the spin transition in the lower mantle may be seismically transparent. A Brillouin light scattering study, which only focused on the shear moduli $C_{44}$ and ($C_{11}$-$C_{12}$), also showed no substantial reduction of $V_S$. No direct information about the behavior of $V_P$ was provided due to the experimental limitations [*Marquardt et al.*, 2009b]. It is notable that the experimental studies on single-crystal elasticity are limited to 300 K, even for the high spin state elasticity data. Therefore, experimental results including the net effect of temperature and pressure on the elasticity are necessary.

Theoretical calculations provide an alternative way to study the elasticity of ferropericlase at high P-T. A recent theoretical work with an extended P-T range up to 150 GPa and 4000 K showed reduction of $C_{11}$ and $C_{12}$ but no reduction of $C_{44}$ across the spin transition at 300 K. $C_{11}$ and $C_{12}$ reductions exhibited equal broadness and decreased magnitude with elevated temperature [*Wu et al.*, 2013]. Their results introduced a softening of $V_P$ but no effect in $V_S$ across the spin transition along an adiabatic geotherm, which contradicts some of the experimental studies. Their calculations also suggested that the seismically observed variations in $V_S$ and $V_\Phi$ are anti-correlated in the lower mantle, which has been previously explained as chemical heterogeneity, can also be produced by the isochemical composition containing Fp [*Wu and Wentzcovitch*, 2014], which has never been investigated experimentally before. Due to the contradictory results in experiments across the spin transition and new questions arising from theoretical calculation, reliable measurement on the elasticity of Fp in high spin, mix spin, as well as low spin states are essential.

Bridgmanite is the most abundant mineral in the Earth's lower mantle, which may incorporate ~5-10 mol% of Fe and Al in its lattice based on element partitioning studies in

the Earth's lower mantle [*Irifune et al.*, 2010]. Bridgmanite is in orthorhombic crystal structure with 9 elastic constants ($C_{11}$, $C_{22}$, $C_{33}$, $C_{44}$, $C_{55}$, $C_{66}$, $C_{12}$, $C_{23}$ and $C_{13}$), which is a more complex system compared to Fp that only has 3 elastic constants. This means that reliably constraining the full set of elastic constants is much more difficult for Bgm, requiring sufficient directionally dependent $V_P$ and $V_S$ measurements within multiple single-crystal platelets with different orientations. High quality single crystals without twinning and deformation are also required. Theoretical calculations can assuage such experimental difficulties, providing invaluable data to model the lower mantle seismic properties [*Karki et al.*, 1997; *Li et al.*, 2005; *Wentzcovitch et al.*, 2004; *Wentzcovitch et al.*, 1998]. Experimentally, single-crystal elasticity on bridgmanite has been mostly measured at ambient conditions for Fe, Al-free bridgmanite [*Sinogeikin et al.*, 2004; *Yeganeh-Haeri*, 1994]. A recent study on single crystal elasticity measuring both Fe, Al-free and Fe, Al-bearing bridgmanite at ambient conditions using inelastic x-ray scattering (IXS) showed that Fe and Al have appreciable effects on the elasticity [*Fukui et al.*, 2016]. They claimed that the cation-substitution of Fe and Al in bridgmanite results in anti-correlated $V_S$ and $V_\Phi$, which explains the seismic observations in LLSVPs. However, applying the results from ambient conditions to interpret the phenomenon at high P-T conditions sometimes can be problematic. High P-T elasticity data on realistic chemical compositions is essential. Another recent high pressure elasticity study on a Fe, Al-bearing Bgm with a significant amount of $Fe^{3+}$ ($Fe^{3+}/Fe^{2+}$ = 0.66) to 40 GPa showed that their modeled $V_P$ and $V_S$ containing high $Fe^{3+}$ content in bridgmanite were consistent with the PREM model only to ~1200 km, but their results increasingly diverged from the seismic model for the lower part of lower mantle [*Kurnosov et al.*, 2017]. These results imply that upper part of lower mantle should contain high amounts of $Fe^{3+}$ to reconcile with seismic observations, and that the lower part of lower mantle may contain less $Fe^{3+}$, indicating a

layered chemical structure for lower mantle. However, the amount of $Fe^{3+}$ in the Earth's lower mantle is still uncertain, and could be significantly affected by the coupled substitution of Al and Fe in the bridgmanite crystal lattice. Further examination of single-crystal bridgmanite with different Al and $Fe^{2+}$, $Fe^{3+}$ contents at high pressure is needed.

Bridgmanite transforms into post-perovskite (PPv) at D" P-T conditions, which was first observed experimentally and later substantiated theoretically [*Murakami et al.*, 2004; *Ono and Oganov*, 2005; *Tsuchiya et al.*, 2004a]. This solid-solid phase transformation has been used to explain seismic discontinuity as well as shear wave anisotropy within the D" layer [*Wookey et al.*, 2005]. However, the existence of PPv in the D" region is still under debate. The broadness of this phase transition has been studied in different realistic mineralogical settings, for example, in pyrolite materials and mid-ocean-ridge-basalt (MORB) [*Grocholski et al.*, 2012]. The results show that the phase transition pressure range is about 10-30 GPa in pyrolite, and narrower (~3-15 GPa) in MORB. This raises the concern that the transition may be too broad to be detected as a sudden jump in $V_S$ observed in D". Therefore, the velocity and density contrast due to this Bgm to PPv phase transition should be tested experimentally to evaluate the possible change that produces any detectable seismic features.

Within Earth's lower mantle, the key issues to be understood by mineral physics efforts are 1) the compositional model of Earth's lower mantle; 2) origins of seismic heterogeneities within the lowermost region of the lower mantle; and 3) existence of post-perovskite in D" layer. To address these issues, we have to examine 1) the combined pressure, temperature and compositional effects on elasticity of lower mantle minerals; 2) how spin transition affects the physical and chemical properties of host minerals; and 3) the seismic features of post-perovskite in the D″ region. In this dissertation, I have attempted to solve several of the questions raised above using the techniques introduced in

Chapter 2, including diamond anvil cell (DAC), Brillouin Light Scattering (BLS), Impulsive Stimulated Light Scattering (ISS) as well as X-ray diffraction. Chapter 3 describes my BLS results on the single-crystal elasticity of ferropericlase $(Mg_{0.94}Fe_{0.06})O$ at high pressure and temperature. Chapter 4 describes my results using combined BLS and ISS to examine the velocity abnormalities of single-crystal ferropericlase $(Mg_{0.92}Fe_{0.08})O$ across the Fe electronic spin transition up to mega-bar pressure. Chapter 5 describes single-crystal elasticity data on two Fe, Al-bearing bridgmanite samples at high pressures to study the pressure and compositional effects on the elastic properties of bridgmanite. Finally, Chapter 6 presents my results on the $V_P$ and $V_S$ measurements of Fe-bearing post-perovskite at D" pressures to investigate the velocity contrast of the bridgmanite and post-perovskite phase transition.

# Chapter 2: Experimental Techniques

In this chapter, I will introduce the experimental techniques used in this dissertation. Diamond anvil cells (DAC) were employed to generate high pressure on the studied samples and served as a probing window for *in situ* characterizations of material properties. Brillouin Light Scattering (BLS) was used to measure the elastic properties of studied samples, including acoustic wave velocities, bulk modulus, shear modulus, and elastic constants. Impulsive Stimulated Light Scattering (ISS) is a pump-probe method for measurements of acoustic wave velocities of materials. In this dissertation, it is combined with BLS to simultaneously measure compressional and shear wave velocities of the samples at very high pressure. Synchrotron X-ray diffraction was also used to determine the crystal structure, unit cell parameters as well as equation of state of the samples.

## 2.1 Diamond Anvil Cell (DAC)

In high pressure studies, shock wave devices, large-volume presses (LVP) and diamond anvil cells (DAC) are commonly used high pressure apparatus. Shock wave experiments are dynamic processes, which can compress samples to multi-megabar pressure for a short time scale (nano - femto seconds). In LVP and DAC experiments, static compression is involved. LVPs can generate modest pressure (up to ~100 GPa), and the sample size can be large, typically in millimeters. DACs are capable to generate pressure beyond ~ 500 GPa [*Dias and Silvera*, 2017; *Dubrovinsky et al.*, 2012], but the sample size is relatively small, normally ranging from 20-100 microns. We will focus on DACs, which consist of three basic components: opposing diamond anvils as pressure generator and probing window, gaskets as sample chambers, and pressure medium to ensure a hydrostatic environment (Figure 2.1).

(A) *Diamond Anvils*

Single-crystal diamond is generally used as anvil material. The diamond is an ideal material in high pressure research due to its unique properties including: optically transparent, the highest Mohs hardness and fracture toughness, highest thermal conductivity, ultra-high melting temperature, etc. Due to its superior features, DAC can be used for *in situ* experiments in a wide pressure and temperature regime.

Standard cut diamond anvils with thick girdles, large tables and flat culets (Figure 2.1) is designed to withstand the highest pressure. It relies on a simple principle that the pressure ($P$) is equal to the force ($F$) divided by area ($A$): $P = F/A$. The force applied to the table surface area is directly transmitted to the small opposing culets, typically in micron meter size, where the pressure can be amplified if the culet size is small enough. In general, diamond anvils with a flat culet size of 300 and 200 μm can safely reach to pressures of 65 and 100 GPa, respectively. For higher pressure experiments, smaller beveled culets should be used.

(B) *Gaskets*

The gasket is an essential component in the DAC experiments to support the pressure between two opposing diamond culets and serves as a sample chamber (Figure 2.1). Typically, a gasket with a 250 μm thickness is pre-indented to 35- 50 μm thick. A hole is drilled at the center in the pre-indented area by electrical discharging machining or laser ablation, which later serves as sample chamber. Various materials are used as gaskets to match the experimental goals. In this dissertation, high-strength rhenium is commonly used for high pressure experiments; specially treated rhenium-tungsten alloy is used for externally-heated experiments to withstand high temperature.

(C) *Pressure Medium*

The purpose of pressure medium in high pressure experiments is to minimize the non-hydrostatic conditions that cause pressure inhomogeneity and pressure gradient onto the samples. Low-strength and chemically inert materials, for example, Argon, Neon and Helium are selected as pressure mediums surrounding the sample in the sample chamber. Inert gases solidify at certain pressures, which produce quasi-hydrostatic conditions up to ~9 GPa in Argon [*Mao et al.*, 1986], ~15 GPa in Neon and over ~100 GPa in Helium [*Klotz et al.*, 2009]. In this dissertation, the most commonly used are Neon and Helium, which were loaded using a gas loading system in the Mineral Physics Laboratory, The University of Texas at Austin. The solids NaCl and KCl were also used as pressure mediums as well as temperature insulators in laser-heating experiments.

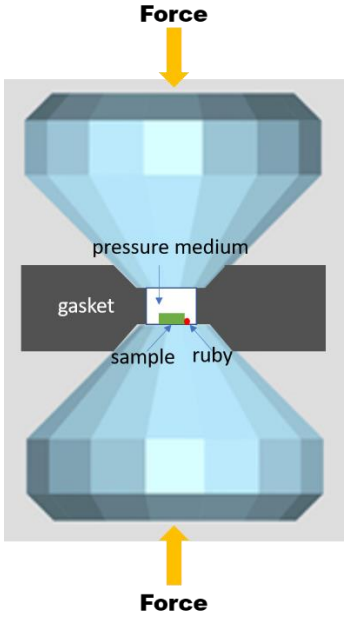


Figure 2.1: Diamond anvil cell (DAC) components. The diamonds anvils were purchased from Almax easyLab Inc.

(D) *Exterior design of DAC*

Short piston-cylinder symmetrical cells have a wide optical access with 96-degree opening angle. They are especially useful for spectroscopic measurements which have a scattering angle. Because of this, they are normally used for Brillouin and Impulsive experiments in this dissertation (Figure 2.2a). A BX90 externally-heated diamond anvil cell is used to perform high temperature and pressure experiments (Figure 2.2b). A small resistive heater placed around the diamond anvils is used to homogeneously heat the sample up to 1000 K [*Kantor et al.*, 2012].


(a) (b)

Figure 2.2: Exterior designs of DAC. (a) Short piston-cylinder symmetrical cells [*Mao*, 2009]; (b) BX90 externally-heated DAC (after Kantor et al., 2012).

## 2.2 BRILLOUIN LIGHT SCATTERING (BLS)

Brillouin Light Scattering (BLS) was first predicted in 1922 by Léon Nicolas Brillouin, a French physicist, to be the inelastic scattering of light by thermally generated acoustic vibrations [*Brillouin*, 1922]. In quantum mechanical point of view, BLS can be treated as photon-phonon interaction. In Brillouin experiments, an incident beam with certain wave vector and frequency propagates through a medium. Photons interact with the medium to cause absorption and creation of phonons. This interaction leads to the

frequency shift of the scattered radiation. The frequency shift could be resolved by the high resolution Fabry-Perot interferometer as an analyzer [*Sandercock*, 1971] and shown as Brillouin spectrum. The acoustic wave velocity can be calculated based on the laser geometry and Brillouin frequency shift as follows:

$$v = \frac{\Delta \upsilon_B \lambda_0}{2\sin(\theta/2)}$$

where $v$ is the measured acoustic velocity, $\Delta \upsilon_B$ is the Brillouin frequency shift, $\lambda_0$ is the laser wavelength of 532 nm, and $\theta$ is the external scattering angle. BLS is the most commonly used technique for measurements of single-crystal elastic properties of geophysical interest, which can be performed in-house or on-line (combined with synchrotron X-ray diffraction).

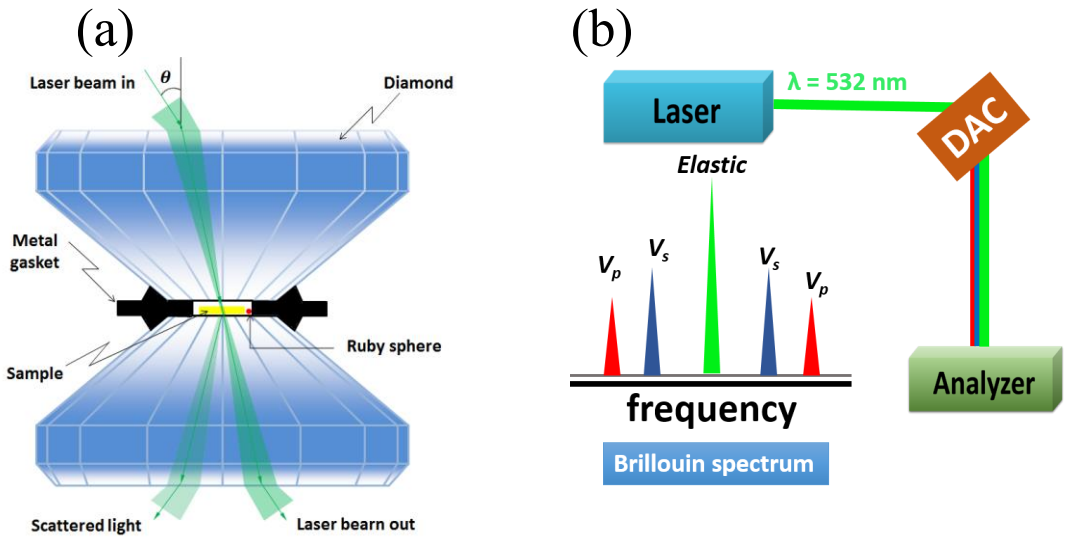


Figure 2.3: Brillouin Light Scattering experiments. (a) Geometry of BLS. (b) BLS setup and BLS spectrum (after Bass 2007).

BLS is widely used to obtain single-crystal elasticities. When waves propagate through an anisotropic media, the acoustic wave velocities vary with direction. The elastic constants of a material are related to the acoustic wave velocity and can be obtained by fitting with the Christoffel's equation [*Every*, 1980]: $\left|C_{ijkl}n_in_j - \rho v^2\delta_{ik}\right| = 0$, where $v$ is the measured velocity with different crystallographic orientations, $\rho$ is the density, $n_i$ is wave direction cosine and $\delta_{ik}$ is the Kronecker delta. The elastic constants, $C_{ijkl}$, are written as full suffix notation in Christoffel's equation, which can be contracted to $C_{ij}$ in Voigt form based on symmetry.

Although, BLS has proven to be a powerful method to measure both $V_P$ and $V_S$ at high pressures, it is limited to certain pressures below ~ 40 GPa [*Kurnosov et al.*, 2017]. This limitation occurs because the BLS method simultaneously measures the velocities of the sample and the diamond anvils. At such high pressure, the $V_P$ of the sample approaches the $V_S$ of diamond (~12 km/s). Thus, the signal from the sample can be masked by the diamond $V_S$ peak. Unfortunately, $V_P$ is necessary to constrain the full set of elastic constants of a crystal. One of the reasons we employ an Impulsive Stimulated Light Scattering (ISS) system is to measure $V_P$ of a crystal at higher pressure.

### 2.3 IMPULSIVE STIMULATED LIGHT SCATTING (ISS)

The ISS is a time-resolved optical spectroscopy, which has proven to be a powerful method to study the elastic properties of crystals and fluids. The technique and the system setup are explicitly described in Tong's master's thesis [*Tong*, 2014]. I will briefly introduce the experimental implementation here.

In the Impulsive system, we use two IR lasers with a wavelength of 1064 nm as the excitation and pump lasers, and a green laser with 532nm wavelength as the probe beam (Figure 2.4). The IR pump lasers and green laser are focused at the sample position with a

~20 nm beam spot with a crossing angle of 20.3°. Crossing two excitation pulses will form the interference grating patterns, which defines the wavelength of the acoustic wave propagating across the sample. The probe beam is incident upon the center of the grating Bragg angle. The time delay between the excitation and probe beam is controlled mechanically by moving the retroreflector on an Aerotech linear stage. For each given delay time, diffracted signal intensity is recorded by a photodiode detector. The time-domain raw ISS spectrum were Fourier-transformed from the time domain to the frequency domain based on Burg method using Matlab program and OriginPro software and then converted to velocity based on the setup geometry.

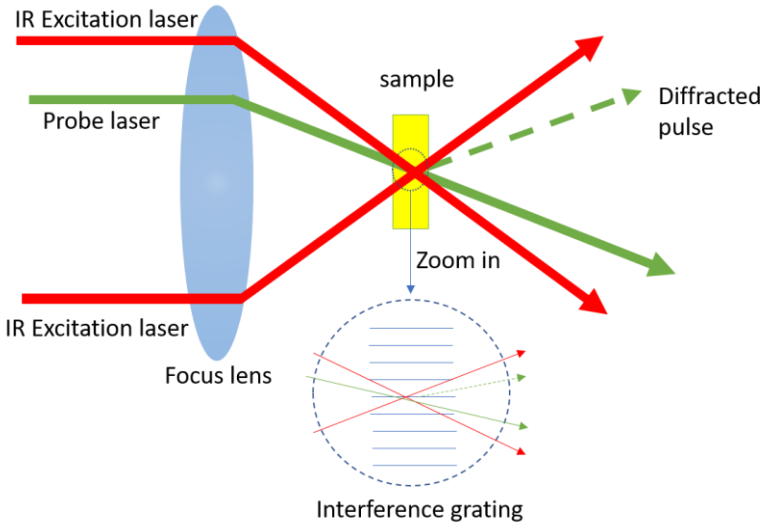


Figure 2.4: Impulsive Stimulated Light Scattering laser beam geometry and experimental setup (after Tong, 2014).

## 2.4 SYNCHROTRON X-RAY DIFFRACTION (XRD)

High energy and small beam (less than ~5 microns) synchrotron X-ray diffraction is extensively used for high pressure research on tiny samples, which provides structural information of various forms of samples (polycrystalline, single crystal, amorphous etc.). Single-crystal XRD with wide scan is also used in this dissertation to determine the single-crystal orientation and to check the crystallinity of a crystal.

In XRD experiments, the *d*-spacing between diffraction planes within a crystal lattice relates to the wavelength ($\lambda$) and angle ($\theta$) of the incident beam, which is described by Bragg's law:

$$2dsin\theta = n\lambda$$

where *n* is any integer. The lattice parameters of a crystal can be calculated by a collection of *d*-spacings between adjacent lattice planes (*hkl*). For example, the unit cell parameter ($a$) for cubic crystal structure is given by:

$$a^2 = \frac{d^2}{h^2+k^2+l^2}.$$

With obtained unit cell parameters of the sample, the equation of state of sample at high P-T can be subsequently obtained. The density of the sample can be calculated if the chemical composition (characterized by Electron Microbeam Probe) of the sample is known.

# Chapter 3: High P-T Single-crystal Elasticity of Ferropericlase and Seismic Heterogeneity in the Earth's Lower Mantle[1]

Deciphering the origin of seismic heterogeneity has been one of the major challenges in understanding the geochemistry and geodynamics of the deep mantle. Fully anisotropic elastic properties of constituent minerals at relevant pressure-temperature conditions of the lower mantle can be used to calculate seismic heterogeneity parameters in order to better understand chemically- and thermally-induced seismic heterogeneities. In this study, the single-crystal elastic properties of ferropericlase $(Mg_{0.94}Fe_{0.06})O$ were measured using Brillouin spectroscopy and X-ray diffraction at conditions up to 50 GPa and 900 K. The velocity-density results were modeled using third-order finite-strain theory and thermoelastic equations along a representative geotherm to investigate high pressure-temperature and compositional effects on the seismic heterogeneity parameters. Our results demonstrate that from 660 to 2000 km, compressional wave anisotropy of ferropericlase increased from 4% to 9.7% while shear wave anisotropy increased from 9% to as high as 22.5%. The thermally-induced lateral heterogeneity ratio ($R_{S/P} = \partial \ln V_S / \partial \ln V_P$) of ferropericlase was calculated to be 1.48 at ambient pressure but decreased to 1.43 at 40 GPa along a representative geotherm. The $R_{S/P}$ of a simplified pyrolite model consisting of 80% bridgmanite and 20% ferropericlase was approximately 1.5, consistent with seismic models at depths from 670 to 1500 km, but showed an increased mismatch at lower mantle depths below ~1500 km. This discrepancy below mid-lower mantle could be due to either a contribution from chemically-induced heterogeneity or the effects of the Fe spin transition in the deeper parts of the Earth's lower mantle.

[1]This chapter is based on the article: Yang, J., J. F. Lin, S. D. Jacobsen, N. M. Seymour, S. N. Tkachev, and V. B. Prakapenka (2016), Elasticity of ferropericlase and seismic heterogeneity in the Earth's lower mantle, J. Geophys. Res. Solid Earth, 121(12), 8488-8500.

## 3.1 INTRODUCTION

Seismic heterogeneities within the Earth's lower mantle are typically attributed to thermal and/or chemical variations of the constituent materials [*Karato and Karki*, 2001]. Some authors have suggested that heterogeneity of the lower mantle is dominantly due to thermal effects [*Forte*, 2000; *Forte et al.*, 1994; *Hager et al.*, 1984] while chemical heterogeneity has been invoked by other studies to explain large low-shear-velocity provinces (LLSVPs) in the lowermost mantle beneath the Pacific and African plates [*Garnero and McNamara*, 2008; *van der Hilst and Kárason*, 1999]. A more recent study has proposed a combined thermo-chemical mechanism for the development of the seismic structure of LLSVPs based on their long-wavelength structure, lateral shear-velocity anisotropy, sharp velocity gradients along their margins, and anti-correlated bulk and shear-velocities [*Davies et al.*, 2015]. Distinguishing between the thermal and chemical contribution to seismic heterogeneities of the lower mantle from a material properties perspective is critical as each mechanism has drastically different implications for our understanding of the geodynamics, geochemistry, and thermal evolution of the planet's interior. Our present understanding of the origin of the lateral heterogeneity in the lower-mantle minerals remains mostly theoretical [*Tsuchiya*, 2011; *Wu and Wentzcovitch*, 2014]. However, comparisons of lateral variations in seismic shear wave ($V_S$) and compressional wave ($V_P$) velocities, given as $R_{S/P} = \partial \ln V_S / \partial \ln V_P$, in conjunction with mineral physics elasticity experiments on lower-mantle minerals at relevant pressure-temperature (P-T) conditions can provide new constrains on the lower-mantle seismic structures and dynamics.

Based on the pyrolite model, Earth's lower mantle, the most voluminous layer of the planet, consists of approximately 75% bridgmanite $(Mg,Fe)SiO_3$, 20% ferropericlase $(Mg,Fe)O$, 5% Ca-silicate perovskite ($CaSiO_3$) [*Ringwood*, 1975]. Accurate determinations

of the elastic properties of deep Earth materials under the relevant P-T conditions are essential for understanding seismic models of the deep mantle. It has been suggested that variations in mineralogy, Fe or Al content of bridgmanite, as well as Fe spin states are plausible candidates for lateral heterogeneity in Earth's lower mantle [*Jackson et al.*, 2005; *McCammon et al.*, 2008]. Changes in the elasticity and texture of ferropericlase including the effects of the spin transition are also proposed as potential sources of mid-lower mantle seismic heterogeneities [*Karato and Karki*, 2001; *Wu and Wentzcovitch*, 2014]. The elasticity of ferropericlase with varying Fe content has been experimentally and theoretically studied at lower mantle pressures across the spin transition, showing that $V_P$ is significantly reduced while *Vs* remains unaffected over the transition [*Jackson et al.*, 2006; *Marquardt et al.*, 2009a; *Wu et al.*, 2013; *Wu and Wentzcovitch*, 2014; *Yang et al.*, 2015]. Ferropericlase is a rheologically weaker phase compared to bridgmanite and can develop a strong lattice preferred orientation, potentially producing shear-wave anisotropy $V_{SH} > V_{SV}$ (where $V_{SH}$ and $V_{SV}$ are the velocities of the horizontally and vertically polarized seismic shear waves, respectively) that observed seismically in the lower mantle [*Yamazaki and Karato*, 2002]. However, the contribution of ferropericlase to the thermal and chemical heterogeneity has remained theoretical. Fully resolving its density, elastic constants, as well as bulk and shear moduli under high P-T conditions is critical to rigorously test theoretical calculations against experimental data and explicitly elucidate the thermal and chemical variations in the lower mantle.

Here we have measured the acoustic wave velocities and density of synthetic single-crystal ferropericlase [$(Mg_{0.96}F_{0.06})O$] at high P-T conditions up to 50 GPa and 900 K using Brillouin Light Scattering (BLS) combined with X-ray diffraction (XRD) in an externally-heated Diamond Anvil Cell (EHDAC). Using these data, we have calculated elastic and seismic properties of ferropericlase along a representative lower mantle

geotherm and discuss the potential contribution of ferropericlase on seismic heterogeneities of the lower mantle.

### 3.2 EXPERIMENTAL METHODS

Single-crystal ferropericlase with $X_{Fe}$ = Fe/(Mg+Fe) = 0.06 ($(Mg_{0.94}Fe_{0.06})O$, hereafter denoted as fp6) was synthesized through the inter-diffusion of Fe and Mg between single-crystal periclase (MgO) and pre-reacted (Mg,Fe)O powders [*Jacobsen et al.*, 2002]. The ferric-iron content $Fe^{3+}/Fe$ = 0.02(1), density $\rho_0$ = 3723 kg/m3, and other details of synthesis, structure, and elastic properties of the sample at ambient conditions were reported by Jacobsen et al. [2002]. For high P-T Brillouin and XRD measurements, thin plates of the single-crystal ferropericlase were polished on both sides perpendicular to [100] to ~12 μm in thickness and then cleaved into several ~70×70 μm square pieces. Single-crystal XRD patterns with an incident X-ray wavelength of 0.3344 Å were used to determine sample orientation and density at beamline 13-BMD in GeoSoilEnviroCARS (GSECARS) of the Advanced Photon Source, Argonne National Lab (APS, ANL). Re-W alloy, which is more stable at high temperatures than a typical Re gasket, was used as the gasket material for high P-T experiments [*Kantor et al.*, 2012]. A 250 μm thick gasket was pre-indented to ~30-40 μm by a pair of diamonds with a 300 μm culet size in an EHDAC. A hole of 170 μm was subsequently drilled and used as sample chamber. The ferropericlase crystal was loaded into the EHDAC sample chamber together with Au powder, which served as the pressure calibrant at high P-T [*Fei et al.*, 2007a], and a ~5 μm ruby sphere, used as the pressure indicator for loading Ne gas pressure medium. The temperature of the sample in the EHDAC was measured using an R-type thermocouple attached to one of the diamond anvils approximately 500 μm away from the diamond culet. The EHDAC was equipped with an alumina ceramic heater coiled with two pieces of Pt wire of 200 μm

diameter and 48 cm in length [*Kantor et al.*, 2012]. Four experimental runs at GSECARS were conducted over a two-year period totaling ~60 8-hour shifts to collect the data presented here.

High P-T Brillouin measurements were conducted at stepwise pressures up to 50 GPa at four constant temperatures of 300 K, 550 K, 750 K and 900 K at 13 BMD in GSECARS of the APS, ANL. To avoid potential oxidation of the diamond anvils and Pt wires at high temperature, Ar gas with 2% $H_2$ gas continuously flowed into the EHDAC during heating. A solid state Verdi V2 laser with a wavelength of 532 nm and a power of 0.4 W was used for Brillouin measurements. Brillouin spectra were collected in asymmetric forward scattering geometry with an external scattering angle of 50° using a six-pass Tandem Fabry-Perot interferometer. The acoustic velocities of the Brillouin spectra were derived from the measured Brillouin frequency shift as follows:

$$V_{P,S} = \frac{\lambda_0 \Delta v_B}{2\sin(\theta/2)}, \quad (1)$$

where $V_{P,S}$ is the measured acoustic velocity, $\lambda_0$ is the laser wavelength of 532 nm, $\Delta v_B$ is the Brillouin frequency shift, and $\theta$ is the external scattering angle of 50°. The Brillouin spectra were collected along principle axes [100] and [110] of single-crystal ferropericlase platelet, which were confirmed by in situ XRD patterns of the crystal before the measurements. XRD patterns of the ferropericlase at each given P-T were also used to determine the density $(\rho)$ of the sample. The elastic constants ($C_{11}$, $C_{12}$, and $C_{44}$) of ferropericlase were determined using the following equations via least-squares regression:

$$V_P\,[100] = (C_{11}/\rho)^{1/2}, \quad (2)$$

$$V_S\,[100] < 110 >= (C_{44}/\rho)^{1/2}, \quad (3)$$

$$V_P\,[110] = [(C_{11} + C_{12} + 2C_{44})/2\rho]^{1/2}, \quad (4)$$

$$V_S\,[110] < 110 >= [(C_{11} - C_{12})/2\rho]^{1/2}, \quad (5)$$

where [uvw] represents the crystallographic direction of acoustic wave propagation, and <uvw> indicates the polarization direction. Pressure was determined from the measured lattice parameter of Au and calibrated using the thermal equation of state [*Fei et al.*, 2007a]. Pressure was measured before and after each Brillouin measurement, and the average pressure was used in the equation of state fitting. Errors are given by their standard deviation (1σ).

### 3.3 Results and Thermoelastic Modeling

High P-T XRD patterns of the single-crystal ferropericlase ($Mg_{0.94}Fe_{0.06}$)O were collected up to 50 GPa at temperatures of 300 K, 550 K, 750 K, and 900 K (Figure 3.1). The lattice parameters of ferropericlase were calculated based on four sets of diffraction peaks corresponding to {200}, {220}, {400} and {420} equivalent reflections. Analysis of the XRD patterns of the sample also confirmed the crystal was oriented in the (100) crystallographic plane within approximately $\pm 1°$ angular uncertainty at high P-T. The P-V curves at each temperature were fitted using the third-order Birch-Murnaghan equation of state (EoS) [*Birch*, 1947]. The calculated density as a function of pressure at 300 K was consistent with values reported by Jackson et al. [2006] (Figure 3.1 inset). The thermal expansion coefficient $\alpha(T)$ was calculated using:

$$V(T) = V_0 \exp[\int_{T_0}^{T} \alpha(T) dT] \quad (6)$$

where $V_0$ is the volume at 300 K, and $\alpha(T)$ is a constant at ambient pressure, with a value of 3.0 (1) × 10-5 $K^{-1}$, determined by fitting the experimental data at ambient pressure. The pressure derivative of the thermal expansion coefficient ($\frac{\partial \alpha(T)}{\partial P}$) is approximately $-1.0 \times 10^{-7} K^{-1} GPa^{-1}$.

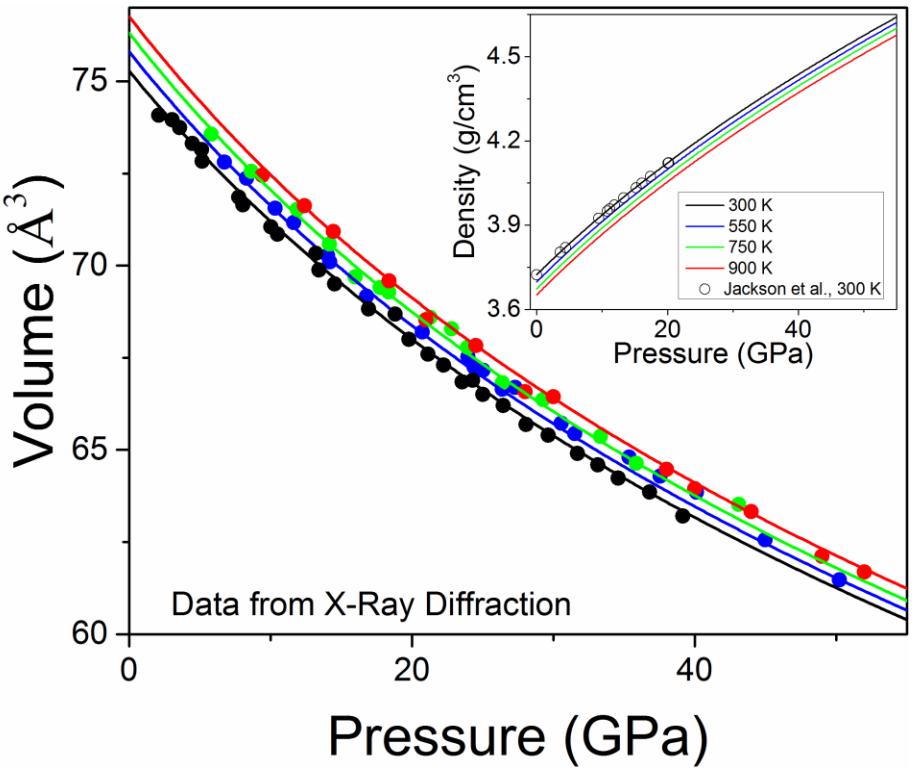


Figure 3.1: Pressure-volume-temperature relations of single-crystal ferropericlase $(Mg_{0.94}Fe_{0.06})O$ from X-ray diffraction. Solid symbols: experimental measurements at 300 K (black), 550 K (blue), 750 K (green) and 900 K (red). Lines: fits to experimental data using the third-order Birch-Murnaghan equation of state. The inset shows the density of the ferropericlase as a function of pressure. Open circles: Jackson et al. [2006].

High P-T Brillouin spectra of ferropericlase along [100] and [110] crystallographic directions are shown in Figure 3.2. Most of the Brillouin spectra showed strong $V_P$ and $V_S$ peaks with high signal-to-noise ratios at high P-T. The $V_P$ mode of ferropericlase overlapped with the $V_S$ of diamond in the anvils above ~30 GPa, preventing measurement of $V_P$ at these conditions. $V_P$ and $V_S$ modes as a function of pressure at each temperature along the [100] and [110] directions are shown in Figure 3.3. These velocities increase with increasing pressure except for $V_S$[100]<110>, which remains almost constant up to ~10

GPa before decreasing with increasing pressure. The velocities as a function of pressure at a constant temperature of 300 K are consistent with those reported for fp6 by Jackson et al. [2006]. Together with the density information at high P-T from XRD measurements, the measured $V_P$ and $V_S$ velocities of the single-crystal ferropericlase permit direct derivation of the full elastic constants at high P-T via equations (2)-(5) (Figure 3.4) [*Every*, 1980].

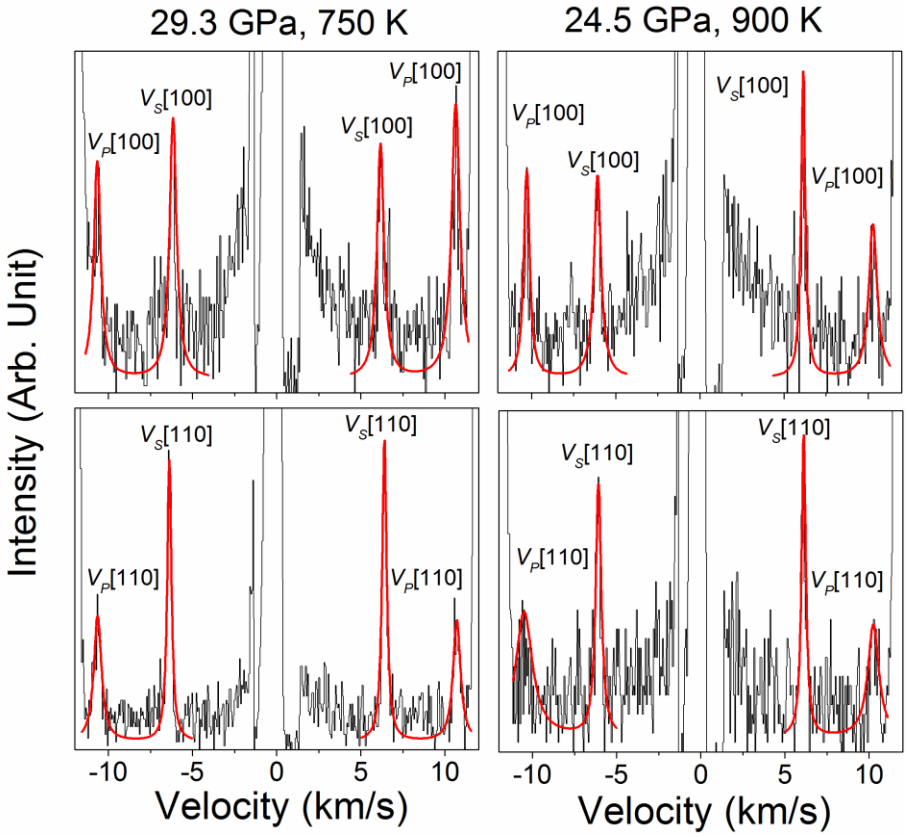


Figure 3.2: Representative Brillouin spectra of single-crystal ferropericlase $(Mg_{0.94}Fe_{0.06})O$ at high pressure and temperature. Black line: collected raw data; red line: Lorentz peak fit. Upper panels: velocity measured along [100] crystallographic direction; lower panels: velocity measured along [110] crystallographic direction.

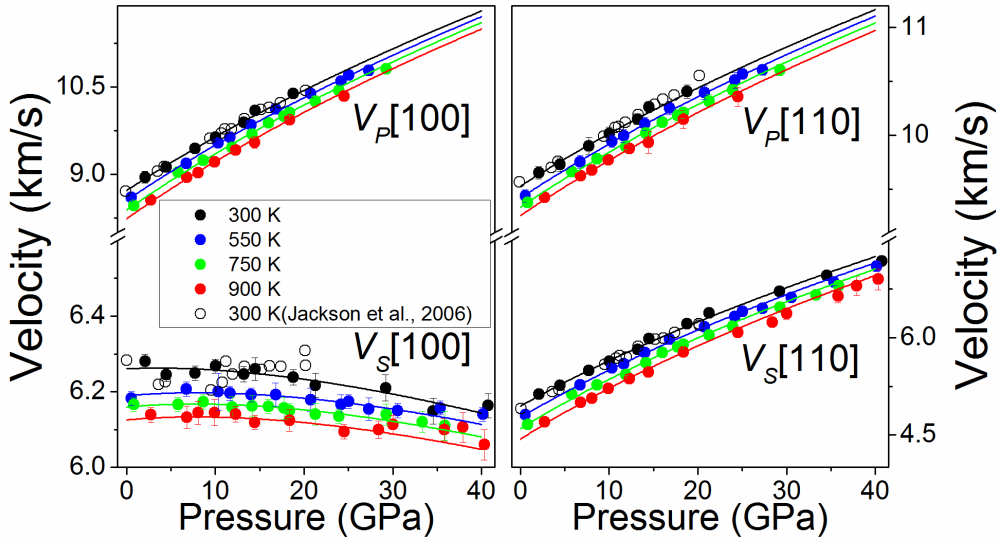


Figure 3.3: Acoustic velocities of the single-crystal ferropericlase $(Mg_{0.94}Fe_{0.06})O$ along [100] and [110] crystallographic directions as a function of pressure and temperature. Lines are calculated from modelled results of the elastic constants using finite-strain theory (see Figure. 3.4 for further details). Solid circles: this study; open circles: $(Mg_{0.94}Fe_{0.06})O$ crystal along same crystallographic directions reported by Jackson et al. [2006].

Elastic constants of the single-crystal ferropericlase $(Mg_{0.94}Fe_{0.06})O$ at ambient pressure as a function of experimental temperatures are shown in Table 3.1 and compared with literature results in Table 3.2. The pressure and temperature derivatives of the reference elastic moduli, as shown in Table 3.3, were obtained by fitting the moduli either at constant T, using the third-order Eulerian finite-strain equation (Figure 3.4) [*Birch*, 1978], or at constant P using linear equation:

$$C_{ij}^0(T) = C_{ij}^0(300\ K) + (T - 300)(\partial C_{ij}/\partial T)_P \quad (7)$$

$$C_{ij}(f) = (1+2f)^{7/2}\left[C_{ij}^0 + b_1 f + (1/2)b_2 f^2 + \cdots\right] - Pb_3 \quad (8)$$

$$b_1 = 3K_{S0}\left(C_{ij}'^0 - b_3\right) - 7C_{ij}^0 \quad (9)$$

$$b_2 = 3K_{S0}'\left(b_1 + 7C_{ij}^0\right) - 16b_1 - 49C_{ij}^0 \quad (10)$$

$$f = (1/2)[(V_0/V)^{\frac{2}{3}} - 1] \quad (11)$$

where $C_{ij}^{0}(300\ K)$ is the derived elastic constant from measurements at ambient pressure and temperature (300 K) and is thus fixed for the further modelling, $C_{ij}^{0}(T)$ is the elastic constant at high temperature and ambient pressure, $C_{ij}^{0}$ and $C_{ij}^{\prime 0}$ is the elastic constant at ambient conditions and its first pressure derivative, respectively, and $V_0$ and $V$ are the unit-cell volumes at ambient conditions and at high pressures, respectively.

Table 3.1: Elastic moduli of single-crystal ferropericlase $(Mg_{0.94}Fe_{0.06})O$ at ambient pressure as a function of experimental temperatures.

| | $K_{S0}$ (GPa) | $G_0$ (GPa) | $C_{11}$ (GPa) | $C_{12}$ (GPa) | $C_{44}$ (GPa) |
|---|---|---|---|---|---|
| 300 K | 160(2) | 121(1) | 283(3) | 101(2) | 146(2) |
| 550 K | 157(2) | 116(1) | 270(4) | 102(2) | 142(2) |
| 750 K | 153(3) | 112(2) | 258(4) | 103(2) | 139(2) |
| 900 K | 151(3) | 108(2) | 248(4) | 104(3) | 137(2) |

Table 3.2: Comparison of the elastic moduli at ambient conditions.

| | Composition | $K_{S0}$ (GPa) | $G_0$ (GPa) | $C_{11}$ (GPa) | $C_{12}$ (GPa) | $C_{44}$ (GPa) |
|---|---|---|---|---|---|---|
| This study | $(Mg_{0.94}Fe_{0.06})O$ | 160(2) | 121(1) | 283(3) | 101(2) | 146(2) |
| Jackson et al. (2006) | $(Mg_{0.94}Fe_{0.06})O$ | 163(3) | 121(2) | 284(3) | 103(1) | 147(1) |
| Jacobsen et al. (2002) | $(Mg_{0.94}Fe_{0.06})O$ | 161(3) | 121(2) | 281(2) | 101(2) | 147(1) |
| Marquardt et al. (2009) | $(Mg_{0.9}Fe_{0.1})O$ | 164(1) | 116(1) | 280(1) | 102(1) | 142(1) |
| Sinogeikin and Bass (1999) | MgO | 163.2(10) | 130.2(10) | 297.9(15) | 95.8(10) | 154.4(20) |
| Karki et al. (1997)* | MgO | 158 | 121.8 | 291 | 91 | 139 |

*Theoretical calculation

Table 3.3: Comparison of the temperature and pressure derivatives of the single-crystal elastic moduli of ferropericlase.

| **Temperature Derivatives** | Composition | $(\partial K_S/\partial T)_P$ (MPa/K) | $(\partial G/\partial T)_P$ (MPa/K) | $(\partial C_{11}/\partial T)_P$ (MPa/K) | $(\partial C_{12}/\partial T)_P$ (MPa/K) | $(\partial C_{44}/\partial T)_P$ (MPa/K) |
|---|---|---|---|---|---|---|
| This study | $(Mg_{0.94}Fe_{0.06})O$ | -15.4(1.1) | -21.3(9) | -58.1(2.2) | 4.9(4) | -15.1(4) |
| Karki et al. [1999]* | MgO | -14.0 | -21.6 | -59.8 | 8.9 | -8.8 |
| Wu and Wentzcovitch (2014)* | $(Mg_{0.875}Fe_{0.125})O$ | -12 | -11 | | | |
| **Pressure Derivatives** | Composition | $(\partial K_S/\partial P)_T$ | $(\partial G/\partial P)_T$ | $(\partial C_{11}/\partial P)_T$ | $(\partial C_{12}/\partial P)_T$ | $(\partial C_{44}/\partial P)_T$ |
| This study | $(Mg_{0.94}Fe_{0.06})O$ | 4.0(2) | 2.1(1) | 8.3(2) | 1.5(1) | 1.0(1) |
| Jackson et al.[2006] | $(Mg_{0.94}Fe_{0.06})O$ | 3.9(2) | 2.1(1) | 8.35 | 1.42 | 0.89 |
| Yang et al. [2015] | $(Mg_{0.92}Fe_{0.08})O$ | | | 8.99(0.1) | 1.95(0.12) | 1.22(0.1) |
| Marquardt et al. [2009] | $(Mg_{0.9}Fe_{0.1})O$ | 3.98(14) | | 8.71(15) | 1.74(14) | 0.84(18) |
| Jacobsen et al. [2005] | $(Mg_{0.76}Fe_{0.24})O$ | 4.17 | 2.7(1) | 9.3(2) | 1.3(6) | 1.2(1) |
| Jacobsen et al. [2005] | $(Mg_{0.44}Fe_{0.56})O$ | 4.17 | 1.5(1) | 9.6(4) | 1.5(4) | -0.16(9) |
| Sinogeikin and Bass [1999] | MgO | 4.0(1) | 2.4(1) | 9.05(20) | 1.34(15) | 0.84(20) |
| Karki et al.[1999]* | MgO | 4.15 | 2.44 | 9.56 | 1.45 | 1.03 |

*Theoretical calculation

Using the derived elastic constants of the sample, the aggregate adiabatic bulk ($K_S$) and shear moduli ($G$) were calculated using the Voigt-Ruess-Hill averages [*Hill*, 1952] (Figure 3.5a, b):

$$K_S = C_{11} - 2C/3, \tag{12}$$

$$G = \left[\left(C/5 + {}^{3C_{44}}/_{5}\right) + 5C_{44}C/(4C_{44} + 3C)\right]/2, \tag{13}$$

$$C = C_{11} - C_{12}. \tag{14}$$

The derived $K_{S0}$and $G_0$ at ambient conditions are 160(2) GPa and 121(1) GPa, respectively, which are fixed for further thermoelastic modeling. The aggregate velocities of the sample (Figure 3.5 c, d) are calculated using the equations:

$$V_P = \sqrt{{(K_S + 4G/3)}/{\rho}}, \tag{15}$$

$$V_S = \sqrt{G/\rho} \tag{16}$$

The P-T derivatives of the reference isotropic elastic moduli were obtained by fitting the moduli either at constant T, using the third-order Eulerian finite-strain equations [Birch, 1978], or at constant P using linear equation:

$$K_{S0}(T) = K_{S0}(300\ K) + (T - 300)(\partial K_S/\partial T)_P \tag{17}$$

$$K_S = K_{S0}(1+2f)^{5/2}\left\{1 + \left[3K_{S0}^{'} - 5\right]f + 1/2[9K_{S0}^{'\,2} - 36K_{S0}^{'} + 35]f^2\right\} \tag{18}$$

$$G_0(T) = G_0(300\ K) + (T - 300)(\partial G/\partial T)_P \tag{19}$$

$$G = (1+2f)^{5/2}\{G_0 + [3G_0'K_{S0} - 5G_0]f + 9[K_{S0}^2[(1/K_{S0})(K_{S0}^{'} - 4G_0')] + 35G_0/9]f^2\} \tag{20}$$

where $K_{S0}$ and $G_0$ are the derived elastic moduli from measurements with ambient pressure and temperature (300 K), $K_{S0}(T)$ and $G_0(T)$ are the elastic moduli at high temperature and ambient pressure, $K_{S0}^{'}$ and $G_0'$ are the first pressure derivatives of the elastic moduli, and *f* is the Eulerian strain. A self-consistent density model was adopted to determine the finite strain parameters for elastic moduli [Speziale and Duffy, 2002]. Density from the XRD results were first used for the initial finite-strain fitting. The derived $K_S$ and $K_{S0}'$ were converted to the isothermal bulk modulus ($K_T$) and its pressure derivative at constant temperature $K_{T0}'$ using the following thermodynamic relations [*Poirier*, 2000]:

$$K_{T0} = K_{S0}/(1 + \alpha_0\gamma_{0T}T) \tag{21}$$

$$K_{T0}' \cong (1 + \alpha_0\gamma_0 T)^{-1}[K_{S0}' - (\frac{\gamma_0 T}{K_{T0}})(\partial K_T/\partial T)_{P0}] \tag{22}$$

where $(\partial K_T/\partial T)_{P0}$ is the temperature derivative of $K_T$ at ambient pressure, $K_{T0}$ is the isothermal bulk modulus at ambient conditions, $\alpha_0$ is the thermal expansion coefficient, and $\gamma_0$ is the Grüneisen parameter. The isothermal parameter $K_{T0}'$was then used to fit the P-V-T relation to obtain refined density. The procedure was iterated until both $K_T$ and $K_{T0}'$ values were convergent and self-consistent with the input P-V-T relation. Thermoelastic

results from XRD are used to derive for these parameters: $(\partial K_T/\partial T)_{P0} = -0.01$ GPa K$^{-1}$ and $\alpha_0 = 3.0 \times$ 10-5 K$^{-1}$ at 300 to 900 K temperature conditions. The literature value $\gamma_{0T} = 1.443$ is used for the conversion [*Tange et al.*, 2009].

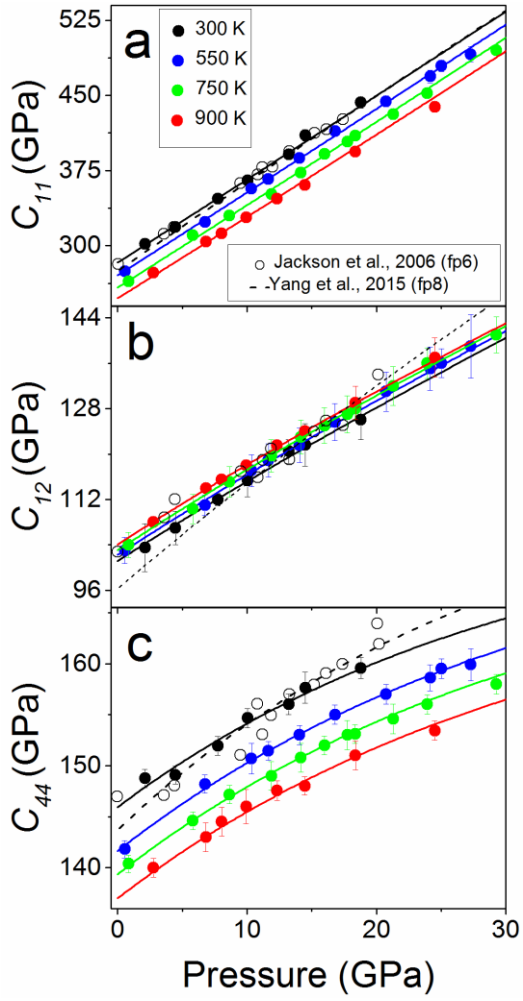


Figure 3.4: Elastic constants of the single-crystal ferropericlase $(Mg_{0.94}Fe_{0.06})O$ as a function of pressure and temperature. Solid lines: fitted results with a third-order finite-strain equation. Open circles: Jackson et al. [2006]; dash lines: Yang et al. [2015].

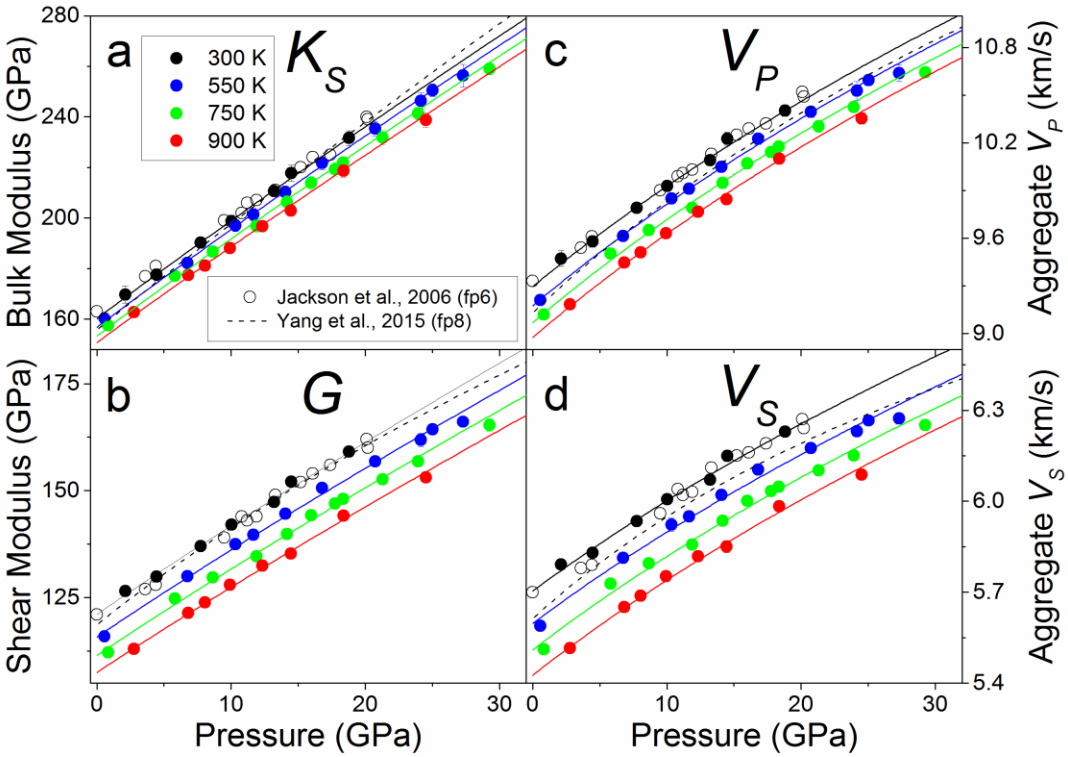


Figure 3.5: Aggregate elastic moduli and velocities of ferropericlase $(Mg_{0.94}Fe_{0.06})O$ as function of pressure and temperature. Solid lines: fits to experimental data using a third-order finite strain equation. Open circles: Jackson et al. [2006]; dash lines: Yang et al. [2015]

## 3.4 Discussion and Implications

### 3.4.1 High-Temperature Effects on the Seismic Parameters of Ferropericlase

Knowledge of the elastic anisotropy ($A$), Poisson's ratio (υ), and $V_P/V_S$ ratio of ferropericlase at high P-T may shed light on understanding seismic anisotropy within the Earth's lower mantle. For the cubic ferropericlase, the elastic anisotropy factor ($A$) can be expressed as:

$$A = \frac{2C_{44} + C_{12}}{C_{11}} - 1 \tag{23}$$

The Poisson's ratio (υ) can be expressed as:

$$\upsilon = \frac{1}{2}\frac{(V_P/V_S)^2 - 2}{(V_P/V_S)^2 - 1} \quad (24)$$

Analysis of these parameters using our data shows that A decreases with increasing pressure but increases with increasing temperature (Figure 3.6). At ambient pressure, *A* is 0.39 at 300 K and 0.53 at 900 K, respectively. The anisotropy decreases to zero at both ~20 GPa, 300 K and at ~24 GPa, 900 K. As temperature was increased from 300 K to 900 K, $V_P/V_S$ and $v$ increased by ~ 2% and ~6% respectively. Compared to MgO [*Sinogeikin and Bass*, 2000], A for fp6 is 8% higher at ambient conditions, whereas $V_P/V_S$ and $v$ are respectively increased by ~1.4% and ~7%. These results show both addition of Fe and elevated temperature can increase elastic-wave anisotropy, whereas pressure suppresses the anisotropy but increases $V_P/V_S$ and $\upsilon$ at high P-T.

To apply these seismic parameters to relevant lower mantle conditions, we have also used thermoelastic modeling to calculate the $V_P/V_S$ ratio, Poisson's ratio, and anisotropy factor to extrapolate the P-T derivatives of elastic constants along a representative lower-mantle geotherm with a reference temperature of 1873 K at 670 km depth [*Brown and Shankland*, 1981] up to 50 GPa, equivalent to a depth of 1250 km (Figure 3.6d, e, f). The pressure range was limited to mid-lower mantle values in order to remove the effects of the Fe spin transition, which can significantly affect modeling outcomes [*Yang et al.*, 2015]. From 660 km to 1250 km, $V_P/V_S$ varies from 1.736 to 1.760 while $\upsilon$ ranges from 0.25 to 0.26, which are generally consistent with seismic models [*Saltzer et al.*, 2004]. The anisotropy factor of ferropericlase is 0.13 at 660 km, decreases to 0 at 900 km, and then its absolute value increases monotonically with increasing pressure to 0.12 at 1250 km, suggesting that ferropericlase is highly anisotropic at depths below the mid-lower mantle.

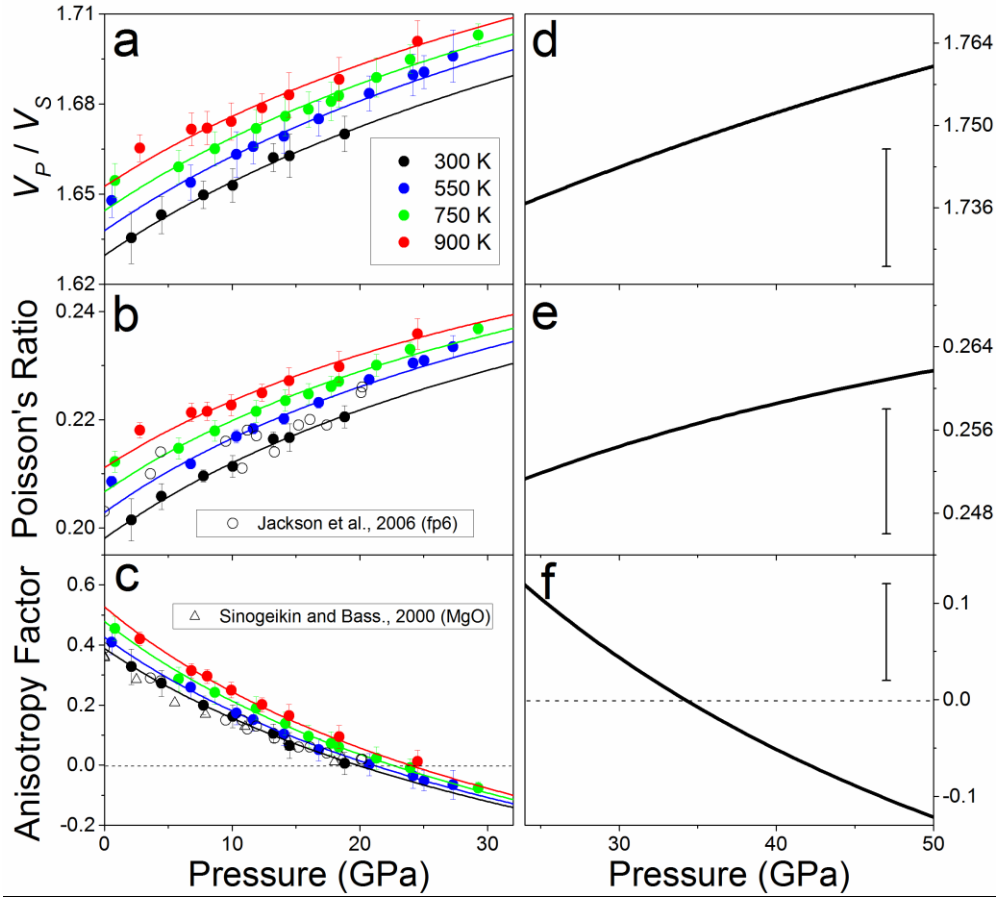


Figure 3.6: Seismic parameters of single-crystal ferropericlase $(Mg_{0.94}Fe_{0.06})O$ as a function of pressure and temperature. (a) $V_P/V_S$ ratio; (b) Poisson's ratio; (c) Anisotropy factor. The anisotropy factor is defined as $A = [(2C_{44} + C_{12}) / C_{11}] - 1$. Lines are calculated from fitted results of the elastic constants and moduli (see Figures. 3.3 and 3.4 for these parameters). Open circles: Jackson et al. (2006); triangles: Sinogeikin and Bass (2000) (d) $V_P/V_S$ ratio; (e) Poisson's ratio; (f) Anisotropy factor along an expected geotherm of the lower mantle [*Brown and Shankland*, 1981]. Representative error bars are estimated using standard error propagation from the modeled parameters (1σ).

### 3.4.2 Seismic Anisotropy in the Lower Mantle

To quantify seismic anisotropy of ferropericlase under lower mantle conditions, we have calculated the $V_P$ anisotropy ($AV_P$) and shear wave splitting factor ($AV_S$) along a representative geotherm using the following equation [*Mainprice et al.*, 2000]:

$$AV_i = 100 \times \frac{V_{i,max} - V_{i,min}}{V_{i,aggre}} \quad (25)$$

where $V_{i,\ max}$, $V_{i,\ min}$, and $V_{i,\ aggre}$ are the maximum, minimum, and aggregate $V_P$ or $V_S$ velocities. At 660 km and 1873 K, the A$V_P$ is 4% and A$V_S$ is 9%, and the difference between the orthogonally polarized $V_{SV}$ and $V_{SH}$ is 0.51 km/s. At 2000 km and 2250 K, the A$V_P$ is 9.7% and A$V_S$ is as high as 22.5%, whereas the difference between $V_{SH}$ and $V_{SV}$ is 1.6 km/s. These extrapolated results show that both $V_P$ and $V_S$ anisotropy increases with depth and that the anisotropy of ferropericlase increases with increasing temperature at lower mantle conditions. Close to the core-mantle boundary, the splitting is expected to be even higher due to the steep thermal gradient within the D" layer. The enhanced A$V_P$ and A$V_S$ observed here, together with the tendency of ferropericlase to develop stronger fabrics [*Yamazaki and Karato*, 2001], support the notion that ferropericlase can significantly contribute to seismic anisotropy in lowermost lower mantle.

### 3.4.3 Thermally Induced Heterogeneity Ratios along a Lower Mantle Geotherm

The thermal or chemical origins of seismic heterogeneity can be constrained by comparing the observed ratios of various seismic parameters with mineral physics results. The ratios of first-order interest include the shear-wave to compressional-wave ratio ($R_{S/P} = \partial \ln V_S / \partial \ln V_P$), bulk sound to shear wave velocity ratio ($R_{\varphi/S} = \partial \ln V_\varphi / \partial \ln V_S$), and density to velocity ratio ($R_{\rho/S,P} = \partial \ln \rho / \partial \ln V_{S,P}$). The contributions of these ratios to lateral heterogeneity can have thermal and/or chemical origins. Mineral physics studies have indicated that $R_{S/P} = \partial \ln V_S / \partial \ln V_P$ is less than 2-2.5 in an iso-chemical lower mantle, which also implies that variations in shear-wave and bulk-wave velocity are positively correlated [*Karato and Karki*, 2001]. Other studies have found a negative correlation between shear-wave and bulk-wave velocity, either throughout the entire lower mantle [*Su and Dziewonski*, 1997] or limited to the mid-lower mantle [*Masters et al.*, 2000]. Most studies

show that $R_{S/P}$ is ~1.5 at the top of the lower mantle and as high as 3.5 at the core-mantle boundary [*Koelemeijer et al.*, 2016; *Masters et al.*, 2000; *Robertson and Woodhouse*, 1996].

Here we have calculated thermally-induced lateral variations in shear-wave and compressional-wave $\partial \ln V_{P,S}/\partial T$ for ferropericlase with 6% Fe (this study) and bridgmanite from a high P-T ultrasonic study [*Li and Zhang*, 2005] to investigate the thermal variation of these two major lower-mantle minerals (Figures 3.7). The velocities of ferropericlase and bridgmanite were first extrapolated along the geotherm based on the derived thermoelastic parameters and finite strain theory. 200 K positive and negative temperature perturbations were applied to the velocities to determine the $\partial \ln V_S/\partial T$ and $\partial \ln V_P/\partial T$ for ferropericlase and bridgmanite. The pressure dependence of $R_{S/P} = \partial \ln V_S/\partial \ln V_P$ of ferropericlase and bridgmanite are shown in Figure 3.8b. For ferropericlase, the $R_{S/P}$ value decreases from 1.48 at 0 GPa to 1.43 at 40 GPa. In contrast, the $R_{S/P}$ value of bridgmanite increases from 1.51 to 1.53 over the same pressure interval.

In order to compare these results with seismic models of the Earth's lower mantle, we have calculated the $R_{S/P}$ value along an expected geotherm for the simplified pyrolite model [*Brown and Shankland*, 1981] consisting of 20% ferropericlase and 80% bridgmanite [*Irifune et al.*, 2010]. In order to take the effect of Fe content into account, the elastic properties of ferropericlase with $X$Fe = 0.20 ($Mg_{0.8}Fe_{0.2}O$) were derived by assuming a linear compositional effect of FeO on elasticity of ferropericlase using data from MgO [*Sinogeikin and Bass*, 2000], $Mg_{0.94}Fe_{0.06}O$, $Mg_{0.92}Fe_{0.08}O$ [*Yang et al.*, 2015], and $Mg_{0.9}Fe_{0.1}O$ [*Marquardt et al.*, 2009a]. Assuming the Fe and Mg partitioning coefficient between bridgmanite (Bgm) and ferropericlase (fp), $K_D = (\frac{Fe}{Mg})^{brg} / (\frac{Fe}{Mg})^{fp} = 0.5$, is pressure independent above ~40 GPa [*Irifune et al.*, 2010], thermoelastic properties of bridgmanite with $X$Fe = 0.10 $(Mg_{0.9}Fe_{0.1})SiO_3$ were adopted to model the velocity and

seismic parameters [*Li and Zhang*, 2005]. The thermoelastic parameters used for ferropericlase and bridgmanite in the following calculations are given in Table 3.4.

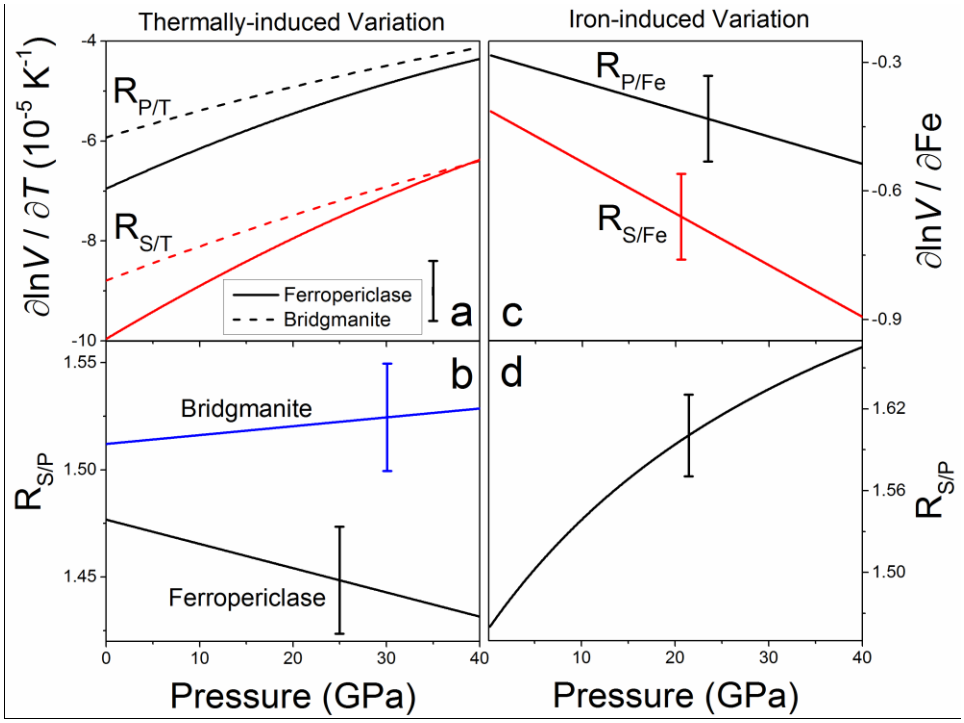


Figure 3.7: Pressure dependence of the thermally induced and Fe induced lateral variation of ferropericlase $(Mg_{0.94}Fe_{0.06})O$ in the compressional and shear wave velocity along a representative geotherm [*Brown and Shankland*, 1981]. (a) $R_{P/T} = \partial \ln V_P / \partial T$ and $R_{S/T} = \partial \ln V_S / \partial T$; (b) thermally induced heterogeneity ratio $R_{S/P} = \partial \ln V_S / \partial \ln V_P$. Dashed lines are calculated results of bridgmanite (Bgm) for comparison [*Li and Zhang*, 2005]. (c) $R_{P/Fe} = \partial \ln V_P / \partial X_{Fe}$ and $R_{S/Fe} = \partial \ln V_S / \partial X_{Fe}$; (d) Fe chemically induced heterogeneity ratio $R_{S/P} = \partial \ln V_S / \partial \ln V_P$. Representative error bars are estimated using standard error propagation from the modeled parameters.

Table 3.4: Thermoelastic parameters for ferropericlase (fp20) $(Mg_{0.8}, Fe_{0.2})O$ and bridgmanite (Bgm10) $(Mg_{0.9}, Fe_{0.1})SiO_3$ used in modeling the pyrolite aggregate.

| | **$(Mg_{0.8}, Fe_{0.2})O$** | **$(Mg_{0.9}, Fe0_{.1})SiO_3$** |
|---|---|---|
| Volume percentage (%) | 20 | 80 |
| Density (g/cm$^3$) | 4.101 | 4.217 |
| $K_S$ (GPa) | 160 | 253 |
| $K_S$' | 4.0 | 4.4 |
| $\partial Ks/\partial T$ (GPa/K) | -0.0154 | -0.02 |
| $G$ (GPa) | 102 | 173 |
| $G$' | 2.1 | 2.0 |
| $\partial G/\partial T$ (GPa/K) | -0.0213 | -0.028 |
| $\alpha$ (K$^{-1}$) | $3.0\times10^{-5}$ | $1.9\times10^{-5}$ |

The volume-weighted aggregate velocity profiles with depth for the simplified (excluding calcium silicate perovskite) pyrolite model are approximately consistent with PREM [*Dziewonski and Anderson*, 1981] (Figure 3.8). Positive and negative temperature perturbations by 200 K were also applied to determine the temperature variation of the aggregate velocity, $\partial \ln V_S/\partial T$ and $\partial \ln V_P/\partial T$. The $R_{S/P} = \partial \ln V_S/\partial \ln V_P$ value of the pyrolite model shows a decrease with increasing depth (Figure 3.9). We should note that recent studies have reported significant changes of the $K_D$ value as a result of the spin transition such that Fe preferentially partitions into ferropericlase [Irifune et al., 2010]. The effect of the spin transition on the seismic parameters needs to be further considered. Since the $R_{S/P}$ value can be significantly influenced by temperature-dependent anelasticity in the deep Earth, the predicted $R_{S/P}$ correction of ~0.2 for the anelasticity effect between 660-1600 km is also taken into account [*Matas and Bukowinski*, 2007](Figure 3.9). Our data are consistent with most seismic observations within uncertainty for the upper part of the lower mantle including MCDRT12 [*Mosca et al.*, 2012], HMSL08 [*Houser et al.*, 2008], and SP12RTS [*Koelemeijer et al.*, 2016]. We thus conclude that the thermal origin is dominant

for the upper 1500 km of the lower mantle, which is in agreement with some seismic predictions [*Simmons et al.*, 2010]. Although most of the seismic models show a high $R_{S/P}$ value in the middle part of the lower mantle [*Koelemeijer et al.*, 2016; *Mosca et al.*, 2012], our data did not predict such a high $R_{S/P}$ value for the high-spin ferropericlase and bridgmanite. This may suggest other causes predominate in these regions, such as the Fe spin transition or a contribution from chemically-induced heterogeneity [*Kaneshima and Helffrich*, 2010; *Simmons et al.*, 2010; *Wu and Wentzcovitch*, 2014].

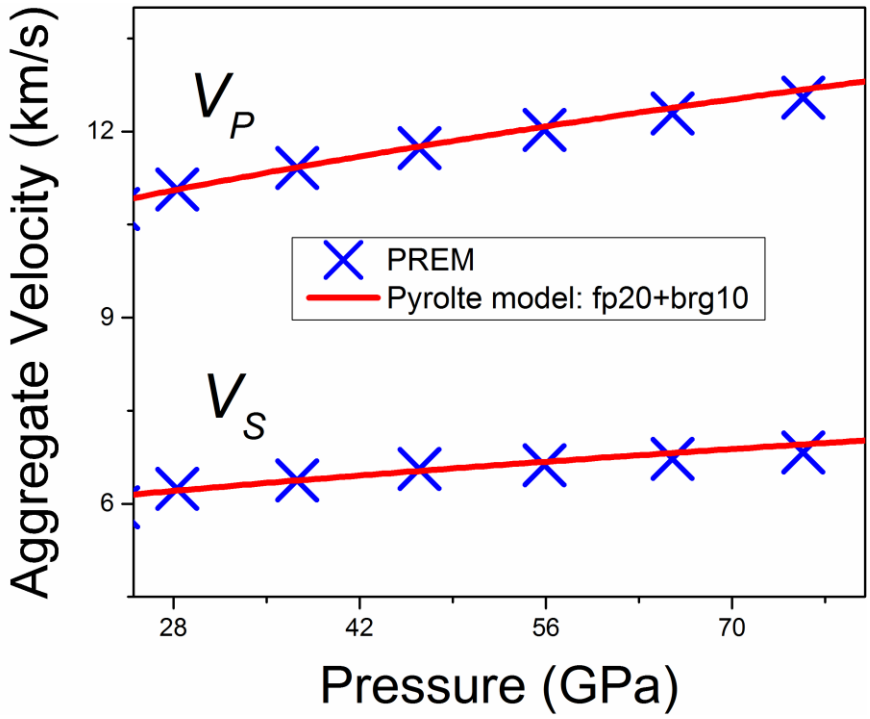


Figure 3.8: Comparison of the aggregate velocity between a simplified pyrolite model and PREM. Lines: simplified pyrolite model with 20% ferropericlase with 20% of iron (fp20) and 80% bridgmanite with 10% of iron (Bgm10) [*Li and Zhang*, 2005]; Crosses: PREM seismic model [*Dziewonski and Anderson*, 1981].

### 3.4.4 Effects of Fe and Fe Spin Transition on the Seismic Heterogeneity

Variation in Fe content in major lower-mantle minerals is regarded as a potential chemical cause for seismic heterogeneities below the mid-lower mantle [*van der Hilst and Kárason*, 1999]. A major change in Fe-partitioning between ferropericlase and bridgmanite is expected to occur in the top of the lower mantle due to the Al dissolution in bridgmanite and in the mid-lower mantle due to the Fe spin transition in ferropericlase [*Irifune et al.*, 2010; *Muir and Brodholt*, 2016]. The amount of iron in the Earth's lower-mantle minerals can affect a wide range of elastic properties of the host minerals, including velocity, elastic constants, and shear modulus [*Jacobsen et al.*, 2002; *Yang et al.*, 2015]. Previous studies have shown that Fe substitution in ferropericlase increases its density but reduces the $V_P$, $V_S$, and shear modulus [*Jacobsen et al.*, 2002; *Jacobsen et al.*, 2004], causing an anti-correlation between bulk and shear velocities with Fe enrichment, which has previously been interpreted as chemical heterogeneity in the deep Earth [*Kellogg et al.*, 1999; *Tackley*, 2000]. For example, the effect of Fe content on seismic heterogeneity can be evaluated with $\partial \ln V_S / \partial X\mathrm{Fe} = -0.5 \pm 0.1$ and $\partial \ln V_P / \partial X\mathrm{Fe} = -0.4 \pm 0.1$, based on the experimental results at ambient pressure [*Karato and Karki*, 2001]. Here we have calculated the velocity variations with Fe content in ferropericlase ($\partial \ln V_S / \partial X\mathrm{Fe}$ and $\partial \ln V_P / \partial X\mathrm{Fe}$) to understand the potential influence of Fe variability on lateral velocity anomalies in the lower mantle. We have calculated relative variations of $V_S$ and $V_P$ with Fe content by considering previous elasticity data from MgO [*Sinogeikin and Bass*, 2000], ferropericlase with $X\mathrm{Fe} = 0.06$ (this study), ferropericlase with $X\mathrm{Fe} = 0.08$ [*Yang et al.*, 2015] and ferropericlase with $X\mathrm{Fe} = 0.10$ [*Marquardt et al.*, 2009a]. At constant temperature, the calculated $\partial \ln V_S / \partial X\mathrm{Fe}$ decreases from −0.41 at 0 GPa to −0.89 at 40 GPa while $\partial \ln V_P / \partial X\mathrm{Fe}$ decreases from −0.28 at 0 GPa to −0.54 at 40 GPa (Figure 3.7c, d). Meanwhile, $R_{S/P}$ shows an increasing trend from 1.46 at 0 GPa to 1.67 at 40 GPa, which is in contrast to the downward-trending

thermal variation for the lower part of lower mantle. These results indicate chemically-induced seismic heterogeneity may become dominant in the lower parts of the lower mantle. The predominance of chemically-influenced heterogeneity in terms of Fe distribution is consistent with some seismic studies [*van der Hilst and Kárason*, 1999], especially when Fe is preferentially partitioned into ferropericlase at high pressure [*Irifune et al.*, 2010].

An alternative source of seismic heterogeneity may be the spin transition of Fe in ferropericlase in the mid-part of the lower mantle [*Wu and Wentzcovitch*, 2014]. The $R_{S/P}$ heterogeneity ratio of a homogenous pyrolite aggregate is as high as ~3.5 over the ~1500 to 2000 km depth (Figure 3.9) where spin crossover occurs in ferropericlase. The spin transition in ferropericlase can also produce an anti-correlation between shear-wave velocity and bulk sound velocity in chemically homogeneous pyrolite aggregates, which is observed in tomography models at certain depths [*Wu and Wentzcovitch*, 2014]. Our results with high-spin ferropericlase show clear discrepancy on the $R_{S/P}$ heterogeneity ratio at depth below ~1500 km. Thus, high-spin ferropericlase alone cannot produce such a robust increase of $R_{S/P}$ value in the mid-part of lower mantle, which implies that spin crossover of ferropericlase is a likely cause of observed lateral seismic heterogeneity in the mid-lower mantle.

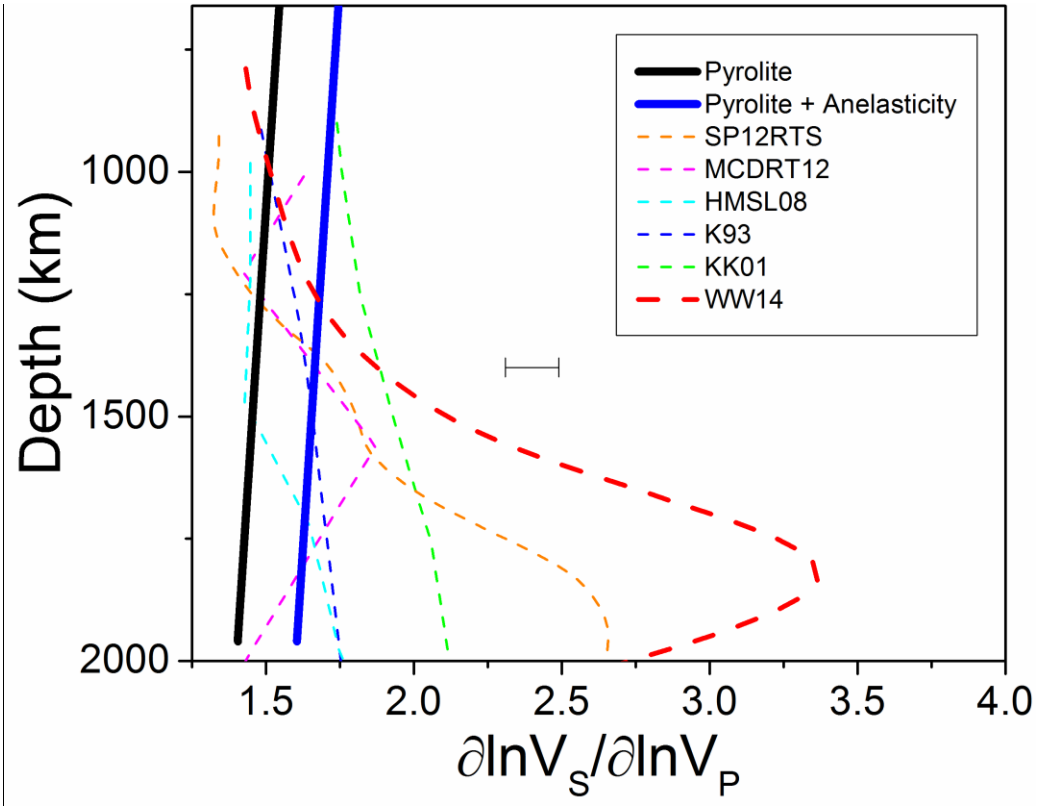


Figure 3.9: Depth profile of the thermally induced heterogeneity ratios ($R_{S/P}$= $\partial \ln V_S / \partial \ln V_P$) for a simplified pyrolite compositional model along a representative geotherm [*Brown and Shankland*, 1981]. Solid black line: simplified pyrolite model with 20% ferropericlase (fp20) and 80% bridgmanite (Bgm10) [*Li and Zhang*, 2005]. Solid blue line: profile corrected for anelasticity effect on the heterogeneity ratio of pyrolite. Mineral physic models for thermal lateral variations are shown as K93 with blue dashed line [*Karato*, 1993], KK01 with green dashed line [*Karato and Karki*, 2001], and WW14 with red dash line [*Wu and Wentzcovitch*, 2014]. Seismic models are shown as magenta dashed line: MCDRT12, a normal-mode data derived models [*Mosca et al.*, 2012]; cyan dashed line: HMSL08, a model employing primarily body-wave data [*Houser et al.*, 2008]; orange dashed line: SP12RTS, a model derived from combined Rayleigh wave phase velocities, body-wave travel-times and normal-model splitting function measurements [*Koelemeijer et al.*, 2016]. Error bars are estimated using standard error propagation from the modeled parameters.

**Acknowledgements**

We acknowledge S. Grand, C. Lu, S. Fu, and I. Yen for their constructive suggestions and discussions. We also thank Z. Mao, Y. Wu, and D. Fan for their assistance in the BLS spectra collection at 13 BMD, GSECARS. We thank GSECARS and Advanced Photon Source for providing X-ray diffraction facilities for the study. J.F.L. acknowledges support from the Geophysics and CSEDI Programs of the National Science Foundation (NSF) and HPSTAR. S.D.J. acknowledges support from NSF EAR-0748707, the David and Lucile Packard Foundation, and the Alexander von Humoldt Foundation. GeoSoilEnviroCARS is supported by the National Science Foundation - Earth Sciences **(**EAR-1128799) and Department of Energy Geosciences **(**DE-FG02-94ER14466)**.** The data for this paper are available by contacting the corresponding author at afu@jsg.utexas.edu.

# Chapter 4: Elasticity of Ferropericlase across the Spin Crossover in the Earth's Lower Mantle[2]

The effects of the spin transition on the physics and chemistry of the lower-mantle ferropericlase and perovskite have been suggested to have significant consequences for the seismology and geochemistry. Knowing the elasticity of ferropericlase across the spin transition can help explain seismic and mineralogical models of the lower-mantle including the origin of seismic heterogeneities in the middle to lowermost parts of the lower mantle. However, full elastic constants of ferropericlase within the spin transition and in the low-spin state remains experimentally controversial due to technical challenges in directly measuring sound velocities under lower-mantle conditions. Here we have reliably measured both $V_P$ and $V_S$ of a single-crystal ferropericlase ($(Mg_{0.92},Fe_{0.08})O$) using complementary Brillouin Light Scattering and Impulsive Stimulated Light Scattering coupled with diamond anvil cell (DAC) up to 96 GPa. The derived elastic constants show drastically softened $C_{11}$ and $C_{12}$ within the spin transition at 40-60 GPa while $C_{44}$ is not affected. Based on thermoelastic modelling along an expected geotherm, the spin crossover in ferropericlase can contribute to elastic abnormalities at mid lower-mantle conditions. Our results imply the middle to lowermost parts of the lower mantle would exhibit enhanced seismic heterogeneities due to the occurrence of the mixed-spin and low-spin ferropericlase.

## 4.1 INTRODUCTION

Seismic wave studies of the lower mantle have established relatively reliable seismic models including compressional and shear wave velocities ($V_P$ and $V_S$), density,

[2]This chapter is based on the article: Yang, J., X. Tong, J.-F. Lin, T. Okuchi, and N. Tomioka (2015), Elasticity of ferropericlase across the spin crossover in the Earth's lower mantle, Sci. Rep., 5, 17188.

and incompressibility in one-dimensional, two-dimensional, and three-dimensional tomographic models (e.g., PREM, AK135, S40RTS) [*Dziewonski and Anderson*, 1981; *Kennett et al.*, 1995; *Ritsema et al.*, 2011]. Thus far, it has been shown that most of the lower mantle, except the lowermost mantle such as the D″ layer, exhibit relatively smooth changes in seismic parameters that have been commonly interpreted as a result of the high pressure-temperature (*P-T*) effects on physical properties of candidate minerals in the region. The lower mantle is mostly believed to be seismically and chemically homogeneous, and likely consists of approximately 75% bridgmanite (silicate perovskite $(Mg,Fe)(Al,Fe,Si)O_3$; Pv), 20% ferropericlase ((Mg,Fe)O; Fp), and 5% calcium perovskite ($CaSiO_3$) by volume in a pyrolite compositional model [*Irifune*, 1994; *Ringwood*, 1975]. However, a number of seismic studies have shown that possible thermal and/or chemical heterogeneities, especially in the middle to lower part of the lower mantle ranging from approximately 1500 km to 2800 km in depth, are needed to reconcile differences in our current understanding among seismic, geochemical models and mineral physics results [*Cammarano et al.*, 2010; *Karato and Karki*, 2001; *Kellogg et al.*, 1999; *Matas et al.*, 2007; *Murakami et al.*, 2012]. Other than the bridgmanite to post-perovskite structural transition at the D″ zone region [*Murakami et al.*, 2004], which may be responsible for the seismic discontinuities in the lowermost mantle, the electronic spin transitions of iron in lower-mantle minerals have been suggested to affect our understanding of the mid to lowermost lower-mantle seismic heterogeneities.

The electronic spin transition of iron in lower-mantle bridgmanite and ferropericlase has been recently reported to affect physical and chemical properties of the host minerals, including changes in elasticity, iron partitioning, and electrical and thermal conductivities [*Badro et al.*, 2003; *Badro et al.*, 2004; *Crowhurst et al.*, 2008; *Lin et al.*,

2007a; *Lin et al.*, 2005; *Marquardt et al.*, 2009b; *Tsuchiya et al.*, 2006; *Wentzcovitch et al.*, 2009], that may contribute to seismic heterogeneities of the region. It has been shown that a broad spin crossover occurs in ferropericlase at conditions ranging from 1700 km to 2700 km in depth [*Mao et al.*, 2011b], while the $Fe^{3+}$ in the octahedral site of bridgmanite undergoes a high-spin to low-spin transition at *P-T* conditions relevant to the top lower mantle [*Lin et al.*, 2013]. Of particular interest to our understanding of the deep-mantle seismology and geodynamics is the effects of the spin transition on the elasticity (e.g., sound velocities, equation of states (EoS), and seismic anisotropies) of the lower-mantle minerals, because a thorough knowledge of their elastic properties is essential for interpreting seismic observations as well as for constraining the chemical composition and mineralogical model of the region [*Murakami et al.*, 2012].

In recent years, there have been a number of experimental and theoretical studies on the elasticity of single-crystal ferropericlase across the spin transition at high pressures using various techniques, including Impulsive Stimulated Light Scattering (ISS), Brillouin Light Scattering (BLS), Inelastic X-ray Scattering (IXS), and Density Function Theory (DFT) [*Antonangeli et al.*, 2011; *Crowhurst et al.*, 2008; *Marquardt et al.*, 2009b; *Wu et al.*, 2013; *Wu and Wentzcovitch*, 2014]. DFT calculations have shown that ferropericlase exhibits significant softening in $V_P$ as well as $C_{11}$ and $C_{12}$ elastic constants across the spin crossover at lower-mantle *P-T* conditions, although $V_S$ and $C_{44}$ are not affected by the transition [*Wu et al.*, 2013]. On the other hand, experimental results on the elasticity across the spin transition differ drastically [*Antonangeli et al.*, 2011; *Crowhurst et al.*, 2008; *Marquardt et al.*, 2009a; *Marquardt et al.*, 2009b]. In particular, ISS measurements on $(Mg_{0.94}Fe_{0.06})O$ up to 60 GPa show a remarkable reduction in both $V_P$ and $V_S$ across the spin transition [*Crowhurst et al.*, 2008], although the reliability of deriving the $V_S$ from the

interfacial wave has been questioned. BLS measurements on $(Mg_{0.9}Fe_{0.1})O$ up to 81 GPa showed no substantial reduction of the directly-measured $V_S$ across the spin transition, while the combination of the $V_S$ values from BLS and the EoS parameters from X-ray diffraction have indicated $V_P$ softening by a maximum of 17% within the spin transition [*Marquardt et al.*, 2009a]. High-pressure IXS experiments up to 80 GPa on $(Mg_{0.83}Fe_{0.17})O$, which used acoustic phonon dispersions at very high frequencies to extract the velocities, did not reveal any reduction on either the $V_P$ or the $V_S$ within the spin transition [*Antonangeli et al.*, 2011]. Furthermore, some of these previous studies have indicated that the spin transition can markedly enhance the elastic *Vs* anisotropy of ferropericlase such that the low-spin state becomes much more elastically anisotropic as compared to its high-spin counterpart [*Antonangeli et al.*, 2011; *Marquardt et al.*, 2009b]. The full elastic constants of single-crystal ferropericlase across the spin transition and in the low-spin state can help provide new insights into the effects of the spin transition on thermodynamic and seismic parameters of the sample, but these essential experimental data remain unclear due to the aforementioned controversies. Since these experimental results point to entirely different scenarios in seismic and geochemical models of the lower mantle, seismically homogeneous vs. heterogeneous lower mantle, it remains unclear if the effect of the spin transition on the elasticity of the lower-mantle ferropericlase should be taken into account in our understanding of the seismic models of the lower mantle. Reliable experimental results can also help elucidate recent theoretical predictions on the elasticity and thermodynamics of ferropericlase at high pressures [*Wu et al.*, 2013].

Here we have directly measured $V_P$, $V_S$, and pressure-volume ($P$-$V$) relation of a single-crystal ferropericlase $(Mg_{0.92},Fe_{0.08})O$ in order to solve for its full elastic constants ($C_{ij}$) using combined BLS, ISS, and X-ray diffraction (XRD) measurements in a diamond

anvil cell (DAC) up to 96 GPa (see Methods for details). The combined experimental results overcome previous technical difficulties and permit direct and reliable evaluation of the full elastic constants and thermoelastic parameters across the spin transition at lower-mantle pressures. Our results show that ferropericlase with 8 at.% iron undergoes a spin transition at 40-60 GPa that is associated with elastic constants $C_{11}$ softening by a maximum of 16%, $C_{12}$ by 70%, whereas $C_{44}$ does not show any observable reduction across the transition; within the spin transition, the aggregate *Ks* from Voigt-Reuss-Hill average reduces by 38%, aggregate $V_P$ by 13%, and aggregate $V_S$ is not affected. The $V_P$ anisotropy experiences a 13% maximum increase as compared to its corresponding high-spin state, whereas no abrupt $V_S$ splitting anisotropy increase was observed across the spin transition. The low-spin state also exhibits distinct elastic behavior from that of the high-spin and mixed-spin states. To decipher the geophysical and geochemical consequences of the spin crossover in the deep mantle, we have modelled elastic and seismic parameters of ferropericlase along an expected lower-mantle geotherm [*Brown and Shankland*, 1981]. Our modelled results show that the velocity abnormalities and elastic softening remain significantly strong across the spin crossover in the lower mantle and that the low-spin ferropericlase exhibits significant $V_P$ and $V_S$ enhancements compared to those of the extrapolated high-spin state. These results are applied to understand potential seismic heterogeneities induced by the spin transition in the deep lower mantle.

### 4.2 METHODS

Single-crystal ferropericlase ($(Mg_{0.92},Fe_{0.08})O$) was synthesized via inter-diffusion of Fe and Mg between a single-crystal periclase and pre-synthesized (Mg,Fe)O powder in a $H_2/CO_2$ gas-mixing furnace at the Institute for Study of the Earth's Interior (ISEI) of Okayama University at Misasa. The MgO crystal with a pre-oriented (100) crystallographic

plane purchased from the MTI Corporation was cut down to 7 mm in length by 7 mm wide and 0.25 mm thick, and was sandwiched between two layers of compacted polycrystalline $(Mg_{0.75}Fe_{0.25})O$ powder approximately 1 mm thick each. The starting sample assemblage was then placed in a Pt holder into the furnace operating at 1350 °C and $10^{-2}$ Pa oxygen fugacity for approximately 2 weeks. The synthesized single-crystal ferropericlase was then extracted and polished down to 12 μm close to surface layer (to avoid non-uniform center area) for further sample analyses. Electron microprobe and X-ray diffraction analyses of the sample at The University of Texas at Austin showed that the sample was chemically homogeneous with the chemical composition of $(Mg_{0.92}Fe_{0.08})O$ and a unit cell parameter of $a$ = 4.1996 (4) Å. The (100)-oriented sample was double polished down to approximately 15 μm thick, and cut into squared platelets 50-80 $\mu m$ in length for high-pressure DAC experiments. The orientation of the platelet was confirmed by the single-crystal X-ray diffraction patterns at ambient and high pressure (Figure 4.1 B).

High-pressure X-ray diffraction patterns were collected from the single-crystal sample at room temperature in a DAC at the Sector 13-BMD of the GSECARS of the Advanced Photon Source (APS), Argonne National Lab (ANL) (Figure 4.1). A pair of diamond anvils with 200 μm culets were used to pre-indent a rhenium gasket with an initial thickness of 250 μm to approximately 25 GPa (or approximately 25 μm thick). Consequently, a hole of 120 μm was drilled in the pre-indented area and used as the sample chamber. A piece of the platelet 50 μm in length was loaded into the sample chamber, together with Au powder as the pressure calibrant and Ne as the pressure medium, in a short symmetric DAC. An incident X-ray beam with a wavelength of 0.3344 Å and a focused size of 20 μm (FWHM) in diameter was used for the diffraction experiments (Figures 4.1 and 4.2). X-ray diffraction patterns of the sample were collected at pressure

intervals of 1-3 GPa up to 91 GPa by a MAR CCD by continuously rotating the DAC around the vertical axis of the sample stage by $\pm$15° (Figure 4.2). The unit cell parameters and their uncertainties for the sample were calculated based on four sets of the diffraction peaks corresponding to {200}, {220}, {400} and {420} equivalent reflections (Figure 4.1). The uncertainties of the unit cell parameters are typically on the order of 0.04% and are approximately 0.08% at the highest pressure of 91 GPa, indicating that the sample remained sufficiently high quality for the X-ray diffraction, BLS, and ISS experiments. Analyses of the XRD patterns of the sample also confirmed that the crystal was indeed oriented in the (100) crystallographic plane within approximately $\pm$1° angular uncertainty.

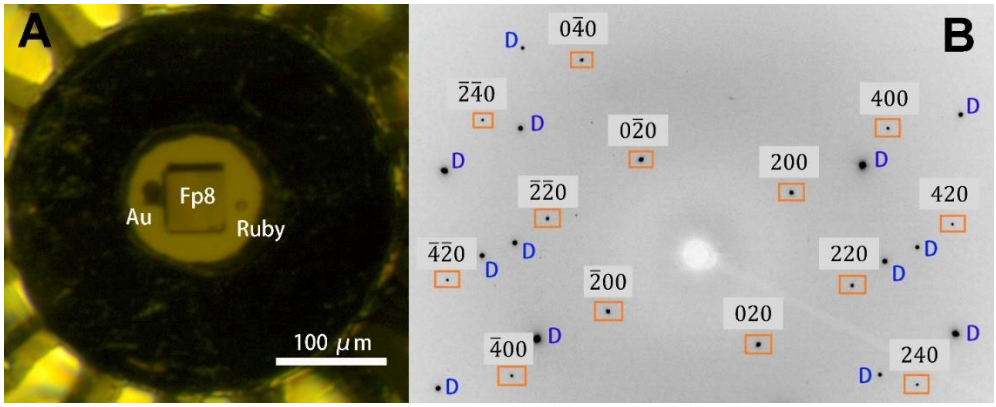


Figure 4.1: Representative sample image and X-ray diffraction pattern of the single-crystal ferropericlase ($Mg_{0.92}Fe_{0.08}$)O at high pressure. (A) Ferropericlase (100) platelet, together with Au and a ruby sphere calibrant [*Fei et al.*, 2007a], loaded into a diamond anvil cell having Ne pressure medium at 13 GPa; (B) Representative X-ray diffraction pattern of the single-crystal ferropericlase at 13 GPa. The diffraction pattern was taken by rotating the diamond cell $\pm$15° about the vertical axis of the sample stage. D: diffraction spots from the diamond anvil.

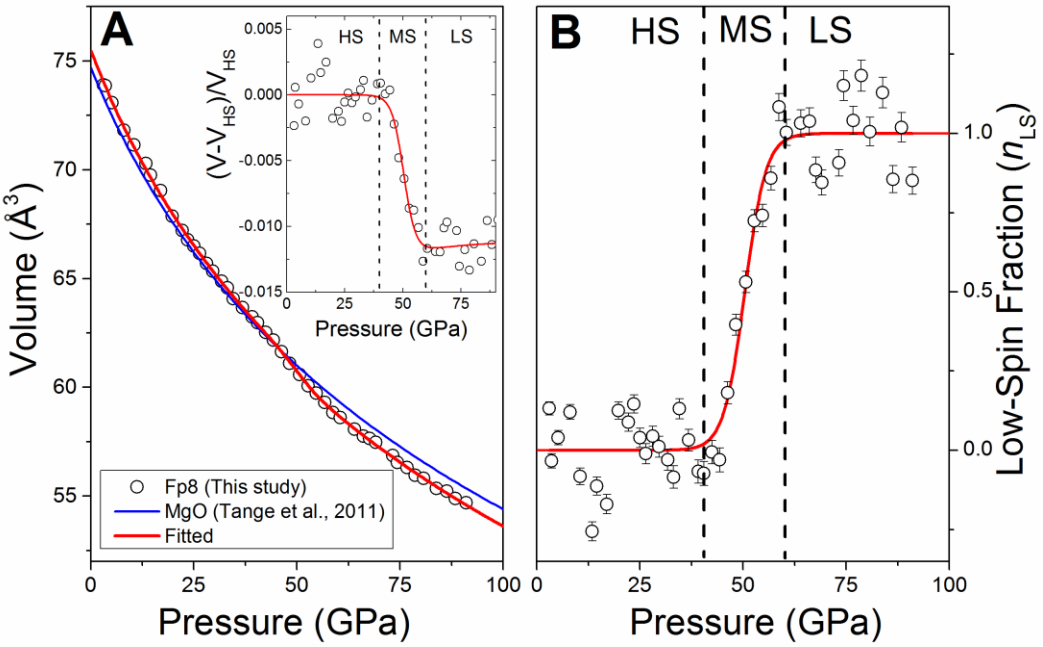


Figure 4.2: Pressure-volume relation and the derived low-spin fraction of iron in the single-crystal ferropericlase ($Mg_{0.92}Fe_{0.08}$)O at high pressures. (A) Pressure-volume relation of ferropericlase. Open circles: unit cell volumes as a function of pressure from experimental X-ray diffraction measurements at 300 K; red line: Birch-Murnaghan EoS fit to the experimental data; blue line: pressure-volume curve of the end-member MgO plotted for comparison[*Tange et al.*, 2009]. The inserted figure shows the volume reduction across the spin transition using the EoS of the high-spin ferropericlase as the reference[*Mao et al.*, 2011b]; (B) Modelled low-spin fraction of the ferropericlase as a function of pressure. The experimental data (open circles) are modelled to derive the low-spin fraction (red line) based on the procedures reported previously [*Mao et al.*, 2011b; *Speziale et al.*, 2005; *Tsuchiya et al.*, 2006]. Vertical dashed lines are plotted to guide the eyes for the high-spin (HS), mixed-spin (MS), and low-spin (LS) regions, respectively.

High-pressure BLS and ISS experiments were performed on the single-crystal ferropericlase at up to 96 GPa in a short symmetric DAC in the Mineral Physics Laboratory of The University of Texas at Austin. Ultralow birefringence and microscopically defect-free diamond anvils were selected for these experiments using a petrographic microscope

under crossed-polar, because we had observed that the pulsed laser of the ISS system with a 1064 nm wavelength could potentially damage diamond anvils having defects and high strained areas. Similar to the sample preparation in the XRD experiments, a pair of diamond anvils with 200 μm culets was used to pre-indent a rhenium gasket and a hole of 120 μm was drilled and used as the sample chamber. A piece of the platelet 50-70 μm in length was loaded, together with a few ruby spheres as the pressure calibrant and Ne as the pressure medium, in a short symmetric DAC. Two runs were conducted for the BLS and ISS experiments (Table 4.2). Pressure uncertainties were determined from measured ruby fluorescence spectra before and after the BLS and ISS measurements. BLS spectra of the sample were collected from the (100) platelet along the [100] and [110] crystallographic directions in the transmitted geometry with a pressure interval of 3-5 GPa up to 96 GPa (Figures. 4.1 and 4.2). The BLS system is equipped with a Coherent Verdi V2 laser operating at 532 nm wavelength and 600 mW laser power, together with a JRS interferometer and an APD detector (Count-10B Photo Counting Module with approximately 5 cps from Laser Components, Inc.). The focused laser beamsize at the sample position was approximately 20 μm in diameter while the scattering angle of the BLS system was set at 48° and calibrated against $SiO_2$ glass and purified water standards. The data collection time was typically 1 hour at pressures below 50 GPa and 2 hours at higher pressures. Analyses of the Brillouin spectra using OriginPro 9.1 software showed strong $V_P$ and $V_S$ peaks with high signal-to-noise ratios at pressures below 20 GPa, while only the $V_S$ peak of the sample was observed at higher pressures as the $V_S$ peak of the diamond anvils saturated the $V_P$ peak of the sample. The measured $V_P$ and $V_S$ velocities of the sample at pressures below 20 GPa were used to derive the full elastic constants of the crystal and also to cross check the reliability of the ISS results at lower pressures (see further discussion below).

High-pressure ISS spectra were also collected from the single-crystal sample along the [100] and [110] crystallographic directions up to 96 GPa (Figure 4.1). The ISS system is a pump-and-probe technique that is equipped with the pump laser with a 1064 nm wavelength and a pulse width of 15 ps and the probe laser with a 532 nm wavelength. The pump laser from Talisker of the Coherent Company was split into two beams which were then recombined at the sample position with a crossing angle of 20.3° and a beam size of 30 μm. The probe laser was delayed by an Aerotech linear stage as long as 20 ns, while the diffracted ISS signals were collected by a photodiode detector. The data collection time for each ISS spectrum was typically 2 hours. Using MATLAB and OriginPro 9.1 software, we implemented the Burg method to analyze the time-domain ISS spectra in order to derive the frequency-domain power spectra and the acoustic wave velocities of the sample at high pressures (Figure 4.1). The derived $V_P$ values from ISS measurements are consistent with those from the BLS measurements at pressures below 20 GPa, confirming the calibration and reliability of both techniques. The interfacial waves were also observed in most of the ISS experiments, but their signals were much weaker than the longitudinal acoustic waves; in fact, the interfacial waves were too weak to be observed in our analyses in some experiments. Given the uncertainties involved in interpretation of the interfacial wave results from ISS experiments, we have only used the $V_P$ from the ISS measurements and the $V_S$ from the BLS experiments, together with the density results from XRD measurements, to derive full elastic constants of the single-crystal ferropericlase at high pressures.

## 4.3 RESULTS AND DISCUSSION

### 4.3.1 Experiments and Thermoelastic Modelling

*P-V* relations of the single-crystal ferropericlase ($(Mg_{0.92},Fe_{0.08})O$) in the (100) platelet were measured using synchrotron X-ray diffraction up to 96 GPa at room temperature in a DAC. These results are used to evaluate the EoS parameters, the width of the spin transition, and the fraction of the high-spin (HS) and low-spin (LS) states in ferropericlase [*Lin et al.*, 2005; *Mao et al.*, 2011b] (Figure 4.1 and Figure 4.2) (See Methods and Appendix A for details of the experiments and modelling). Analysis of the measured *P-V* curve shows that the spin transition occurs over pressures ranging between 40 GPa and 60 GPa, and is associated with a density increase of 1.2% (0.1%). The derived isothermal bulk modulus at ambient conditions ($K_{T0}$) and its pressure derivative ($K_{T0}'$) are: $K_{T0}$ = 152.5 (2.4) and $K_{T0}'$ = 4.1 (0.2) for the HS state, and $K_{T0}$ = 161.6 (7.1) with a fixed $K_{T0}'$ of 4 for the LS state, consistent with previous studies [*Fei et al.*, 2007b] (Figure 4.3). The single-crystal platelet was also used for simultaneously measuring $V_S$ in the BLS experiments and $V_P$ in the ISS experiments along principle [100] and [110] crystallographic axes up to 96 GPa in the Mineral Physics Laboratory of the University of Texas at Austin (Figures 4.4 and 4.5); at relatively lower pressures, the $V_P$ and $V_S$ velocities of the platelet were also measured as a function of the azimuthal angles in order to assure the orientation of the platelets and to further confirm the reliability of our measurements as compared with previous studies (Figure 4.6). Together with *P-V* results from XRD measurements, the measured $V_P$ and $V_S$ velocities of the single-crystal ferropericlase permit direct derivations of the full elastic constants ($C_{11}$, $C_{12}$, $C_{44}$) at high pressures via Christoffel's equations (Figure 4.5). Using the Eulerian finite-strain theory [*Birch*, 1978] and a thermoelastic model for the cubic system [*Wu et al.*, 2013], we have modelled the elastic constants within

the spin transition using formulations reported previously [*Wu et al.*, 2013] (See Appendix A for details). Specifically, the elastic compliances $S_{ij}$ of the crystal across the spin transition are given by:

$$S^{ij}V = n_{LS}S_{LS}^{ij}V_{LS} + (1 - n_{LS})S_{HS}^{ij}V_{HS} - \left(\frac{\partial G_{LS}}{\partial \sigma_j} - \frac{\partial G_{HS}}{\partial \sigma_j}\right)\frac{\partial n_{LS}}{\partial \sigma_i}, \quad [1]$$

where $V$ is the volume, $n_{LS}$ is the LS fraction, $\sigma_i$ and $\sigma_j$ are the $i_{th}$ and $j_{th}$ stress component, respectively, in the Voigt notation, and $G$ is the Gibbs free energy. Basically, this thermalelastic model can be constrained with experimentally determined low-spin fraction ($n_{LS}$) and volume ($V$) derived from equation of state, and elastic constants derived from velocity. To further obtain the pressure-dependent EoS parameters for the HS and LS states, respectively, the elastic constants and the aggregate bulk and shear moduli as a function of pressure are derived by fitting the results to the third-order Eulerian finite-strain equation (Figures 4.5 and 4.7).

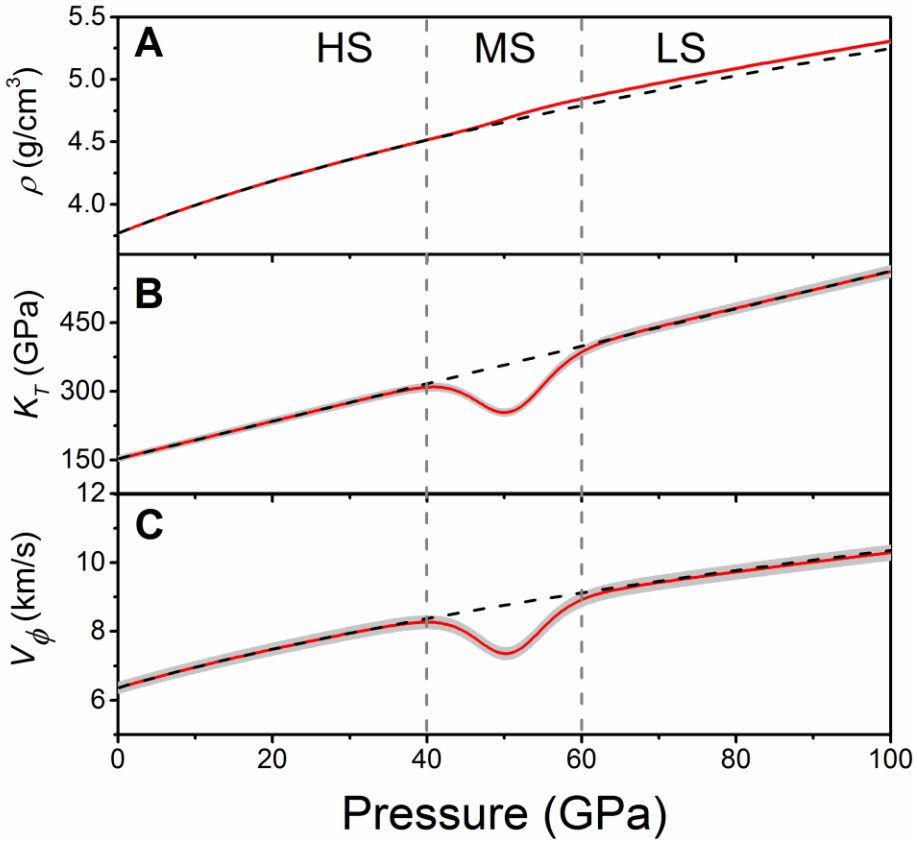


Figure 4.3: Equation of state parameters of the single-crystal ferropericlase ($Mg_{0.92}Fe_{0.08}$)O at high pressures and 300 K. (A) Density ($\rho$); (B) Isotherm bulk modulus ($K_T$); (C) Bulk sound velocity ($V_\Phi$). Red solid lines: modelled EoS parameters across the spin transition; dash lines: extrapolated EoS parameters for the HS ferropericlase. Grey shaded areas show the uncertainties of the parameters calculated from standard error propagations. Error bars (grey shaded areas) for the density are too small to be shown in the figure.

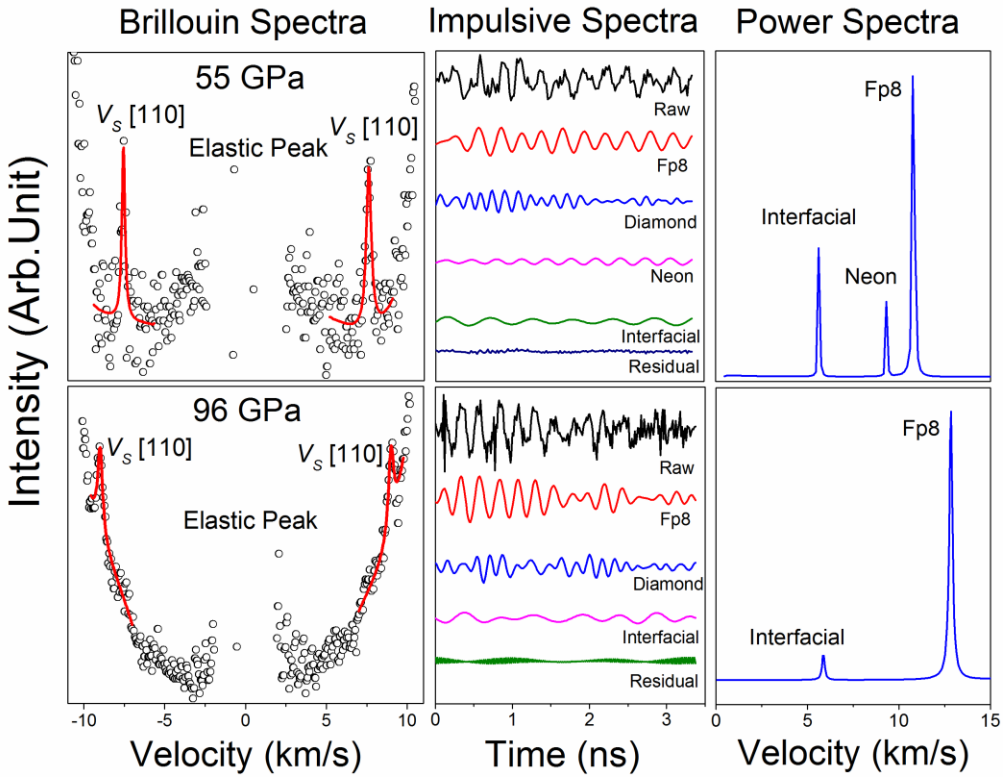


Figure 4.4: Representative Brillouin light scattering (BLS), Impulsive stimulated scattering (ISS), and power spectra of the single-crystal ferropericlase $(Mg_{0.92}Fe_{0.08})O$ along [110] crystallographic axis at high pressures. The BLS spectra were used to derive the $V_S$, while the $V_P$ and the interfacial wave were detected in the ISS spectra. The ISS spectra in the time domain were analyzed and Fourier-transformed to the power spectra in the velocity (frequency) domain to derive the acoustic waves of the sample at high pressures. Neon medium was also observed in the ISS spectra at pressures up to approximately 70 GPa.

Table 4.1: Elasticity of ferropericlase $(Mg_{0.92}Fe_{0.08})O$ in the high-spin and low-spin state at 300 K.

| | $(\partial C_{11}/\partial P)_T$ | $(\partial C_{12}/\partial P)_T$ | $(\partial C_{44}/\partial P)_T$ |
|---|---|---|---|
| **HS** | 8.99 (0.1) | 1.95(0.12) | 1.22(0.10) |
| **LS** | 9.9 (0.2) | 2.2(0.2) | 1.3(0.2) |

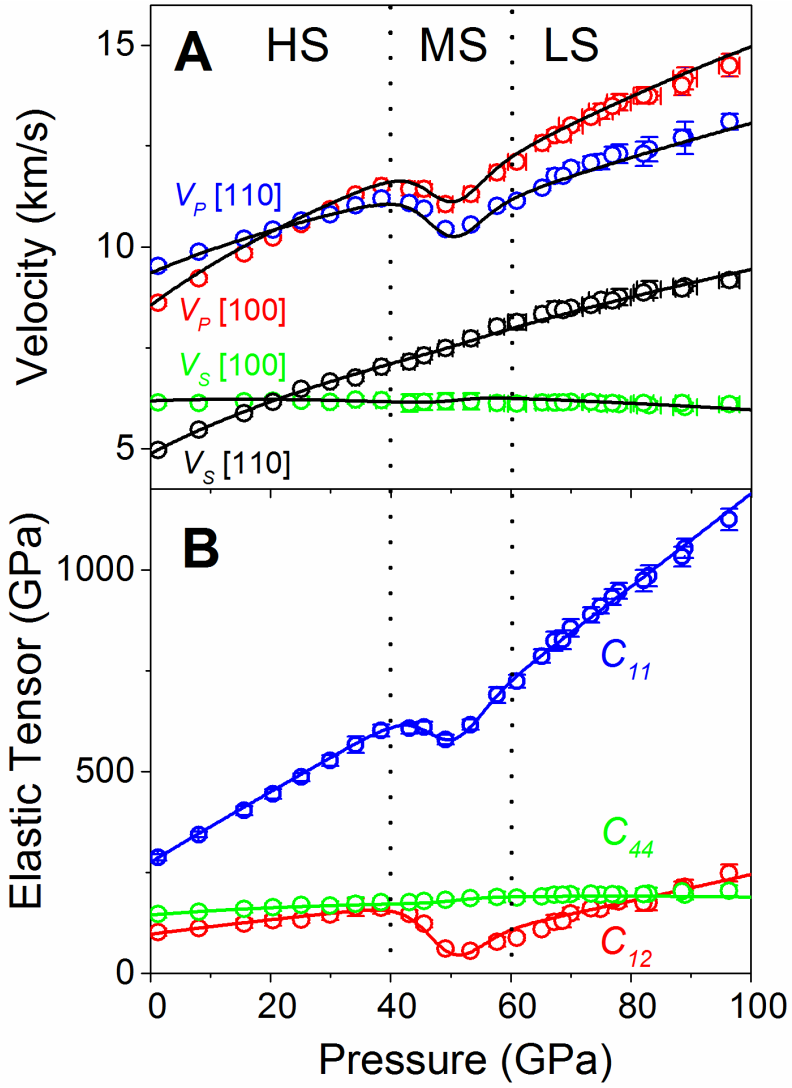


Figure 4.5: Elasticity of single-crystal ferropericlase ($Mg_{0.92}Fe_{0.08}$)O as a function of pressure at 300 K. (A) Compressional and shear wave velocities along the [100] and [110] crystallographic axes as a function of pressure. Compressional wave velocities were measured using the ISS technique, while shear wave velocities were measured using the BLS technique. Open circles: experimental data; solid lines: modelled velocity profiles using thermoelastic equations (see SI for details). (B) Elastic constants ($C_{ij}$) as a function of pressure. Open circles: $C_{ij}$ directly derived from measured compressional and shear wave velocities via Christoffel's equations; solid lines: modelled $C_{ij}$ profiles. Vertical dashed lines are plotted to guide the eyes for the high-spin (HS), mixed-spin (MS; HS+LS), and low-spin (LS) regions, respectively (see Figure. 4.3 for details).

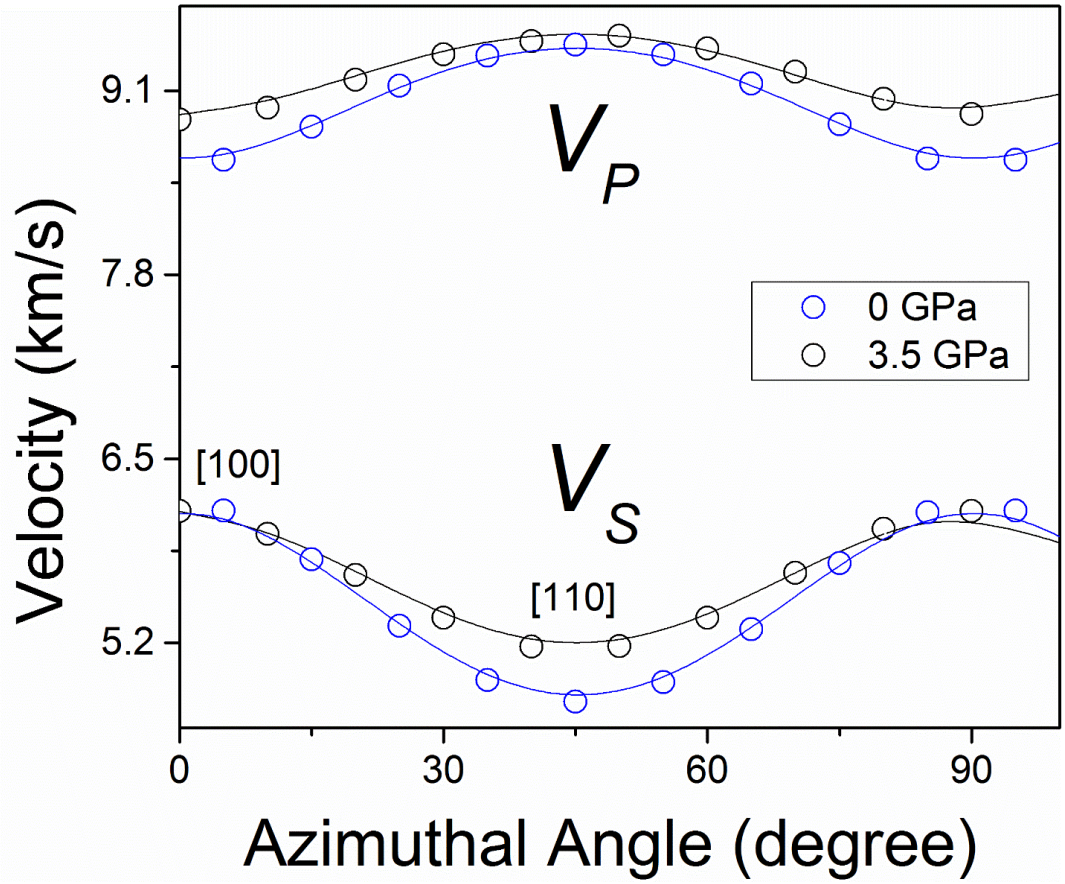


Figure 4.6: Compressional ($V_P$) and shear ($V_S$) wave velocities of ferropericlase in the (100) platelet as a function of azimuthal angle at ambient (blue circles) and 3.5 GPa (black circles). Uncertainties of the velocities are smaller than the size of the symbols and are not shown for clarity. Solid lines represent modelled velocity profiles from the best fit to the single-crystal elastic constants for each given pressure. These orientation-dependent measurements also help use to locate the [100] and [110] directions for the (100) platelet.

Examination of the directly-measured $V_P$ and $V_S$ show that the $V_P$ softens by ~10% maximum in both the [100] and [110] directions within the spin transition, while the $V_S$ along the [100] is slightly enhanced but the $Vs$ along the [110] is not noticeably affected (Figure 4.5 A) (see SI for comparison with previous results). Furthermore, the $C_{11}$ and $C_{12}$

elastic constants are significantly softened by a maximum of 16% and 70%, respectively, across the spin transition, but $C_{44}$ is not affected by the spin transition (Figure 4.5 B). The maximum softening for these parameters occurs at approximately 50 GPa, which is midway within the spin transition where the fraction of the LS state is about 50% (Figure 4.2). As reported in previous theoretical calculations [*Wu et al.*, 2013], the $C_{11}$ and $C_{12}$ softening can be explained by the addition of an energy abnormality as a result of the HS and LS mixing (shown in the last term in Equation [1]). Since $n(\sigma_4)$ is an even function and $\partial n/\partial \sigma_4|_{\sigma_4=0} = 0$, the last term in Equation [1] vanishes such that the $C_{44}$ softening is not expected to occur across the spin crossover [*Wu et al.*, 2013]. Our results thus confirm theoretical predictions on the elasticity across the spin transition in ferropericlase at high pressures. The derived elastic constants are used to calculate $V_{S1}$, $V_{S2}$, and $V_P$ velocities as a function of propagation directions ($\boldsymbol{n}$) by solving the Christoffel's equation $\det|C_{ijkl}n_jn_l - \rho V^2\delta_{ik}| = 0$ (Figure 4.8). At ambient conditions, the single-crystal ferropericlase exhibits the slowest $V_P$ in the [100] direction and the fastest $V_P$ in the [111] direction, while the $V_S$ is the slowest in the [110] direction and the fastest in the [100] direction. This anisotropic behavior is reversed at pressures of approximately 21 GPa, above which the $V_P$ minimum and maximum are along the [111] and [100], respectively, while the $V_S$ minimum and maximum are along the [100] and [110] directions. The velocities vary significantly with the propagation direction at pressures above approximately 40 GPa, indicating that the single-crystal ferropericlase exhibits strong $V_P$ and $V_S$ anisotropies. The velocity anisotropy factor ($A$) is defined as $A = (V_{max} - V_{min})/2(V_{max} + V_{min}) \times 100\%$, where $V_{max}$ and $V_{min}$ are the maximum and minimum velocities, respectively [*Mainprice et al.*, 2000]. For $V_P$, the anisotropy is defined as the difference between the maximum and minimum velocities in corresponding propagation directions, while the $V_S$ splitting anisotropy is defined as the velocity difference between the maximum and minimum velocities being two orthogonally

polarized $V_S$ velocities along corresponding propagation directions. Our results show that the $V_P$ anisotropy and the $V_S$ splitting anisotropy are 11.5% and 23.5% at ambient conditions, decreasing to almost zero at approximately 21 GPa, and then increasing monotonically up to 40 GPa, which are consistent with previous results [*Jackson et al*., 2006; *Crowhurst et al*., 2008]. Most importantly, the $V_P$ anisotropy increases to 11.2% at 50 GPa within the spin transition (13% increase in the anisotropy as compared to the extrapolated HS state reference), while the $V_S$ splitting anisotropy continuously increases with increasing pressure but deviates from the extrapolated HS state counterpart starting with the spin transition (Figure 4.7 C and Figure 4.9). Contrary to previous studies [*Marquardt et al.,* 2009b], our results show that the spin transition is actually associated with the enhanced $V_P$ anisotropy and slightly reduced $V_S$ anisotropy as compared to the extrapolated HS counterpart (Figure 4.9). But within the uncertainty, the spin transition effect on $V_S$ anisotropy is negligible (Figure 4.7 C). Furthermore, our results clearly show that the LS ferropericlase exhibits distinct elastic behavior from that of the HS state, including enhanced pressure derivative of $C_{11}$, $C_{12}$ and $C_{44}$, which implies enhanced pressure dependence of aggregate $K_S$ and aggregate $V_P$ (Figure 4.5, Figure 4.7 A and 4.7 B; Table 4.1). In particular, the spin transition is associated with a significant reduction of the aggregate $V_P/V_S$ ratio via the aggregate $V_P$ softening since *Vs* softening does not occur within the spin transition; this ratio is reduced from 1.75 at approximately 40 GPa at the onset of the transition to 1.6 at approximately 50 GPa which is midway within the transition (Figure 4.7 B and 4.7 D). The LS state also exhibits lower $V_P/V_S$ ratio (~ 12% reduction) than that of the extrapolated HS state. Such a reduction in the $V_P/V_S$ ratio highlights the abnormality for the Poisson's ratio within the spin transition and into the LS state.

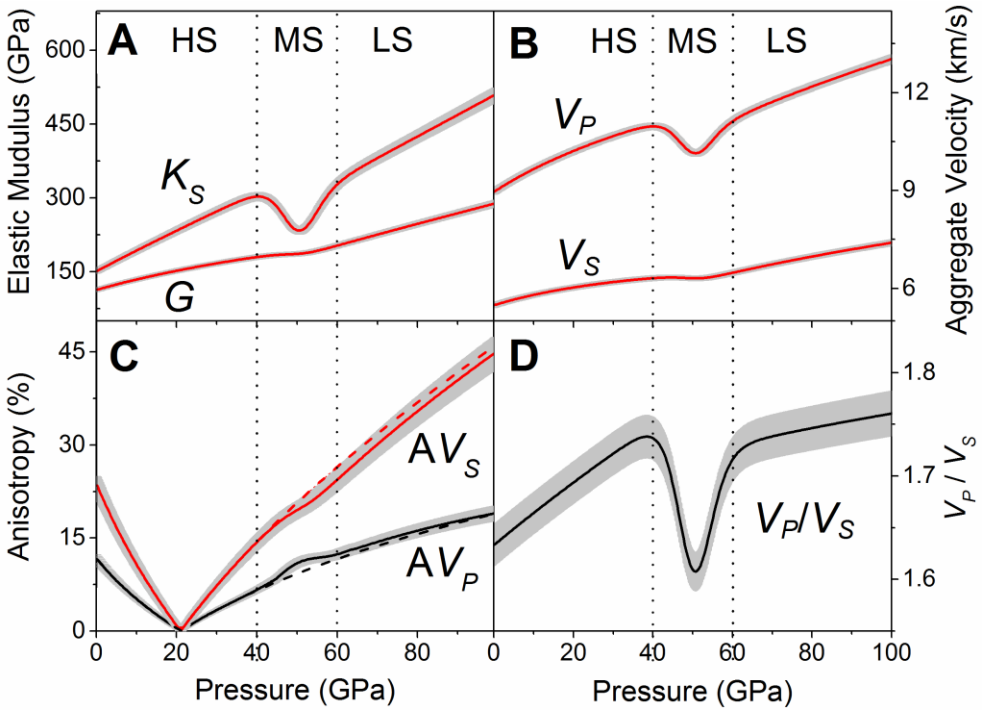


Figure 4.7: Aggregate bulk and shear moduli $K_S$ and $G$, aggregate velocities, elastic anisotropies and aggregate $V_P/V_S$ ratio of ferropericlase $(Mg_{0.92}Fe_{0.08})O$ at high pressure and 300 K. (A) Adiabatic bulk and shear modulus from Vogit-Reuss-Hill average; (B) Aggregate compressional $V_P$ and shear wave velocities $V_S$, where $V_P = \sqrt{K_S + 4/3G/\rho}$ and $V_S = \sqrt{G/\rho}$ ; (C) Compressional and shear wave anisotropy as a function of pressure; dashed lines are the extrapolated anisotropies for the HS state that are plotted for comparison; (D) aggregate $V_P/V_S$ ratio. Grey shaded areas represent uncertainties calculated from standard error propagations using the experimentally derived elastic constants. Vertical dashed lines are plotted to guide the eyes for the HS, MS, and LS regions, respectively.

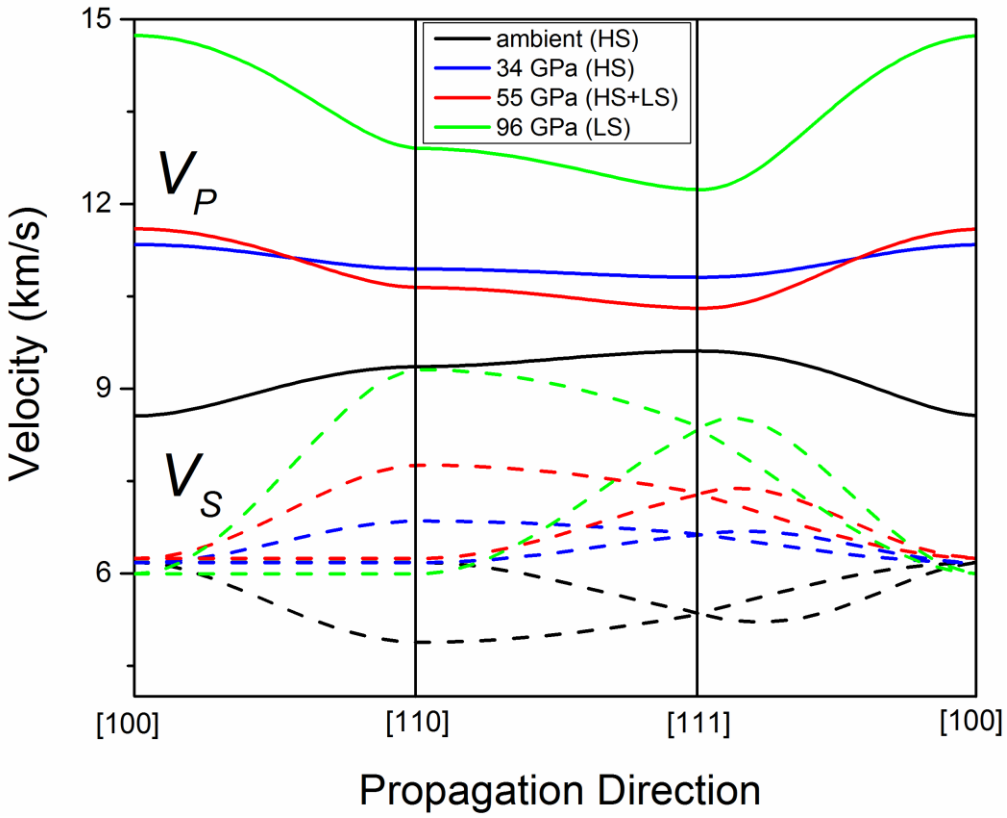


Figure 4.8: Compressional ($V_P$) and shear ($V_S$) wave velocities of the single-crystal ferropericlase ($Mg_{0.92}Fe_{0.08}$)O as a function of the propagation direction at high pressures. The velocities at representative pressures are plotted to highlight the changes in compressional and shear wave anisotropies across the spin transition.

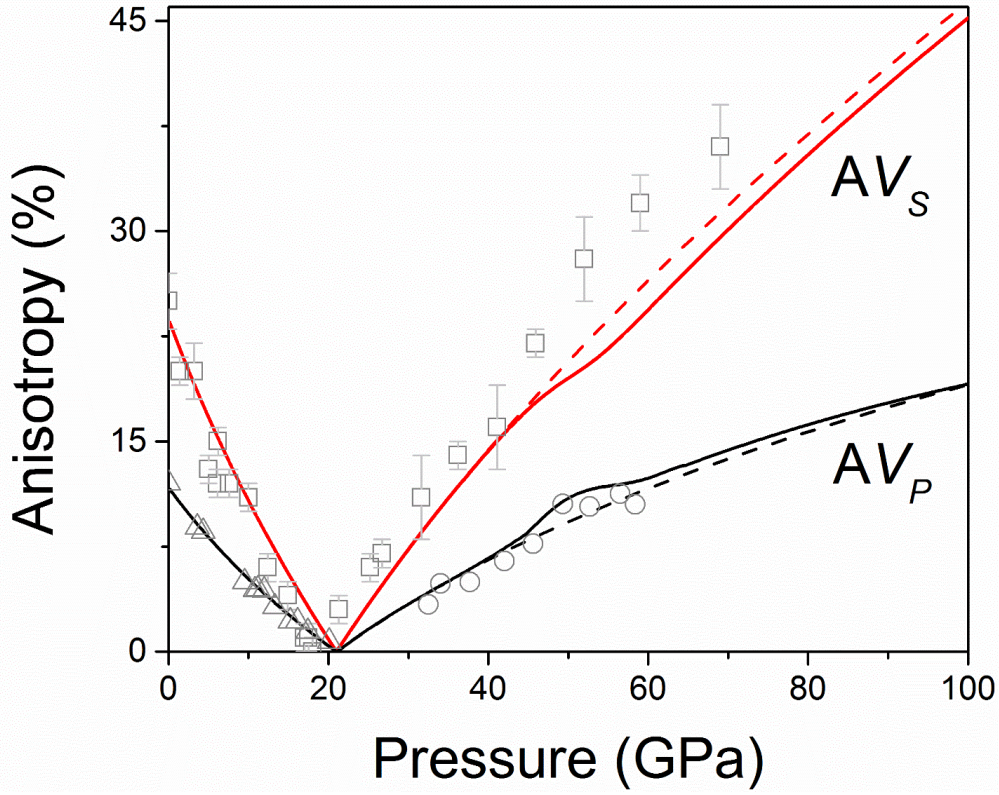


Figure 4.9: Compressional and shear wave anisotropy as a function of pressure at 300 K. Red lines: shear wave anisotropy; black lines: compressional wave anisotropy. Dashed lines are the extrapolated anisotropies for the HS state that are plotted for comparison. Open squares: shear wave anisotropy calculated from directly measured velocities along [100] and [110] using equation ($V_S$[100] − $V_S$ [110]) / ($V_S$ [100] + $V_S$ [110])/2 via BLS measurement [*Marquardt et al.*, 2009b]; open triangles: compressional wave anisotropy calculated from elastic constants measured by BLS using Christoffel's equations [*Jackson et al.*, 2006]; open circles: compressional wave anisotropy calculated from elastic constants measured by ISS using Christoffel's equations [*Crowhurst et al.*, 2008].

### 4.3.2 Implication for Lower-Mantle Seismic Heterogeneities

To understand the effects of the spin transition on the elasticity of ferropericlase at relevant *P-T* conditions of the lower mantle [*Lin et al.*, 2007b; *Tsuchiya et al.*, 2006], we have modelled the elastic constants of ferropericlase along an expected lower-mantle

geotherm using thermoelastic models and a previously reported spin crossover diagram [*Mao et al.*, 2011b; *Wu et al.*, 2013]. The thermal EoS parameters of ferropericlase with 25 at.% iron in a previous experimental report are linearly scaled back to construct the spin crossover diagram for our ferropericlase with 8 at.% iron at high *P-T* (See SI for details), showing that the spin crossover of ferropericlase with 8 at.% iron occurs between 65 and 105 GPa along the geotherm. The temperature derivatives of the elastic constants for pure MgO [*Karki et al.*, 1999] are combined with our high-pressure elasticity results (Table 4.1 and Table 4.2) to account for the high *P-T* effects for the HS and LS states, respectively (Figure 4.10). These modelled results show that the effects of the spin crossover on the elastic and seismic parameters along an expected adiabatic geotherm remain profound, even though the spin crossover is broadened by high temperatures (Figure 4.11 and Figure 4.10). In particular, the $C_{11}$ and $C_{12}$ elastic constants exhibit 15% and 60% maximum reduction, respectively, within the spin crossover at approximately 85 GPa, corresponding to 1900 km in depth. The $V_P$ anisotropy increases to 18.6% at ~85 GPa within the spin transition (a 23% increase in the anisotropy as compared to the extrapolated HS state reference), while the pressure-dependent $V_S$ anisotropy is lower than that of the HS counterpart in the LS state (Figure 4.10 B). Compared to the HS state reference, the aggregate $V_P$ decreases by 10% while the $V_P/V_S$ ratio drops by 13% within the spin crossover (Figure 4.11). On the other hand, the aggregate $V_P$ and $V_S$ profiles of the LS ferropericlase are significantly higher than that of its HS state counterpart (Figure 4.11 A). Using the HS state as the reference, we have calculated the deviations of a number of seismic parameters across the spin crossover along an expected mantle geotherm. These results show that the spin crossover produces significant variations in the $V_P$ and $V_S$ velocities and anisotropies, $V_P/V_S$ ratio, and Poisson's ratio as compared to the extrapolated HS state. Specifically, the $V_P$, $V_P/V_S$ ratio, and Poisson's ratio are significantly reduced

within the spin crossover, whereas the LS state exhibits enhanced $V_P$ and $V_S$ velocities as well as reduced $V_P/Vs$ and Poisson's ratio (Figure 4.12).

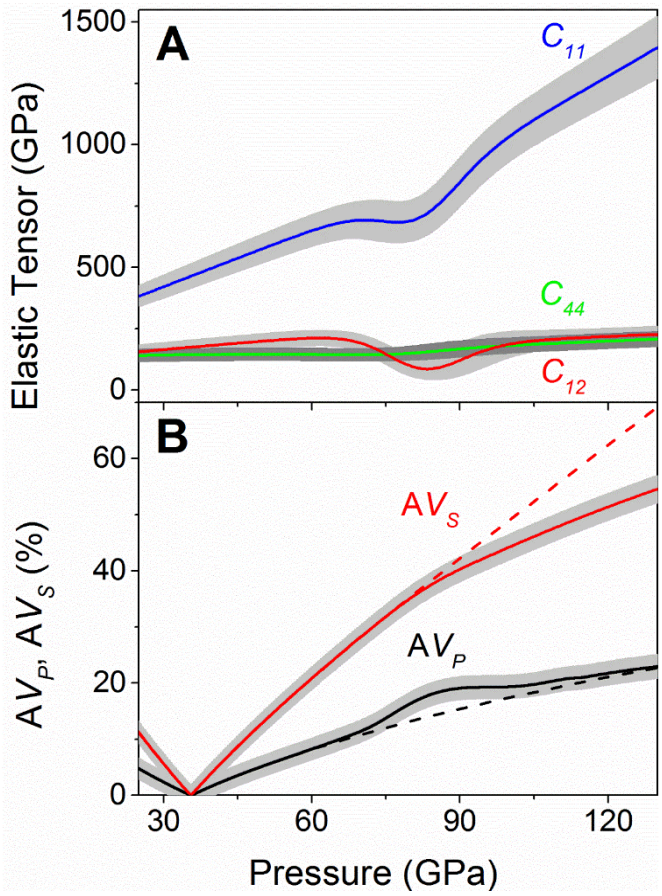


Figure 4.10: Modelled elastic properties of ferropericlase ($Mg_{0.92}Fe_{0.08}$)O across the spin transition zone along an expected lower-mantle geotherm. (A) Elastic constants: $C_{11}$, $C_{12}$, and $C_{44}$ plotted as blue, red, and green lines, respectively. (B) $V_P$ and $V_S$ anisotropy. Red line: $V_S$ anisotropy; black line: $V_P$ anisotropy. The $V_P$ and $V_S$ anisotropies are calculated using the equations $AV_P = (V_P max - V_P min)/2(V_P max + V_P min)$ and $AV_S = (V_S max - V_S min)/2(V_S max + V_S min)$, where subscripted *min* and *max* represent the minimum and maximum velocity of the single crystal, respectively. Grey shaded areas show the uncertainties calculated using standard error propagations.

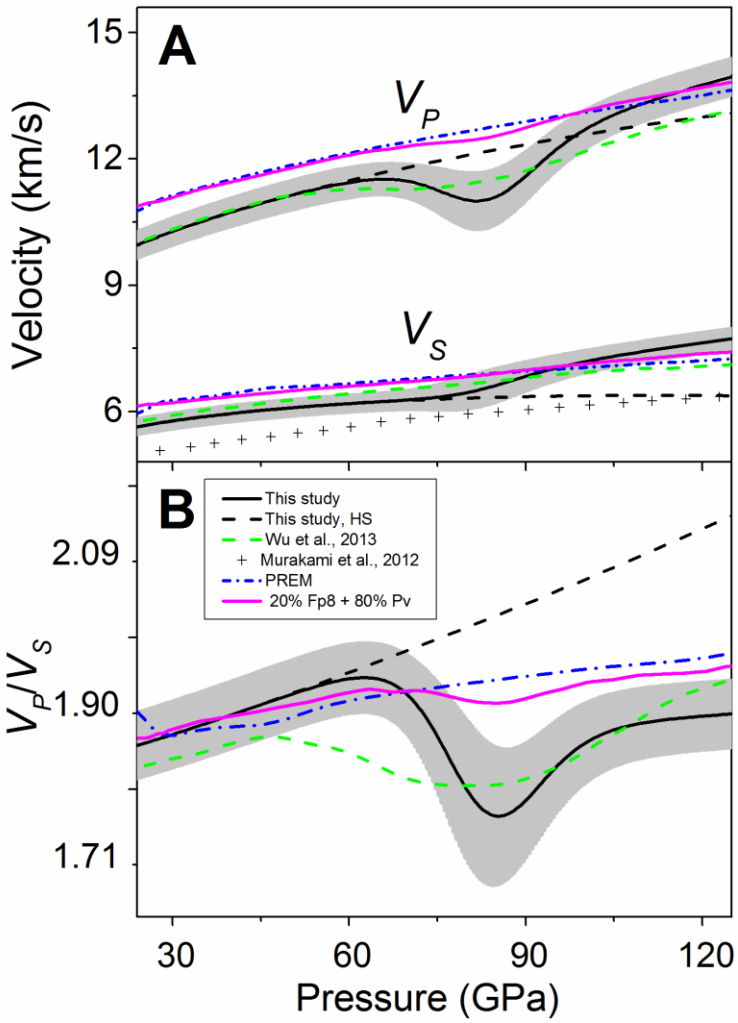


Figure 4.11: Modelled seismic velocities and $V_P/V_S$ ratio of ferropericlase ($(Mg_{0.92}Fe_{0.08})O$) along an expected lower-mantle geotherm. (A) Aggregate compressional and shear wave velocities. These results are calculated from the single-crystal elastic constants. (B) Calculated $V_P/V_S$ ratio. Solid lines: modelled seismic parameters with uncertainties shown as grey areas; black dashed lines: modelled parameters for the high-spin state; green dotted lines: theoretical $V_P$ and $V_S$ values of ferropericlase ($(Mg_{0.875}Fe_{0.125})O$) [*Wu et al.*, 2013]; crosses: experimental results with 17% iron [*Murakami et al.*, 2012]. PREM seismic parameters are plotted as blue dotted dashed lines for comparison [*Dziewonski and Anderson*, 1981]; The magenta lines are the modelled velocity profiles assuming that the lower mantle is composed of 20% ferropericlase (fp8) and 80% Bridgmanite (Pv) [*Murakami et al.*, 2012].

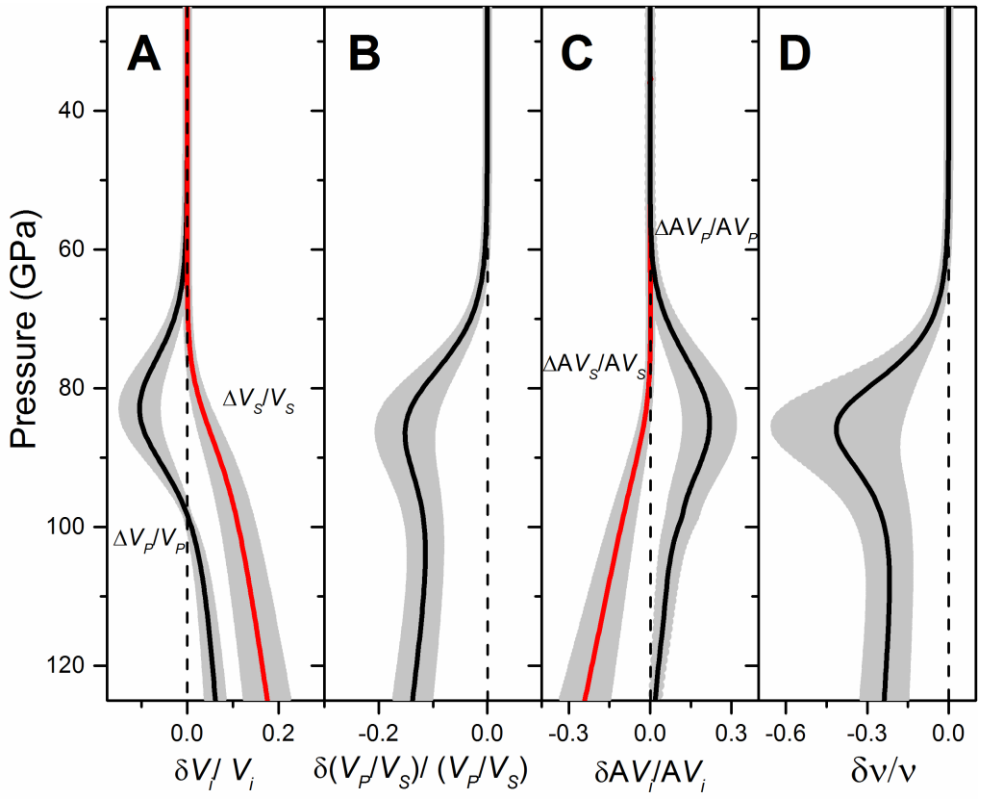


Figure 4.12: Variations of the seismic parameters of ferropericlase $(Mg_{0.92}Fe_{0.08})O$ as a function of depth along an expected lower-mantle geotherm. The variations were derived using the modelled seismic parameters of the high-spin ferropericlase as the reference. (A) Aggregate $V_P$ and $V_S$; (B) $V_P/V_S$ ratio; (C) $V_P$ and $V_S$ anisotropy; (D) Poisson's ratio.

Our modelled velocity profiles show that the $V_P$ profile of ferropericlase with 8 at.% iron is significantly reduced by a maximum of 10% with the spin crossover at approximately 1900 km in depth along an expected mantle geotherm, while the $V_S$ profile is slightly enhanced with increasing fraction of the LS state as compared to the extrapolated HS state (Figure 4.11). That is, the $V_P/Vs$ ratio is also significantly reduced with the spin crossover. On the other hand, the $V_P$ and $Vs$ profiles of the LS ferropericlase are higher than those of the extrapolated HS state as well as the PREM model toward the very bottom of the lower mantle. Considering that ferropericlase in the lower mantle may account for

approximately 20 vol.% of the lower-mantle in a pyrolite model [*Ringwood*, 1975], our calculated $V_P$ and *Vs* profiles with 20 vol.% of ferropericlase and 80 vol.% of bridgmanite are fairly consistent with seismic PREM model at depths from uppermost to mid lower-mantle. On the other hand, the spin crossover in ferropericlase is expected to contribute to a 3% reduction in $V_P$ and a 5% reduction in $V_P/V_S$ ratio at the middle parts of the lower mantle, while the occurrence of the LS ferropericlase would result in enhanced $V_P$ and $V_S$ profiles relative to the seismic model (Figure 4.11). These changes are expected to be more significant for ferropericlase containing 20% iron in a pyrolite model [*Ringwood*, 1982]. Since the $V_P$ and *Vs* velocities of ferropericlase behave differently across the spin transition, our results here also indicate $V_P/V_S$ ratio can be used as a more sensitive seismic indicator for probing the spin transition-induced heterogeneities in the lower mantle (Figures 4.7 and 4.11).

Based on the $V_S$ profiles of the polycrystalline ferropericlase and bridgmanite at high *P-T* conditions, it has been proposed that the lower mantle is predominantly made of bridgmanite by 93% in volume, called the perovskitic lower mantle, and that ferropericlase may only account for 7% of the lower-mantle mineralogy [*Murakami et al.*, 2012]. In this scenario, the contributions of the elastic and seismic anomalies of ferropericlase across the spin crossover would play a much smaller role to the overall seismic profiles of the lower mantle such that the associated effects may become seismically insignificant. In our modelling, we have considered the lower-mantle *P-T* conditions along an expected adiabatic geotherm, but the possibility of having a super-adiabatic lower mantle with a steeper thermal gradient than the adiabatic geotherm model could also be considered here [*Murakami et al.*, 2012]. The relatively higher geotherm would widen the spin crossover leading to lesser velocity anomalies within the spin crossover and lower $V_P$ and $V_S$ profiles

of the LS ferropericlase in the lower mantle. It also remains to be seen as to how the changes in the partitioning coefficient of iron between bridgmanite and ferropericlase ($K_D^{Pv\text{-}Fp} = (X_{Fe}^{Pv}/ X_{Mg}^{Pv}) / (X_{Fe}^{Fp}/ X_{Mg}^{Fp})$) across the spin transition can influence the abnormal elasticity in ferropericlase reported here. Previous studies have shown that the $K_D^{Pv\text{-}Fp}$ decreases from approximately 0.85 at ~750-km depth to 0.2 at ~1800 km depth in a pyrolitic composition, indicating that $Fe^{2+}$ preferentially partitions into ferropericlase in the middle to lower part of the lower-mantle [*Auzende et al.*, 2008; *Sakai et al.*, 2009]. That is, the iron content of lower mantle minerals can be largely influenced by the depth and breadth of spin transition. In this case, the spin crossover of ferropericlase can even occur over a wider range of *P*-*T* conditions with variable amounts of iron involved, thus spreading seismic and chemical anomalies in ferropericlase that may become too broad to be seismically detectable with our current seismic resolutions. Our results here point to potential seismic heterogeneities in the lower mantle and also highlight a much more complex picture on the elasticity of ferropericlase lower mantle, which can have profound consequences in our understanding of chemical composition, seismology and geodynamics of the region.

Table 4.2: Experimental results for ferropericlase ($Mg_{0.92}Fe_{0.08}$)O. $V_P$ velocities were derived from ISS measurements while $V_S$ velocities were from BLS measurements.

| **Run 1** | | | | | | | | |
|---|---|---|---|---|---|---|---|---|
| Pressure | Density g/cm$^3$ | $V_P$ [100] km/s | $V_P$ [110] km/s | $V_S$ [100] km/s | $V_S$ [110] km/s | $C_{11}$ GPa | $C_{12}$ GPa | $C_{44}$ GPa |
| 1.3(0.1) | 3.80 | 8.61(0.08) | 9.52(0.09) | 6.14(0.07) | 4.97(0.06) | 287(8) | 102(9) | 146(8) |
| 8.0(0.1) | 3.95 | 9.21(0.08) | 9.87(0.09) | 6.12(0.07) | 5.46(0.07) | 343(8) | 112(7) | 152(6) |
| 15.6(0.2) | 4.11 | 9.83(0.10) | 10.19(0.09) | 6.17(0.07) | 5.87(0.07) | 403(11) | 123(11) | 159(9) |
| 20.4(0.0) | 4.20 | 10.23(0.07) | 10.42(0.06) | 6.19(0.10) | 6.15(0.06) | 445(12) | 131(12) | 163(10) |
| 25.2(0.3) | 4.28 | 10.56(0.07) | 10.64(0.07) | 6.19(0.10) | 6.47(0.07) | 486(10) | 132(8) | 168(7) |
| 29.9(0.5) | 4.36 | 10.93(0.06) | 10.81(0.07) | 6.15(0.10) | 6.65(0.07) | 527(14) | 144(13) | 168(10) |
| 34.2(0.6) | 4.43 | 11.29(0.07) | 11.02(0.07) | 6.21(0.10) | 6.75(0.09) | 566(20) | 164(22) | 172(16) |
| 38.5(0.8) | 4.49 | 11.50(0.09) | 11.19(0.09) | 6.19(0.10) | 7.03(0.10) | 601(15) | 161(14) | 176(10) |
| 43.1(0.9) | 4.56 | 11.43(0.15) | 11.08(0.07) | 6.12(0.22) | 7.15(0.10) | 607(13) | 146(10) | 176(8) |
| 45.6(1.0) | 4.60 | 11.43(0.12) | 10.94(0.07) | 6.15(0.20) | 7.31(0.10) | 610(14) | 122(9) | 178(9) |
| 49.2(1.2) | 4.67 | 11.05(0.08) | 10.44(0.07) | 6.16(0.20) | 7.49(0.11) | 579(12) | 61(4) | 182(8) |
| 53.3(1.1) | 4.28 | 11.30(0.07) | 10.55(0.06) | 6.17(0.20) | 7.72(0.11) | 616(12) | 55(3) | 176(8) |
| 57.7(1.2) | 4.81 | 11.84(0.10) | 11.01(0.08) | 6.13(0.10) | 8.02(0.11) | 689(19) | 78(12) | 188(14) |
| 61.0(1.5) | 4.86 | 12.11(0.08) | 11.14(0.06) | 6.12(0.15) | 8.13(0.18) | 724(16) | 88(7) | 188(9) |
| 65.2(1.0) | 4.91 | 12.57(0.08) | 11.46(0.07) | 6.14(0.15) | 8.33(0.11) | 786(17) | 109(8) | 190(9) |
| 67.3(0.4) | 4.94 | 12.77(0.13) | 11.76(0.17) | 6.14(0.11) | 8.45(0.20) | 823(24) | 127(18) | 195(16) |
| 70.0(2.0) | 4.97 | 13.00(0.12) | 11.95(0.14) | 6.16(0.11) | 8.49(0.10) | 856(22) | 148(15) | 196(13) |
| 75.0(2.0) | 5.03 | 13.36(0.19) | 12.10(0.19) | 6.11(0.11) | 8.67(0.10) | 909(18) | 159(10) | 194(8) |
| 78.0(2.0) | 5.06 | 13.58(0.20) | 12.30(0.23) | 6.10(0.11) | 8.75(0.21) | 947(20) | 177(11) | 195(9) |
| 83.0(2.0) | 5.12 | 13.74(0.10) | 12.41(0.30) | 6.06(0.11) | 8.94(0.21) | 985(26) | 174(18) | 197(14) |
| 89.0(2.0) | 5.19 | 14.17(0.28) | 12.69(0.40) | 6.03(0.11) | 9.02(0.11) | 1053(24) | 215(17) | 194(11) |
| **Run 2** | | | | | | | | |
| 68.7(1.3) | 4.95 | 12.78(0.13) | 11.76(0.07) | 6.13(0.10) | 8.43(0.10) | 826(23) | 130(17) | 195(15) |
| 73.3(1.5) | 5.01 | 13.21(0.10) | 12.07(0.17) | 6.16(0.10) | 8.56(0.14) | 888(19) | 160(12) | 197(10) |
| 76.9(1.1) | 5.05 | 13.49(0.10) | 12.28(0.20) | 6.12(0.10) | 8.67(0.15) | 932(19) | 179(12) | 196(9) |
| 82.1(1.6) | 5.11 | 13.75(0.21) | 12.30(0.30) | 6.13(0.10) | 8.86(0.10) | 973(27) | 174(20) | 195(15) |
| 88.5(1.1) | 5.18 | 14.00(0.25) | 12.70(0.20) | 6.13(0.10) | 8.96(0.10) | 1033(25) | 208(19) | 203(13) |
| 96.4(1.7) | 5.27 | 14.50(0.28) | 13.10(0.20) | 6.10(0.15) | 9.17(0.16) | 1125(27) | 248(21) | 205(13) |

**Acknowledgements**

We greatly appreciate the critical comments and helpful suggestions by S.P. Grand and Z. Mao. We acknowledge J. Liu, Y. Wu, M. Song, C. Prescher, K. Zhuravlev, and V. Prapapenka for their assistance in the high-pressure experiments. J.F. Lin acknowledges support from the Geophysics Program (EAR-1446946) of the U.S. National Science Foundation. The ISS system at UT Austin is funded by the Instrumentation and Facility Program (EAR-1053446) of the US NSF and the Instrumentation Matching Program of the Jackson School of Geosciences, while the Brillouin system was built partially using funds from the CDAC (Carnegie-DOE Alliance Center) and the Jackson School Matching Program. Synchrotron X-ray diffraction work was performed at the GSECARS of the APS, ANL. APS is supported by 263 DOE-BES, under Contract No. DE-AC02-06CH11357. GeoSoilEnviroCARS is supported by the National Science Foundation - Earth Sciences and Department of Energy Geosciences. This work was partly supported from ISEI for long term Joint-Use Research.

# Chapter 5: Coupled Effect of Fe and Al Substitutions on the Single-Crystal Elasticity of Bridgmanite in the Earth's Lower Mantle[3]

Single-crystal elasticity of bridgmanite with chemical compositions of $Mg_{0.95}Fe_{0.06}Al_{0.04}Si_{0.96}O_3$ (Fe6-Al4-Bgm) and $Mg_{0.90}Fe_{0.12}Al_{0.11}Si_{0.90}O_3$ (Fe12-Al11-Bgm) has been investigated using combined Brillouin Light Scattering (BLS), Impulsive Stimulated Light Scattering (ISS), and X-ray diffraction in diamond anvil cells at 25 GPa and 35 GPa. Based on experimentally measured $V_P$ and $V_S$ as a function of the azimuthal angle within two crystal platelets for each composition, we have reliably derived full elastic constants and elastic moduli of these Fe-Al-bearing bridgmanite crystals at high pressures. Our results show that the elastic constants can be significantly affected by coupled Fe and Al substitution when compared with end-member $MgSiO_3$ bridgmanite, resulting in a dramatic $V_S$ decrease of ~4-5% as well as a slight increase of $V_\Phi$. The $V_S$ splitting anisotropy of Fe12-Al11-Bgm is ~26%, which is ~16% higher than that of Fe6-Al4-Bgm. The existence of Fe-Al-rich bridgmanite may contribute to the reduced $V_S$ and increased seismic $V_S$ splitting anisotropy in some regions of the Earth's lower mantle.

## 5.1 INTRODUCTION

Seismic tomography studies provide growing evidence for seismic heterogeneities in middle and lower parts of lower mantle. These observations have been traditionally interpreted as thermal and/or chemical perturbations, e.g., hotter/colder-than-average temperatures and Fe enrichment [*Garnero and McNamara*, 2008; *van der Hilst and*

[3]This chapter is based on the article: Yang, J., Fu, S., Okuchi, T., Lin, J. F., Coupled Effect of Fe and Al Substitutions on the Single-Crystal Elasticity of Bridgmanite in Earth's Lower Mantle. (manuscript in preparation)
Author Contributions:
Lin, J.F and Yang, J. designed the research. Lin, J.F. and Okuchi, T. synthesized the Fe-Al-bearing bridgmanite single crystals. Yang, J. and Fu, S. collected the BLS and ISS data. Lin, J.F. Yang, J. and Fu. S. discussed the content of the manuscript. Yang, J. and Lin, J.F wrote the paper. All authors commented on the manuscript.

*Kárason*, 1999]. The observation of the Large Low Shear Velocity Provinces (LLSVPs) with the lower-than-average shear wave velocity ($V_S$) beneath Africa and the Central Pacific points to a number of possible origins for the regions: higher-than-average temperature, Fe enrichment, and/or existence of primordial materials [*Burke et al.*, 2008; *Fukui et al.*, 2016; *Lee et al.*, 2010; *Mao et al.*, 2011a]. However, the anti-correlations between bulk sound velocity ($V_\Phi$) and $V_S$ in LLSVPs cannot be simply explained by temperature variations alone [*Garnero et al.*, 2016; *Karato and Karki*, 2001]. Chemical variations caused by Fe and/or Al enrichment as well as the electronic spin transition of Fe in major lower-mantle host minerals bridgmanite (Bgm) and ferropericlase (Fp) have been invoked to explain the seismic anomalies in the middle and lowermost lower mantle [*Fukui et al.*, 2016; *Huang et al.*, 2015; *Jackson et al.*, 2005; *Wu and Wentzcovitch*, 2014; *Yang et al.*, 2016]. Elasticity as well as texturing of the constitute minerals of the Earth's lower mantle at relevant pressure-temperature (P-T) conditions are thus critically needed to provide mineral physics constraints on these seismic observations.

Based on a pyrolite model, Earth's lower mantle likely consists of ~75% Fe-Al-bearing Bgm, 20% Fp and 5% calcium silicate perovskite [*Irifune et al.*, 2010; *Ringwood*, 1975]. The elasticity and textures of the most abundant lower-mantle mineral, Fe-Al-bearing Bgm, can thus play a critical role in deciphering seismic tomography and chemical composition of the deep mantle. Among the three major minerals of the lower-mantle, previous studies have shown that Bgm is the only phase that can accommodate a significant amount of Al, together with the dissolution of a significant amount of $Fe^{3+}$ in its lattice [*Hummer and Fei*, 2012; *Irifune et al.*, 2010]. In a lower-mantle pyrolitic composition, it has been shown that Al enters into the B-site of the Bgm lattice to replace $Si^{4+}$ via charge-coupled substitution, with high-spin $Fe^{3+}$ replacing A-site $Mg^{2+}$: $Mg^{2+} + Si^{4+} \leftrightarrow Fe^{3+} + Al^{3+}$. The coupled substitution of $Fe^{3+}$ and $Al^{3+}$ and self-disproportionation reaction

significantly enhances the $Fe^{3+}$ content of Bgm and potentially produces metallic Fe in the lower mantle [*Frost et al.*, 2004; *Xu et al.*, 2017]. $Fe^{3+}$ and $Al^{3+}$ can also affect the Fe partitioning between Bgm and Fp. Together with the consideration of the spin transition of Fe in Bgm and Fp, recent studies have showed that the Fe partitioning coefficient $K_D^{Bgm\text{-}Fp}$, given by $([Fe^{2+}+Fe^{3+}]^{Bgm}/[Mg^{2+}]^{Bgm})/([Fe^{2+}]^{Fp}/[Mg^{2+}]^{Fp})$, increases from ~0.5 at 23 GPa (topmost lower-mantle conditions) to almost 0.9 at approximately 28 GPa (~750 km depth) due to the coupled substitution, but it decreases to ~0.5 at approximately 40-50 GPa in the pyrolitic composition due to the spin transition of Fe in Fp for mid-lower mantle conditions [*Irifune et al.*, 2010; *Xu et al.*, 2017]. That is, the Al solubility in Bgm increases with increasing pressure from 23 GPa to approximately 28 GPa. At approximately 30-40 GPa, the cation numbers of Fe and Al (oxygen = 3) are ~0.11 and ~0.10, respectively, in the Bgm lattice [*Irifune et al.*, 2010]. On the other hand, mid-ocean ridge basalt (MORB) in subducted slabs can contain higher amounts of Al than the pyrolitic composition; if subducted into the lower mantle, they can produce Al-rich phases including Bgm, NAL ($NaAlSiO_4$), and CF ($CaFe_2O_4$) [*Hirose et al.*, 1999; *Hirose et al.*, 2005]. Physical insight into the coupled effects of Fe and Al substitution on the elasticity of Bgm at high P-T conditions is thus critically needed for understanding seismic features of the lower mantle.

Sound velocity and elastic moduli of single-crystal and polycrystalline Bgm have been investigated at ambient conditions and high P-T conditions both theoretically and experimentally [*Chantel et al.*, 2012; *Jackson et al.*, 2005; *Li and Zhang*, 2005; *Li et al.*, 2005; *Murakami et al.*, 2012; *Murakami et al.*, 2007; *Tsuchiya and Tsuchiya*, 2006; *Wentzcovitch et al.*, 2004; *Wentzcovitch et al.*, 1998]. Extensive theoretical studies on the single-crystal elasticity of Fe-Al-bearing Bgm at relevant P-T conditions of the lower mantle have shown that the Bgm crystal can exhibit extremely high $V_P$ and $V_S$ splitting anisotropies and the substitution of Fe and Al reduces the $V_S$ by ~2-3% and $V_P$ by ~1.5%

at core-mantle-boundary conditions [*Li et al.*, 2005]. An experimental Brillouin light scattering (BLS) study on $V_S$ and equation of state of polycrystalline Bgm and Fp at relevant lower-mantle P-T conditions using the best fit to global seismic velocity profiles have indicated that the lower mantle is mostly made of Bgm [*Murakami et al.*, 2012]. On the other hand, experimental studies on the single-crystal elasticity of Bgm are rather limited to ambient conditions and high pressure, mostly due to technical difficulties and availability of high quality single crystals [*Fukui et al.*, 2016; *Kurnosov et al.*, 2017; *Sinogeikin and Bass*, 2000; *Yeganeh-Haeri*, 1994]. Single-crystal elastic constants of $MgSiO_3$ Bgm and Fe-Al-bearing Bgm at ambient conditions measured by inelastic X-ray scattering has been used to explain the anti-correlation between decreased $V_S$ and enhanced $V_\Phi$ in LLSVPs due to the Fe and Al cation-substitution [*Fukui et al.*, 2016]. Single-crystal elasticity of Fe-Al-bearing Bgm $(Mg_{0.9}Fe_{0.1}Si_{0.9}Al_{0.1})O_3$ with $Fe^{3+}/Fe^{2+} = 0.66$ up to 40 GPa at room temperature by BLS suggests that the aggregate $V_P$ and $V_S$ profiles of the pyrolitic Bgm with a high $Fe^{3+}/Fe^{2+}$ ratio co-existing with Fp are consistent with the PREM seismic profiles at depths of 670-1200 km [*Kurnosov et al.*, 2017]. However, these seismic profiles start to deviate from each other at depths greater than 1200 km, indicating that changes in Fe and Al substitution or $Fe^{3+}$ content may occur in the deeper regions of the lower mantle [*Kurnosov et al.*, 2017]. Comparison of these single-crystal elasticity results with theoretical calculations also reveals significant differences between the elasticity of Al-Fe-bearing and $MgSiO_3$ Bgm at lower-mantle pressures [*Karki et al.*, 1997; *Kurnosov et al.*, 2017; *Li et al.*, 2005; *Wentzcovitch et al.*, 2004]. Reliable single-crystal elasticity of Bgm as a function of Fe and Al substitution and $Fe^{3+}$ at lower-mantle P-T conditions remain experimentally unavailable to address these critical issues of our understanding of the lower-mantle seismic profiles and mineral physics.

Here we have studied the single-crystal elasticity of Fe-Al-bearing Bgm in two distinct compositions, $Mg_{0.95}Fe_{0.06}Al_{0.04}Si_{0.96}O_3$ (Fe6-Al4-Bgm) and $Mg_{0.90}Fe_{0.12}Al_{0.11}Si_{0.90}O_3$ (Fe12-Al11-Bgm), at 25 GPa and 35 GPa using combined BLS, Impulsive stimulated light scattering (ISS), and X-ray diffraction (XRD) in a diamond anvil cell (DAC). The use of ISS allows us to reliably measure $V_P$ of two crystal platelets of Bgm, whereas the BLS is used primarily to probe their $V_S$ at high pressures. Together with complimentary XRD results for derivation of the density and Mössbauer measurements to determine the $Fe^{3+}/Fe^{2+}$ ratio, we have successfully derived the full elastic constants of these Bgm crystals to evaluate coupled Fe-Al substitution effects on Bgm elasticity at high pressures. These results are compared with previous theoretical and experimental studies as well as seismic profiles to provide better mineral physics constraints on our understanding of the lower mantle.

## 5.2 EXPERIMENTS

Two batches of bridgmanite single crystals with different Fe and Al contents were synthesized using 5000-ton Kawai-type multi-anvil apparatus at Okayama University at Misasa, Japan [*Mao et al.*, 2017; *Okuchi et al.*, 2015]. Mixtures of powder starting materials including $MgSiO_3$, $Mg(OH)_2$, $Al_2O_3$, and $^{57}FeO$ with desired wt.% proportion for each batch were packed into a Pt capsule and compressed to 24 GPa. The sample assemblage was then heated to 1750 ºC for Run #5K2179 and to 1800 ºC for Run #5K2417 for approximately 7 hours to permit sufficient growth of the crystals. Some bridgmanite crystals were retrieved from the recovered capsules and then analyzed using a JEOL JXA-8200 electron microprobe in the Department of Geological Sciences, the University of Texas at Austin. The analyses confirmed the chemical homogeneity across each crystal examined with a composition of $Mg_{0.95}Fe_{0.06}Al_{0.04}Si_{0.96}O_3$ (Fe6-Al4-Bgm) from Run

#5K2417 and $Mg_{0.89}Fe_{0.12}Al_{0.11}Si_{0.89}O_3$ (Fe12-Al11-Bgm) from Run #5K2179, respectively. These crystals were also analyzed using conventional and synchrotron Mössbauer spectroscopy at ambient conditions and high pressures to determine the valence states of Fe in the samples [*Lin et al.*, 2016; *Mao et al.*, 2017]. Analysis of the Mössbauer spectra for hyperfine quadrupole splitting and isomer shifts indicates that Fe6-Al4-Bgm contains both $Fe^{3+}$ (55%) and $Fe^{2+}$ (45%) in the A site, while Fe12-Al11-Bgm contains 80% $Fe^{3+}$ and 20% $Fe^{2+}$ in the A site; no B site $Fe^{3+}$ was detected in the measurements. Combining both electron microprobe and Mössbauer analysis results, the detailed chemical formula for Fe6-Al4-Bgm and Fe12-Al11-Bgm can be written on the basis of three oxygen atoms as $Mg_{0.9589}Fe^{2+}_{0.033}Fe^{3+}_{0.027}Al_{0.04}Si_{0.96}O_3$ and $Mg_{0.89}Fe^{2+}_{0.024}Fe^{3+}_{0.096}Al_{0.11}Si_{0.89}O_3$, respectively [*Mao et al.*, 2017]. To confirm the single-crystal quality, lattice parameters, and orientations of the crystal structure, single-crystal XRD analysis with a wavelength of 0.3344 Å for the incident X-ray source was also performed at 13BMD and 13IDD beamline of GeoSoilEnviroCARS (GSECARS) of the Advanced Photon Source (APS), Argonne National Laboratory (ANL). The refined unit cell parameters in the *Pbnm* structure for Fe6-Al4-Bgm are a = 4.7657(3) Å, b = 4.9340(2) Å, c = 6.9032(6) Å and a = 4.7867(2) Å, b = 4.9569(2) Å, c = 6.9141(4) Å for Fe12-Al11-Bgm. Integrated peaks of the diffracted spots show an averaged full-width at half maximum (FWHW) of ~0.04º, indicating that the synthesized crystals are of high single crystal quality.

Multiple single-crystal bridgmanite samples in both compositions were polished to platelets ~15 μm in thickness for the high-pressure experiments. The crystallographic orientations of the platelets were determined using single-crystal XRD measurements at GSECARS, APS. Because a large number of velocity measurements from multiple platelets are required to reliably determine the elastic constants of the orthorhombic Bgm with acceptable uncertainties, having crystal platelets with appropriate orientations for the

velocity measurements is critical to extract reliable elastic constants, especially for Bgm, which has nine elastic constants [*Mao et al.*, 2015]. Thus, the sensitivities of each elastic constant to the specific orientation of the platelet were calculated and used as criteria to select the crystal platelets which can provide the best velocity constraints on full elastic constants (Figure 5.1 and Figure 5.2). The single crystal platelets with orientations (4.5, 0.9, 1.9) and (2.0, 4.2, -2.1) for Fe6-Al4-Bgm, and (6.1, -0.4, 1.4) and (0.1, -3.2, 3.6) for Fe12-Al11-Bgm were selected for high-pressure Brillouin and Impulsive experiments (Figure 5.2a and d inserts; Figure 5.1).

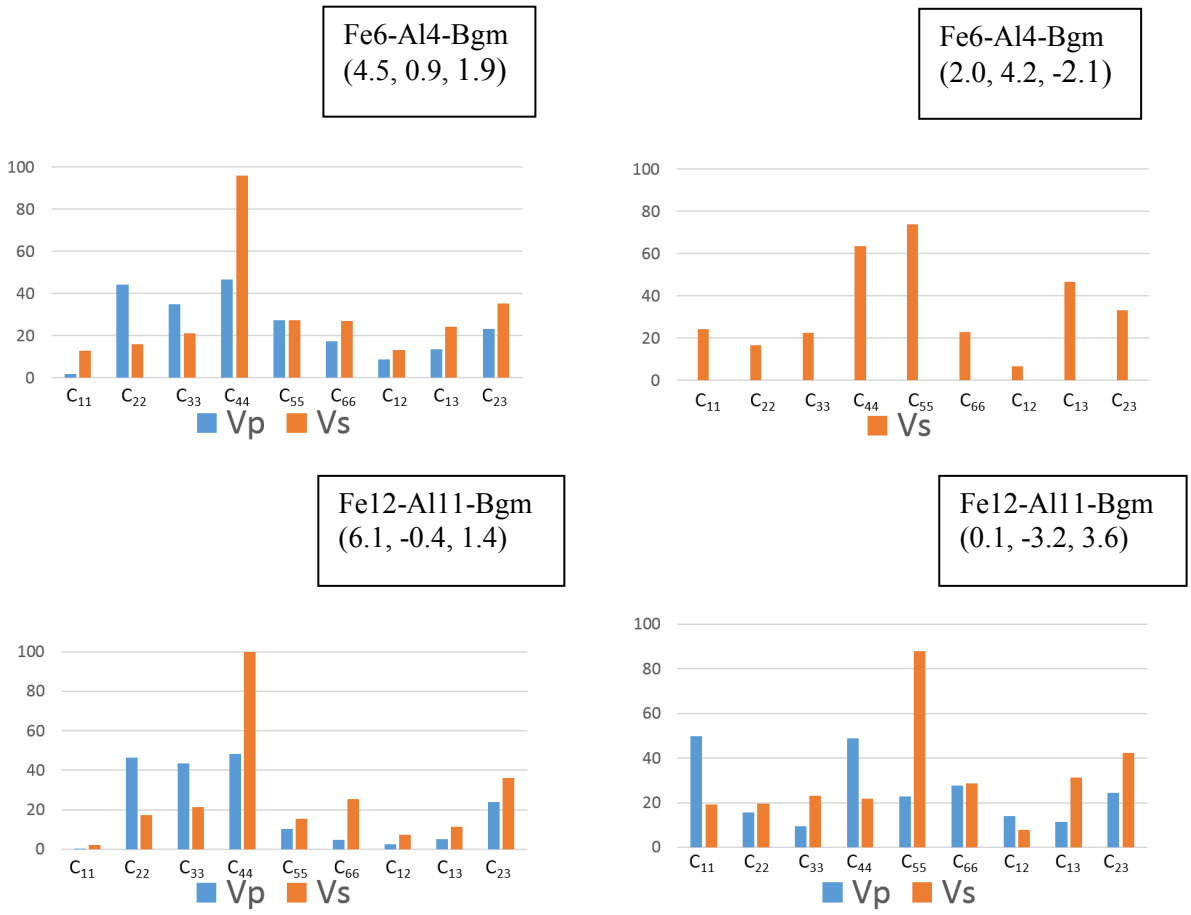


Figure 5.1: Sensitivity analysis of elastic constants for bridgmanite to experimental $V_P$ and $V_S$ velocities based on Christoffel's equations. The sensivity of elastic constants to velocity depends on crystallographic orientations, which are related to the uncertanties of each elastic constant when constraining the resluts from experimental velocity data.

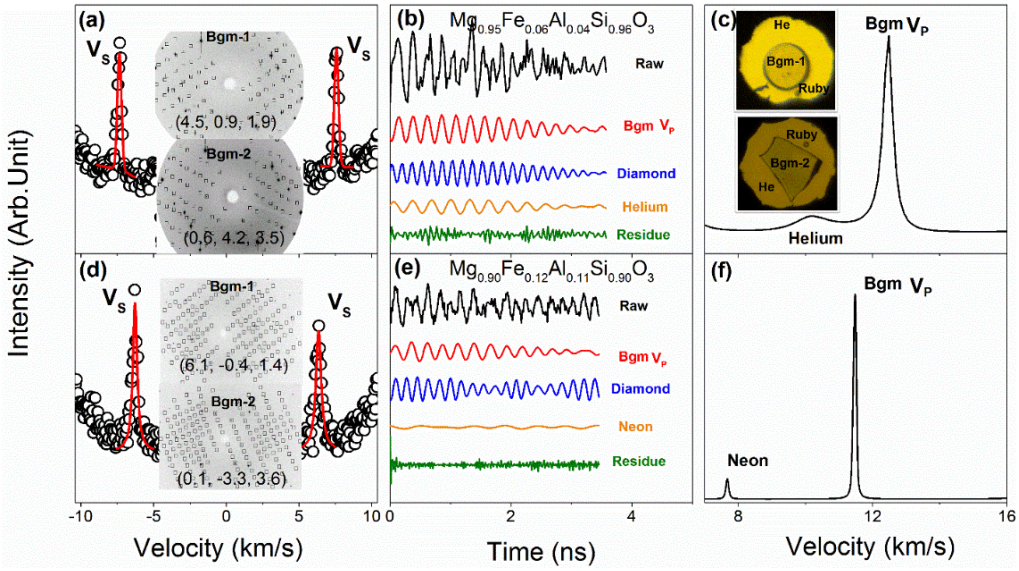


Figure 5.2: Representative experimental Brillouin light scattering, impulsive stimulated light scattering, and X-ray diffraction spectra of single-crystal bridgmanite samples at 25 GPa. (a), (b), and (c) are for Fe,Al-bearing bridgmanite (Fe6-Al4-Bgm) with a composition of $Mg_{0.95}Fe_{0.06}Al_{0.04}Si_{0.96}O_3$; (d), (e), and (f) are for Fe,Al-bearing bridgmanite (Fe12-Al11-Bgm) with a composition of $Mg_{0.90}Fe_{0.12}Al_{0.11}Si_{0.90}O_3$. (a) and (d): Brillouin spectrum of the sample showing shear wave velocity ($V_S$); (b) and (e): impulsive light scattering spectrum; (c) and (f): Flourier-transformed power spectrum for compressional wave velocity ($V_P$) measurements. Velocity of pressure medium, helium or neon, is also observed in the spectrum. Inserts in (a) and (c) represent orientation matrices determined by synchrotron X-ray diffraction at GSECARS. Inserts in (c) show two separate Fe6-Al4-Bgm single crystals Bgm-1 and Bgm-2 with orientation matrices shown in (a) loaded in sample chambers of diamond anvil cells with helium medium at 25 GPa.

Two Fe6-Al4-Bgm platelets with an orientation matrix of (4.5, 0.9, 1.9) and (2.0, 4.2, -2.1) were prepared and loaded separately into two sample chambers of DACs, together with He as pressure medium and ruby as the pressure calibrant (Figure 5.2) [*Mao et al.*, 1986]. Each DAC with a pair of 300 μm culets was equipped with a 35-μm thick pre-indented Re gasket and with a 190-μm diameter drilled hole as a sample chamber. The platelet with (4.5, 0.9, 1.9) orientation was prepared using a Focused Ion Beam (FIB) to

cut it into a round disk of approximately 70 μm in diameter, while the platelet with (2.0, 4.2, -2.1) orientation after polishing from both sides of the platelet had a diameter of approximately 80 μm ready for loading without any further cutting (Figure 5.2c insert). On the other hand, both platelets of Fe12-Al11-Bgm of approximately 60 μm in diameter each were loaded simultaneously into a sample chamber, with Ne as pressure medium and a ruby sphere as the pressure calibrant.

BLS and ISS experiments of the loaded crystals were performed at 25 GPa and 35 GPa at the Mineral Physics Laboratory of the University of Texas at Austin. A solid-state green laser with a wavelength of 532 nm (Coherent Verdi V2) was used for the Brillouin measurements running at a typical laser power of 0.6 W. Brillouin spectra were collected at the forward scattering geometry with a scattering angle of 47º using a six-pass Sandercock tandem Fabry-Perot interferometer [*Fu et al.*, 2017; *Lu et al.*, 2013; *Yang et al.*, 2016; *Yang et al.*, 2014; *Yang et al.*, 2015], which was calibrated using standard distilled water and glass on a monthly basis. The acoustic wave velocity can be calculated based on the geometry between the incident laser and measured signal and the Brillouin frequency shift:

$$v = \frac{\Delta \upsilon_B \lambda_0}{2\sin(\theta/2)}$$

where $v$ is the measured acoustic velocity, $\Delta \upsilon_B$ is the Brillouin frequency shift, $\lambda_0$ is the laser wavelength (532 nm in our experiments), and $\theta$ is the external scattering angle. For each platelet, we have collected the spectra at a 10° step rotating around the compression axis of the DAC over a range of 180° - 200° in the azimuthal direction of the platelet (Figure 5.2a,d). The ISS system is equipped with an infrared pump laser of 1064-nm wavelength and a green probe laser with 532-nm wavelength (Talisker, Coherent Company). Both lasers have a pulse width of 15 ps. In the ISS setup, the pump

laser was split into two beams which were then recombined and focused at the sample position with a crossing angle of 20.3°, which was regularly calibrated using standard distilled water and glass [*Fu et al.*, 2017; *Yang et al.*, 2015]. The probe laser was delayed by an Aerotech linear stage, and the scattered signals with a time delay between diffracted pump and probe beam are recorded by a photodiode detector, which are further Fourier-transformed to frequency-domain using the Origin Software [*Fu et al.*, 2017; *Yang et al.*, 2015]. Identical to BLS measurements, ISS spectra were collected at a 10° step rotating about the compression axis of the DAC over a range of 180° - 200° in the azimuthal direction of the platelet (Figure 5.2c,f). High-pressure X-ray diffraction experiments of the Bgm crystals were also performed using an incident X-ray wavelength of 0.3344 Å and a CCD detector at 13 IDD beamline of the GSECARS. Single crystal platelets for each composition were loaded into a DAC with helium as the pressure medium and Pt as the pressure calibrant [*Fei et al.*, 2007a; *Mao et al.*, 2017] The diffraction patterns were analyzed to derive lattice parameters and density of the samples at high pressures needed for determination of the elastic constants of the crystals.

### 5.3 RESULTS

For each pressure, a set of nine single-crystal elastic constants of the Bgm crystals for each composition was obtained by simultaneously fitting the $V_P$ and $V_S$ data of two platelets as a function of azimuthal angles via Christoffel's equation [*Every*, 1980]:

$$\left|C_{ijkl}n_i n_j - \rho v^2 \delta_{ik}\right| = 0$$

where $v$ is the measured velocity, $\rho$ is the density derived from X-ray diffraction analysis, $n_i$ is the wave direction cosine and $\delta_{ik}$ is the Kronecker delta. The single-crystal elastic constants, $C_{ijkl}$, are written in full suffix notation in Christoffel's equation, which are contracted to $C_{ij}$ in Voigt form in this study. As shown Figure 5.3 and Table 5.1, the nine

elastic constants of each single-crystal Bgm can be well constrained using our experimental data. Analysis of the sensitivity test (Figure 5.1) shows that the off-diagonal elastic constants ($C_{12}$, $C_{12}$, $C_{23}$) are relatively difficult to constrain compared to longitudinal ($C_{11}$, $C_{22}$, $C_{33}$) and shear elastic constants ($C_{44}$, $C_{55}$, $C_{66}$), respectively. The pre-analyzed sensitivities of the elastic constants to the orientation-dependent $V_P$ and $V_S$ are consistent with derived uncertainties of the elastic constants (Figure 5.1, Table 5.1). Those with small sensitivities generally have large uncertainties, and vice versa (Figures 5.1).

Table 5.1: Elastic constants and moduli of single-crystal bridgmanite at 25 GPa and 35 GPa.

| | | $C_{11}$ (GPa) | $C_{22}$ (GPa) | $C_{33}$ (GPa) | $C_{44}$ (GPa) | $C_{55}$ (GPa) |
|---|---|---|---|---|---|---|
| 25 (GPa) | Fe6-Al4 | 611(28) | 666(16) | 657(11) | 223(2) | 210(8) |
| | Fe12-Al11 | 599(10) | 686(10) | 648(10) | 205(2) | 182(2) |
| 35 (GPa) | Fe6-Al4 | 660(24) | 712(25) | 698(20) | 255(7) | 222(15) |
| | Fe12-Al11 | 644(12) | 722(14) | 674(13) | 249(5) | 205(4) |
| | $C_{66}$ (GPa) | $C_{12}$ (GPa) | $C_{13}$ (GPa) | $C_{23}$ (GPa) | $K_S$ (GPa) | G (GPa) |
| 25 (GPa) | 219(6) | 222(15) | 234(11) | 236(11) | 368(27) | 212(19) |
| | 230(7) | 260(13) | 262(13) | 267(10) | 389(18) | 198(18) |
| 35 (GPa) | 228(15) | 256(18) | 246(17) | 268(18) | 401(28) | 227(20) |
| | 233(4) | 273(5) | 274(5) | 282(5) | 410(18) | 217(15) |

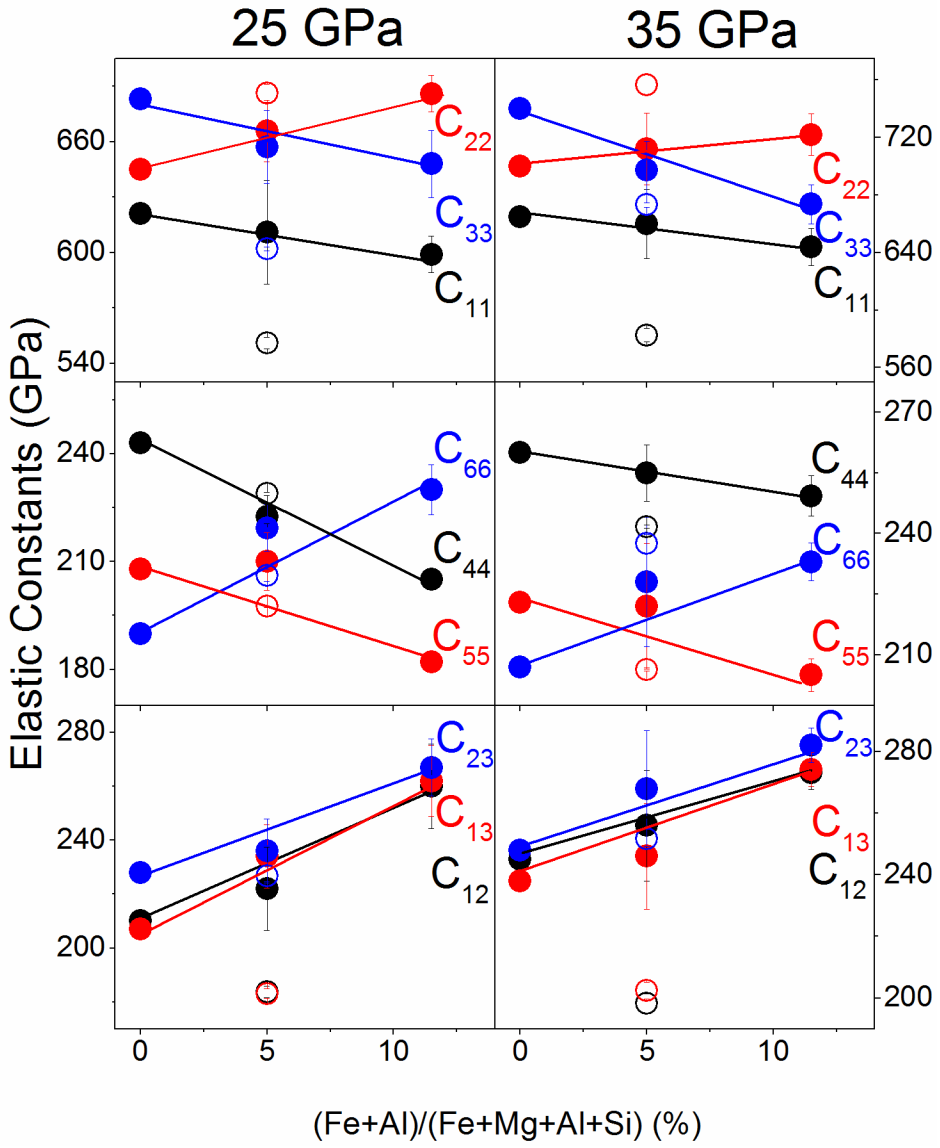


Figure 5.3: Elastic constants of single-crystal bridgmanite as a function of Fe and Al substitutions at 25 GPa and 35 GPa. The number ratios of Fe/(Mg+Fe+Si+Al) and Al/(Mg+Fe+Al+Si) of Fe6-Al4-Bgm sampleare 3.0% and 2.0%, respectively, and 6.0% and 5.5%, respectively, for Fe12-Al11-Bgm. Data for pure end member $MgSiO_3$ bridgmanite (Bgm) are calculated using theoretical values from the literature [Wentzcovitch et al., 2004]. Open circles at 25 and 35 GPa are taken from Kurnosov et al. [2017] for $Mg_{0.9}Fe_{0.1}Al_{0.1}Si_{0.9}O_3$ (Fe10-Al10-Bgm). Linear fits (solid lines) using our data for Fe,Al-bearing bgm and theoretical values for $MgSiO_3$ [Wentzcovitch et al., 2004] are used to demonstrate the combined Fe and Al substitutional effects.

To understand the combined Fe and Al substitutional effects on the elasticity of single-crystal Bgm, the nine elastic constants for each composition are plotted as a function of the total number ratio for the Fe and Al substitution at 25 GPa and 35 GPa (Figure 5.3). The elastic constants for $MgSiO_3$ Bgm from theoretical calculations and a recent experimental study on Fe10-Al10-Bgm are also plotted for comparison [*Kurnosov et al.*, 2017; *Wentzcovitch et al.*, 2004]. Comparison of these results shows that our results are drastically different from those reported by Kurnosov et al. [2017] in most elastic constants (Figure 5.3). We note that Kurnosov et al. [2017] investigated Fe10-Al10-Bgm with $Fe^{3+}/Fe^{2+}$ ratio of 0.66, which is very similar in bulk composition to our Fe12-Al11-Bgm sample with $Fe^{3+}/Fe^{2+}$ ratio of 0.8. Unfortunately, we were unable to refit the $V_P$ and $V_S$ data of Kurnosov et al. [2017] to test the reliability and uncertainties of their reported constants as original data were not made available. When comparing our results with end-member $MgSiO_3$ values in theoretical calculations at each given pressure [*Wentzcovitch et al.*, 2004], the combined Fe and Al substitution shows a first-order linear trend for all elastic constants: $C_{11}$, $C_{33}$, $C_{44}$, and $C_{55}$ decrease with increasing Fe and Al concentrations, while $C_{22}$, $C_{66}$, $C_{12}$, $C_{13}$ and $C_{23}$ increase with increasing Fe and Al contents (Figure 5.3).

Using these elastic constants as well as density from XRD analysis [Mao et al., 2017], we have further calculated the adiabatic bulk modulus ($K_S$), shear modulus ($G$), aggregate $V_P$ and $V_S$, and $V_\Phi$ of our samples, and compared them with previous theoretical and experimental values [*Kurnosov et al.*, 2017; *Wentzcovitch et al.*, 2004]. Similar to the elastic constants, these results (especially for $V_P$ and $K_S$) are not consistent with that by Kurnosov et al. [2017]: their values are significantly lower than our values and $MgSiO_3$ Bgm. When comparing our results with $MgSiO_3$ Bgm [*Wentzcovitch et al.*, 2004], the most distinct feature is the significant $V_S$ decrease with increasing Fe and Al content. Compared with $MgSiO_3$ Bgm [*Wentzcovitch et al.*, 2004], $V_S$ of Fe12-Al11-Bgm decreases by ~5%

and ~4% at 25 GPa and 35 GPa, respectively (Figure 5.4). Within experimental uncertainties, $V_P$ do not appear to be much affected by the Fe and Al substitution. On the other hand, $V_\Phi$ slightly increases with increasing Fe and Al content such that the $V_S$ and $V_\Phi$ are anti-correlated with the Fe and Al content (Figure 5.4). The compositional effect on the $V_S$ decrease and $V_\Phi$ increase is suppressed from 25 GPa to 35 GPa such that the anti-correlation is expected to be to be less significant in Fe-Al-rich Bgm. Analysis of the individual effect of Fe or Al on the velocity shows that the addition of the A-site Fe decreases $V_S$ but increases $V_\Phi$, while the substitution of Al increases $V_S$ but decreases $V_\Phi$ (Table 5.2).

Table 5.2: Fe and Al effects on sound velocities at 25 GPa and 35 GPa.

| | $dV_\Phi/dFe$ | $dV_\Phi/dAl$ | $dV_P/dFe$ | $dV_P/dAl$ | $dV_S/dFe$ | $dV_S/dAl$ |
|---|---|---|---|---|---|---|
| 25 GPa | 0.26 | -0.10 | 0.67 | -0.53 | -0.68 | 0.27 |
| 35 GPa | 0.09 | -0.15 | -0.97 | 0.15 | -0.46 | 0.15 |

We have also compared our single-crystal elastic constants with previous experimental and theoretical values as a function of pressure [*Fukui et al.*, 2016; *Karki et al.*, 1997; *Kurnosov et al.*, 2017; *Li et al.*, 2005; *Wentzcovitch et al.*, 2004] (Figure 5.5). Analysis of these results shows that the elastic constants are quite scattered. The elastic constants of Fe10-Al10-Bgm, $C_{11}$, $C_{33}$, $C_{12}$ and $C_{13}$, by Kurnosov et al. [2017] are systematically lower than our data for the Fe12-Al11-Bgm sample at the same pressures of 25 and 35 GPa. Based on our sensitivity test (Figure 5.1), these constants are all very sensitive to reliable $V_P$ measurements in a single-crystal bridgmanite, which may help explain the differences in the elastic constants and why the $K_S$ in our study is ~8% higher than that of in Kurnosov et al. [2017] at 25 and 35 GPa. On the other hand, values for $G$ between our study and Kurnosov et al. [2017] are consistent within uncertainties (Figure

5.4) because the derivation of $G$ is more dependent on $C_{44}$, $C_{55}$, and $C_{66}$ constants, and thus more sensitive to $V_S$ measurements (Figure 5.1).

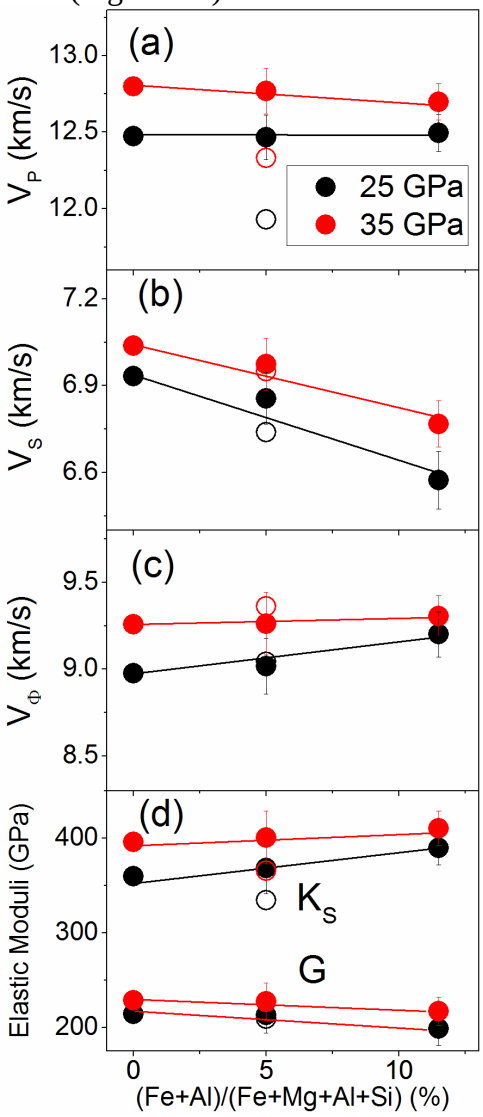


Figure 5.4: Sound velocities and elastic moduli of single-crystal bridgmanite as a function of Fe/Al substitution at 25 GPa and 35 GPa. Black symbols represent data at 25 GPa and red symbols are at 35 GPa. Data for pure end member $MgSiO_3$ bridgmanite are calculated based on theoretical values from the literature [Wentzcovitch et al., 2004]. Open symbols are results from Kurnosov et al. [2017] plotted for comparison. Linear fits (solid lines) using our data and theoretical values are used to demonstrate the Fe and Al substitutional effects.

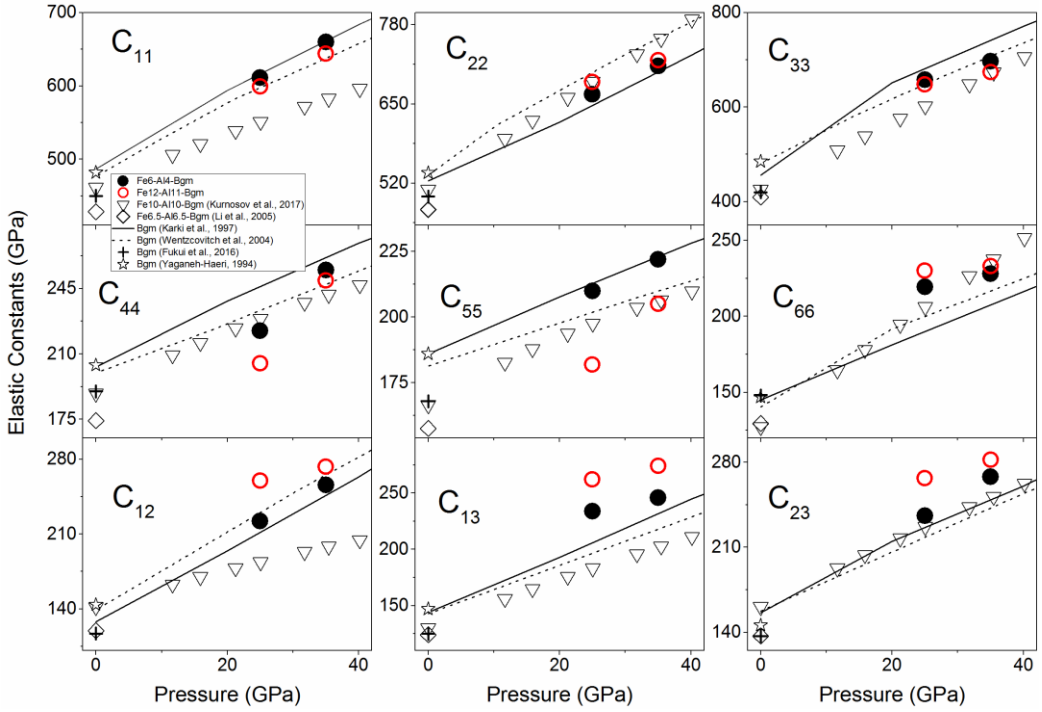


Figure 5.5: Comparison of elastic constants of single-crystal bridgmanite as a function of pressure. Solid and open circles are for single-crystal elastic constants of Fe6-Al4-Bgm and Fe12-Al11-Bgm, respectively, at high pressure in this study; open triangles at ambient and high pressures are for $Mg_{0.9}Fe_{0.1}Al_{0.1}Si_{0.9}O_3$ (Fe10-Al10-Bgm) [Kurnosov et al. 2017]; solid [Karki et al., 1997] and dashed [Wentzcovitch et al., 2004] lines are theoretical calculation for Bgm; results at ambient pressure are ploted for comparison: open diamonds for $Mg_{0.935}Fe_{0.065}Al_{0.065}Si_{0.935}O_3$ (Fe6.5-Al6.5-Bgm) [Li et al. 2005]; open stars for Bgm [Yaganeh-Haeri et al., 1994]; plus symbols for Bgm [Fukui et al., 2016].

Based on the full set of elastic constants, we have calculated the variations of $V_P$ and $V_S$ of the single-crystal bridgmanite crystals with propagation direction to investigate their $V_P$ and $V_S$ anisotropy at high pressure (Figures 5.6 and 5.7). When comparing our results with $MgSiO_3$ Bgm [*Wentzcovitch et al.*, 2004] at 25 and 35 GPa, the coupled Fe and Al substitution are found to significantly influence the directionality of $V_P$ and $V_S$. Specifically, the fastest $V_P$ in $MgSiO_3$ Bgm is approximately along the [001] direction, but

is shifted toward the [010] direction for Fe12-Al11-Bgm as a result of increasing Fe/Al content. This trend can be explained by the $C_{11}$ and $C_{33}$ decrease, and $C_{22}$ increase, resulting in $C_{22}$ larger than $C_{33}$ with increasing Fe and Al content (Figure 5.3). The shear wave splitting anisotropy is defined by the velocity difference between two orthogonally polarized shear wave velocities, $V_{S1}$ and $V_{S2}$. At 25 GPa, the $V_S$ splitting anisotropy of $MgSiO_3$ Bgm is the largest at ~0.86 km/s along [010] direction, but the direction has the lowest anisotropy at ~0.06 km for Fe6-Al4-Bgm (Figures 5.6 and 5.7).

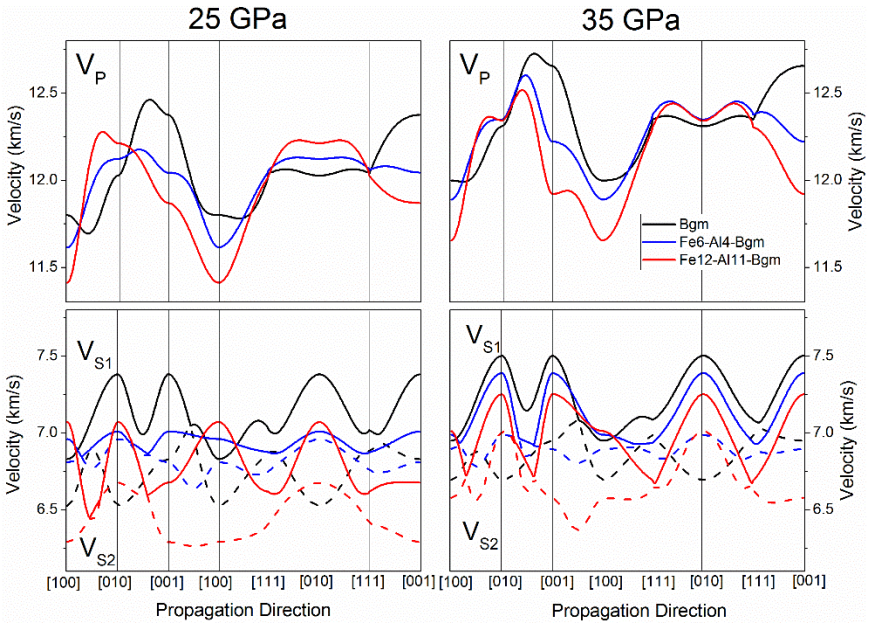


Figure 5.6: Variation of compressional ($V_P$) and shear wave velocities ($V_{S1}$ and $V_{S2}$) of single-crystal bridgmanite with propagation directions at 25 and 35 GPa. Black lines: Bgm [Wentzcovitch et al., 2004]; blue lines: Fe6-Al4-Bgm; red lines: Fe12-Al11-Bgm. For shear wave velocities, dashed lines are used for $V_{S2}$ to distinguish them from $V_{S1}$ (solid lines), where $V_{S1}$ and $V_{S2}$ are orthogonal polorized shear wave velocities; $V_{S1}$ is greater than $V_{S2}$ by definition.

**Fe6-Al4-Bgm**
**25 GPa**

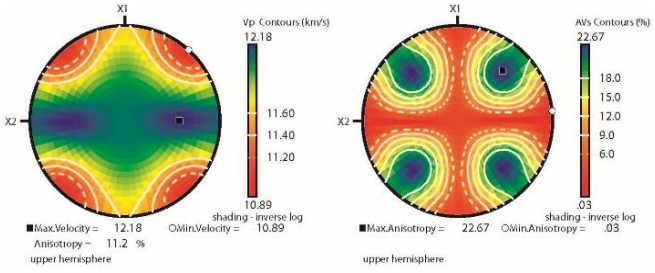


**35 GPa**

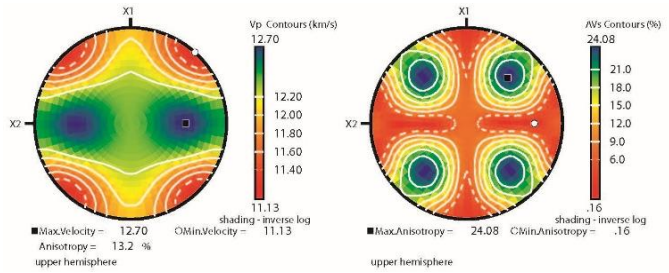


**Fe12-Al11-Bgm**
**25 GPa**

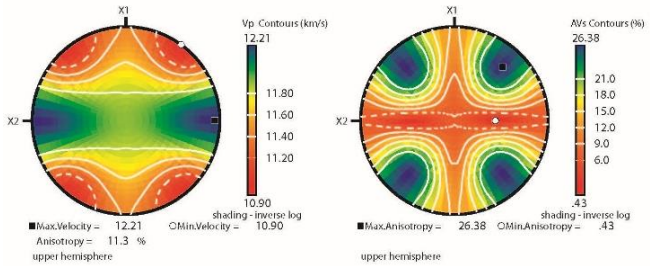


**35 GPa**

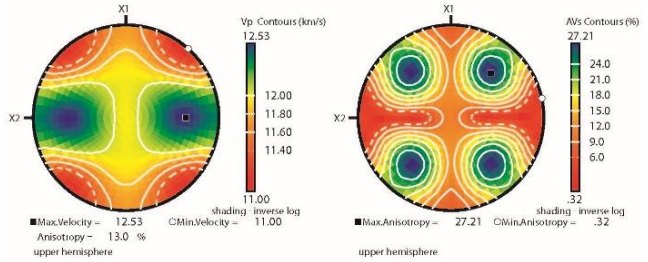


Figure 5.7: Azimuthal $V_P$ anisotropy and $V_S$ spliting anisotropy of single-crystal bridgmanite Fe6-Al4-Bgm and Fe12-Al11-Bgm at 25 GPa and 35 GPa. X1 and X2 represent crystallographic directions. Calculations are performed using the petrophysical software Unicef Careware [Mainprice, 1990].

In addition to the single-crystal anisotropy, the $V_P$ and $V_S$ anisotropy for Bgm aggregates can be calculated using the equation:

$$AV_{P,S} = \frac{2(V_{P,S}^{max} - V_{P,S}^{min})}{V_{P,S}^{aggr}}$$

where $V_{P,S}^{max}$ , $V_{P,S}^{min}$, and $V_{P,S}^{aggr}$ represent maximum, minimum, and aggregate $V_P$ and $V_S$ of Bgm crystal (Figures 5.7 and 5.8). Comparison of previous experimental and theoretical results at ambient conditions shows that A$V_P$ values are most consistent with one another, but A$V_S$ values are quite scattered, varying from 22 to 33% (Figure 5.8) [*Fukui et al.*, 2016; *Karki et al.*, 1997; *Li et al.*, 2005; *Sinogeikin et al.*, 2004; *Yeganeh-Haeri*, 1994]. By examining the anisotropy for Fe6-Al4-Bgm and Fe12-Al11-Bgm, we found that the $V_S$ anisotropy increases with increasing Fe and Al content by 16%, changing from 22-24% for Fe6-Al4-Bgm to 26-27% for Fe12-Al11-Bgm at 25-35 GPa.

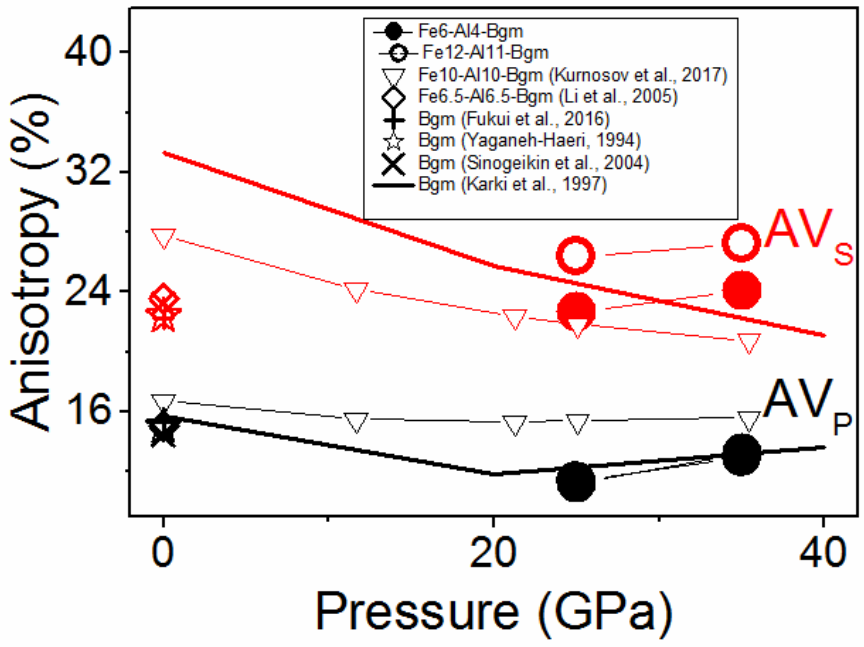


Figure 5.8: Comparison of elastic ansiotropy of single-crystal bridgmanite as a function of pressure. Black and red symbols represent shear wave anisotropy ($AV_S$) and compressional wave velocity ($AV_P$), respectively, which are calculated based on elastic constants; solid circles: Fe6-Al4-Bgm; open cirles: Fe12-Al11-Bgm; open triangles: Fe10-Al10-Bgm [Kurnosov et al. 2017]; crosses: Bgm [Sinogeikin et al., 2004]; plus symbols: Bgm [Fukui et al., 2016]; open stars: Bgm [Yagnaeh-Haeri, 1994]; open diamonds: Fe6.5-Al6.5-Bgm [Li et al. 2005].

### 5.4 Geophysical Implications

Our single-crystal elasticity study on Fe-Al-bearing Bgm, although limited to high pressure, has significant implications for understanding seismic features and mineral physics of the Earth's lower mantle. Our results on the elasticity of Fe6-Al4-Bgm and Fe12-Al11-Bgm show that the coupled effects of the Fe and Al substitution are most evident in reducing $V_S$ by 4-5% and enhancing the $V_S$ splitting anisotropy by 16% with the substitution of additional 6 at.% Fe and 7 at.% of Al for Fe12-Al11-Bgm as compared with Fe6-Al4-Bgm at topmost lower-mantle pressures. The $V_P$ anisotropy and $V_S$ splitting

anisotropy for both Fe6-Al4-Bgm and Fe12-Al11-Bgm remain relatively high at ~13% and ~24-27%, respectively, at 35 GPa, which corresponds to mid-lower mantle pressures. On the other hand, aggregate $V_P$, *Ks* as well as $V_P$ anisotropy are only marginally influenced by the Fe and Al substitution. The individual substitution effects of Fe vs. Al on the $V_P$ and $V_S$ velocities are distinctively different from each other: at 25 GPa the addition of Fe decreases $V_S$ with a negative gradient $dV_S/dFe$ of -0.68 km/s/at.% and increases $V_\Phi$ with a gradient $dV_S/dFe$ of ~0.26 km/s/at.%, while the substitution of Al increases $V_S$ with a gradient $dV_S/dAl$ of 0.27 km/s/at.% and decreases $V_\Phi$ with a negative gradient $dV_\Phi/dAl$ of −0.1 km/s/at.% (Table 5.2). Therefore, if some regions of the Earth's lower mantle are enriched in Fe and/or Al, they could exhibit distinct seismic features to be distinguishable from thermal variations, as high temperature is expected to reduce $V_P$, $V_S$, and density. Specifically, some regions of Earth's lower mantle could be significantly enriched in Fe and/or Al as a result of the subducted mid-ocean-ridge-basalt (MORB) materials, remnants of early partial melts, and/or existence of primordial materials [*Hirose et al.*, 1999; *Hirose et al.*, 2005; *Labrosse et al.*, 2007; *Ono et al.*, 2001]. These regions could be reflected as seismic heterogeneities in seismic observations [*Garnero et al.*, 2016; *Hager et al.*, 1984; *Kaneshima and Helffrich*, 1999]. Based on our study and previous results [*Li et al.*, 2005; *Mao et al.*, 2011a], one would expect to see lower-than-average $V_S$ and slightly increased $V_\Phi$ in seismic studies for these Fe and Al-enriched regions of the lower mantle. The LLSVPs beneath Africa and the Central Pacific are shown to exhibit distinct seismic features including $V_S$ decrease by 1-2%, anti-correlation between $V_\Phi$ and $V_S$, and increased density [*Garnero et al.*, 2016; *Koelemeijer et al.*, 2016; *Ritsema et al.*, 1999]. These features are, to the first order, consistent with our study for the elastic behaviors of Fe-Al-rich Bgm. Our data here also suggest that the $V_P$ and $V_S$ splitting anisotropy can be greatly affected by enrichment of Fe and Al in Bgm. For a pyrolitic composition with ~12

at.% of Fe and 11 at.% of Al in Bgm [*Irifune et al.*, 2010], the $V_S$ splitting anisotropy is 23%, which could be ~18% higher than that of $MgSiO_3$ Bgm [*Wentzcovitch et al.*, 2004] at topmost mantle pressures, while the $V_P$ anisotropy of 11% is not expected to be significantly affected by Fe and Al variation. If the Fe-Al-enriched Bgm is present at the bottom of the lower mantle with certain lattice preferred orientations [*Miyagi and Wenk*, 2016], it would likely contribute to local seismic anisotropies of the region. However, it remains unclear why seismic anisotropies are not commonly observed in most regions of the lower mantle if elastically anisotropic Fe-Al-Bgm is expected to be the most abundant mineral in the region. Further studies on high P-T single-crystal elasticity of Bgm with various Fe and Al contents, together with the consideration of their textures and slip systems, are needed to provide better constraints on the chemical and thermal origins of the seismic features as well as on the mineralogy of the lower mantle.

**Acknowledgements**

We thank N. Tomioka, N. Purejav, E. Ito, and T. Yoshino for their help with synthesis of the bridgmanite crystals at University of Okayama, V. Prakapenka for his assist with X-ray diffraction analysis of the starting crystals, C. McCammon for Mössbauer analysis of the birdgmanite crystals, and Y. Yang for FIB cutting of the starting samples. J. F. Lin acknowledges support from the Geophysics and CSEDI Programs of the U.S. National Science Foundation, the Visiting Professorship Program of the Institute for Study of the Earth's Interior, Okayama University, and HPSTAR Center. This work was supported in part by JSPS KAKENHI (26287135). X-ray diffraction patterns of the crystal were measured at GeoSoilEnviroCARS sector of the APS. GSECARS was supported by the National Science Foundation (EAR-0622171) and Department of Energy (DE-FG02-94ER14466) under Contract No. DE-AC02-06CH11357. APS is supported by 263 DOE-BES, under Contract No. DE-AC02-06CH11357.

# Chapter 6: Velocity Profiles of Fe-bearing Silicate Post-perovskite in Earth's Lowermost Mantle: Evidence for the Origin of the D" Seismic Discontinuities[4]

Observations of the lowermost mantle have found seismically distinct regions approximately 100-450 km above the core-mantle boundary, called the D" layer, which exhibit shear wave ($V_S$) splitting anisotropy, anti-correlation between shear and bulk sound velocity ($V_\Phi$), decreased $V_S$ gradient, and low Poisson's ratio [*Lay and Helmberger*, 1983]. Ever since the discovery of a silicate post-perovskite (PPv) transition in the deep lowermost mantle [*Murakami et al.*, 2004; *Oganov and Ono*, 2004], the bridgmanite (Bgm) to PPv transition has been widely used to explain observed seismic features of the D" layer, including $V_S$ splitting anisotropy and seismic discontinuities. However, experimental compressional wave velocity ($V_P$) and $V_S$ velocity constraints on Fe-bearing PPv at relevant lowermost-mantle conditions remain unavailable to verify interpretations of numerous seismic features in D". Here we have reliably measured $V_P$, $V_S$, and density of Fe-bearing PPv at lowermost mantle pressures using Impulsive Stimulated Light Scattering (ISS), Brillouin Light Scattering (BLS), and X-ray Diffraction (XRD) in high-pressure diamond anvil cells. Comparison of the velocity profiles between Fe-bearing PPv and Bgm shows that the Bgm-PPv transition containing 15% Fe is associated with a significant $V_S$ increase of ~5(±2)% and a marginal $V_P$ decrease of ~2.7(±1.5)%, resulting in a $V_\Phi$ decrease of ~7% and Poisson's ratio decrease of 10% at approximately 120 GPa, ~270 km above the core-mantle-boundary. The anti-correlation between the increased $V_S$ and decreased $V_\Phi$,

[4]This chapter is based on the article: Yang, J., Fu, S., Liu, J., Grand, S.P., Lin, J. F., Velocity Profiles of Fe-bearing Silicate Post-perovskite in Earth's Lowermost Mantle: Evidence for the Origin of the D" seismic Discontinuities. (manuscript in preparation)
Author Contributions:
Lin, J.F and Yang, J. designed the research. Yang, J. and Liu, J. synthesized the Fe-bearing post-perovskite sample. Yang, J., Fu, S and Liu, J. collected the BLS and ISS data. Lin, J.F, Grand, S.P., and Yang, J. discussed the content of the manuscript. Yang, J. and Lin, J.F wrote the paper. All authors commented on the manuscript.

together with a Poisson's ratio of 0.29 and lower velocity gradients for Fe-bearing PPv at lowermost mantle conditions, are most consistent with seismic observations beneath the Cocos plate at ~320 km above the CMB [*Hutko et al.*, 2008]. Our results thus provide strong mineral physics constraints to support the existence of Fe-bearing PPv in certain regions of the D" layer.

## 6.1 INTRODUCTION

Seismic compressional wave ($V_P$) and shear wave ($V_S$) velocities of the Earth's lower mantle are observed to mostly increase monotonically with depth, with no noticeable seismic discontinuities, from 670 km to approximately 2600 km in depth. At approximately 100-450 km above the CMB, however, significant increased $V_S$, $V_S$ splitting anisotropy, and decreased $V_S$ velocity gradient are observed seismically [*Lay and Helmberger*, 1983]. These seismic features in the D" region seem to be distributed globally, although the magnitude and depth of these seismic anomalies vary significantly in different regions [*Chaloner et al.*, 2009; *Ding and Helmberger*, 1997; *Hutko et al.*, 2008; *Kendall and Nangini*, 1996; *Kito et al.*, 2007; *Lay et al.*, 2004a; *Lay and Helmberger*, 1983; *Reasoner and Revenaugh*, 1999; *Schlaphorst et al.*, 2016; *Thomas et al.*, 2004; *Zhang and Lay*, 1984]. Beneath the Cocos plate a sharp increase in $V_S$ of 1-3% was observed in conjunction with a negative (up to 3%) or a small positive (<1%) change in $V_P$ [*Ding and Helmberger*, 1997; *Hutko et al.*, 2008; *Kendall and Nangini*, 1996; *Kito et al.*, 2007; *Lay and Helmberger*, 1983; *Thomas et al.*, 2004]. In addition, both regional and global seismic studies show a robust feature of seismic anisotropy of 1-3% in which horizontally polarized shear waves ($V_{SH}$) travel faster than vertically-polarized shear waves ($V_{SV}$) in the D" layer beneath the circum-Pacific [*Lay et al.*, 1998; *Matzel et al.*, 1996]. Seismic tomographic studies further reveal two massive anomalous zones with lowered $V_S$ beneath the Pacific Ocean and the

Southern African continent [*Garnero and McNamara*, 2008], called Large Low Shear Velocity Provinces (LLSVPs), which are believed to be surrounded by subducted slabs with higher-than-average velocity [*Garnero et al.*, 2016]. High resolution seismic studies also find thin patches at CMB with strong velocity reductions, called Ultralow Velocity Zones (ULVZs), which are observed at the edge of the LLSVPs [*McNamara et al.*, 2010]. Velocity profiles of candidate lowermost-mantle constituents at relevant P-T conditions are urgently needed to explain these aforementioned seismic features in the D" region, LLSVPs, and ULVZs. From a mineral physics perspective, seismic parameters across the Bgm-PPv transition at expected P-T conditions of the D" region [*Murakami et al.*, 2004] have been used to explain discontinuities not only for the D" region [*Iitaka et al.*, 2004; *Oganov and Ono*, 2004], but also for the ULVZ [*Mao et al.*, 2006]. It has also been suggested that D" may be regionally enriched in Fe [*Mao et al.*, 2006]. Knowing the cause of the D" seismic discontinuities as well as LLSVPs and ULVZs can provide new insights into the physical, chemical, and rheological states at the CMB, which in turn can lead to a better understanding of core-mantle interactions and heat transfer at the CMB as well as mantle convection.

The D" discontinuity was first proposed to be caused by a solid-solid phase transition with a large positive Clapeyron slope [*Sidorin et al.*, 1999], which was later supported by the discovery of the PPv transition with a Clapeyron slope of ~7 MPa/K [*Murakami et al.*, 2004; *Oganov and Ono*, 2004; *Tsuchiya et al.*, 2004b]. Theoretical calculations show that the $MgSiO_3$ PPv transition produces a positive $V_S$ change ($\Delta V_S$) up to 5%, while the change in $V_P$ ($\Delta V_P$) is significantly less at ~1% [*Caracas and Cohen*, 2005; *Iitaka et al.*, 2004; *Oganov and Ono*, 2004; *Tsuchiya and Tsuchiya*, 2006; *Wentzcovitch et al.*, 2006; *Wookey et al.*, 2005]. Previous studies further showed that PPv can display strong

lattice preferred orientations and, together with its high elastic anisotropy, can produce 1-3% $V_S$ splitting anisotropy with $V_{SH} > V_{SV}$ [*Iitaka et al.*, 2004]. However, the interpretation of the aforementioned seismic features at the D" region using the occurrence and texturing of PPv phase has remained mostly theoretical because of limited experimental data at lowermost mantle conditions. Experimentally-measured $V_S$ for the Bgm-PPv transition with $MgSiO_3$ composition shows a velocity contrast of 0.5% at most [*Murakami et al.*, 2007], indicating that the PPv transition cannot be used to explain the $V_S$ discontinuity at D" layer. To better understand seismic features at the D" region, we have used complimentary laser and X-ray spectroscopic techniques coupled with a DAC to measure $V_P$ using ISS, $V_S$ using BLS, and lattice parameters and density using XRD of Fe-bearing PPv at D" pressures (Figure 6.1). These results are used to evaluate velocity discontinuities and correlations as well as Poisson's ratio across the PPv transition at lowermost mantle pressures. We compare velocity profiles of Fe-bearing Bgm and PPv with seismic observations for seismic discontinuities in D", as well with observations of LLSVPs, and ULVZ regions to verify the possible existence of Fe-bearing PPv and iron enrichment in the lowermost mantle.

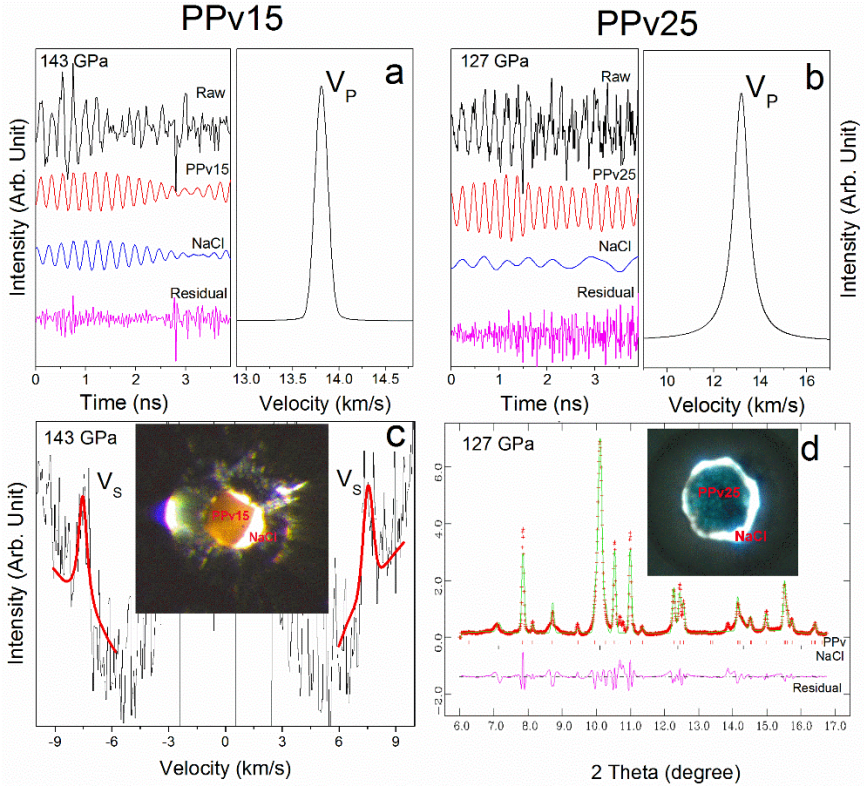


Figure 6.1: Representative experimental spectra of the synthesized Fe-bearing PPv samples at high pressures and 300 K. Impulsive light scattering spectrum (right panel) and Fourier-transformed power spectrum for compressional wave velocity ($V_P$) (left panel) of PPv15 at 143 GPa (a) and PPv25 at 127 GPa (b); (c) Brillouin spectrum of PPv15 at 143 GPa, together with an inset photo of the sample with NaCl as pressure medium; (d) X-ray diffraction spectrum of PPv25 with a photo insert of the sample. Black lines in Figure 6.1c represent the raw Brillouin spectrum and red lines show the fitted shear wave velocity ($V_S$). Red crosses in Figure 6.1d indicate the raw diffraction spectrum while the green lines represent Le Bail fit; red and black vertical bars indicate peaks for PPv25 and NaCl phases, respectively. Incident X-ray wavelength used was 0.3344 Å.

## 6.2 METHOD

Fe-bearing silicate post-perovskite samples (PPv15 or PPv25) were synthesized from starting materials of silicate glass [$(Mg_{0.85}Fe_{0.15})SiO_3$] and polycrystalline enstatite [$(Mg_{0.75}Fe_{0.25})SiO_3$], respectively. The starting glass was synthesized from a mixture of

MgO, $Fe_2O_3$, $Al_2O_3$ and $SiO_2$ powders in appropriate ratios using a high-temperature furnace (See [*Mao et al.*, 2014b] for more details on the synthesis of Fe-bearing silicate glass). Enstatite was synthesized from the powders of $SiO_2$, MgO, and $^{57}Fe_2O_3$ mixed in the appropriate ratio, which was placed in a furnace with well controlled oxygen fugacity [*Mao et al.*, 2010]. An electron microprobe was used to analyze the chemical composition and homogeneities of the starting glass and enstatite, which showed $(Mg_{0.85}Fe_{0.15})SiO_3$ for the glass and $(Mg_{0.75}Fe_{0.25})SiO_3$ for enstatite sample, respectively.

The glass starting materials were polished down to approximately 10-12 μm in thickness and subsequently cut into pieces around 60 μm in diameter, while polycrystalline enstatite was slightly compressed between two diamond anvils to prepare for a sample disk of 10 μm in thickness and 60 μm in diameter. The sample disk was loaded into a sample chamber and sandwiched between two dried NaCl layers of approximately 5 μm in thickness which was served as the pressure medium, pressure calibrant, and thermal insulator. Each sample assemblage was loaded into a short symmetric diamond anvil cell (DAC) quipped with a pair of beveled diamonds of 150/300 μm in culet size and a pre-indented Re gasket with a hole 80 μm in diameter and 28-μm thick. Enstatite loaded in the sample chamber was directly compressed to 125 GPa at 300 K, and laser heated at ~2000 K for approximately 5 hours while the glass sample was compressed to 143 GPa at 300 K and laser heated at ~2200 K for approximately 30 hours to fully transform the starting materials to PPv at GSECARS of the Advanced Photon Source (APS), Argonne National Laboratory (ANL). During the synthesis, the laser heating spot (approximately 10 μm) was constantly scanned across the whole sample by slowly moving the sample stage every few seconds. This process was used to minimize chemical diffusion and to ensure that the sample was heated as uniformly as possible. Analysis of the XRD spectra of the laser

heated samples using an incident X-ray beam of 2 μm and a wavelength of 0.3344 Å confirmed the successful synthesis of the PPv15 and PPv25 samples (Figure 6.1d and Figure B1). XRD spectra measured from various spots of the samples showed consistent lattice parameters without experimental uncertainties, indicating that the starting samples were successfully transformed into PPv phase. The pressure of the sample was determined from analysis of the XRD spectra using the NaCl EoS [*Fei et al.*, 2007a]. After a pressure change, each sample was then laser annealed at around 1800 K for 2 hours across the whole sample at 13IID beamline of the GSECARS to release possible non-hydrostaticity and to further confirm the crystallinity of PPv samples as well as the sample pressures. In total, XRD patterns were collected from PPv15 at 143, 134 and 122 GPa and from PPv25 at 127, 122 GPa. XRD patterns of the PPv samples have been measured in decompression at each given pressure to determine the lattice parameters, unit cell volume and density the samples. The cell parameters of PPv15 and PPv25 were calculated using the Le Bail fits to the experimental XRD patterns. Densities of the samples were then calculated using the starting composition of the samples and the derived unit cell volumes (Table 6.1).

The synthesized PPv15 and PPv25 samples were used for BLS and ISS experiments in the Mineral Physics Laboratory of the University of Texas at Austin. BLS and ISS spectra were collected from PPv15 in the transmitted geometry, but PPv25 sample was only sufficiently transparent for ISS measurements (it was too dark to permit BLS measurements). The BLS system was equipped with a Coherent Verdi V2 laser operating at 532 nm wavelength, together with a JRS interferometer and an APD detector (Count-10B Photo Counting Module with approximately 5 cps from Laser Components, Inc.). The laser power was set at 0.6 W for most of the measurements. The focused laser beam size at the sample position was approximately 20 μm in diameter while the scattering angle of

the BLS system was set at 47°, which was calibrated against $SiO_2$ glass and purified water standards. The data collection time was typically 12-18 hours for each pressure point due to relatively weak acoustic signals from the samples when compared with the background noise and strong diamond $V_S$ peak. To reduce the overlap of the diamond $V_S$ peak with the sample $V_S$ peak, the crystallographic orientations for each pair of diamond anvils (the anvils were standard design in 100 orientation) used in the experiments were aligned in the alignment process of the DAC. BLS spectra of the samples were collected from an orientation where the $V_S$ of the diamond anvils were at maximum velocity to allow the maximum window and lowest background for collecting the $V_S$ peak of the samples. The measured BLS spectra were fitted with a Lorentzian peak shape (Figure 6.1c).

High-pressure ISS spectra were collected from both PPv15 and PPv25 samples. The ISS system was equipped with a pump laser of 1064 nm wavelength and a probe laser with a 532-nm wavelength (Talisker, Coherent Company), which had a pulse width of 15 ps. The pump laser was split into two beams which were then recombined at the sample position with a crossing angle of 20.3° and a focused beam size of 25 μm. The probe laser was delayed by an Aerotech linear stage by as long as 20 ns, while the diffracted ISS signals were collected by a photodiode detector. The data collection time for each ISS spectrum was typically 4 hours with 1-2 mm step size. The time-domain raw ISS spectra were Fourier-transformed to frequency-domain power spectra based on the Burg method using the MATLAB and OriginPro 9.1 software. The acoustic wave velocities of the sample were calculated from the frequency based on the laser-beam geometry (Figure 6.1a), which was calibrated using glass and water standards. The interfacial waves in the ISS spectra were extracted in some data analyses but were not used for the modelled velocity profiles. Thus,

only $V_P$ velocities of the samples were used from the ISS measurements while the $V_S$ velocities were derived from the BLS experiments.

### 6.3 RESULTS

Two Fe-bearing PPv samples, $Mg_{0.85}Fe_{0.15}SiO_3$ (PPv15) and $Mg_{0.75}Fe_{0.25}SiO_3$ (PPv25), were synthesized in laser-heated diamond anvil cells at beamline 13-IDD at GSECARS, Advanced Photon Source (APS), Argonne National Laboratory (ANL). The formation of the Fe-bearing PPv phase was confirmed using *in situ* XRD measurements, which also provide lattice parameters and densities of the samples at high pressures (Figure 6.1d and Figure B1). Our synthesized PPv15 was optically translucent in transmitted light (Figure 6.1c insert) to sufficiently permit both ISS and BLS measurements at 143, 134 and 122 GPa, while PPv25 was sufficiently semi-translucent (Figure 6.1d insert) to only allow for ISS measurements at 127 and 122GPa (Figures 6.1, 6.2; Table 6.1). Together with the $V_P$ and $V_S$ measurements from ISS and BLS, the bulk sound velocity ($V_\Phi$) of PPv15 is calculated using $V_\Phi = \sqrt{{V_P}^2 - 4{V_S}^2/3}$. Because $V_S$ was not measured in the PPv25 sample at high pressure, literature $V_\Phi$ values [*Mao et al.*, 2014a] and our $V_P$ data for PPv25 are used to calculate its $V_S$ values at high pressures using the aforementioned equation (Figure 6.2). These results also allow us to evaluate the pressure gradients of the velocities as well as the Fe compositional effects on the velocities of Bgm and PPv at lowermost mantle pressures (See Appendix B for details). Comparison of the velocities of PPv15 and PPv25 at 120 GPa shows that $V_P$ and $V_S$ of PPv15 are 0.48 km/s (or 3.5%) and 0.11 km/s (or 1.5%) lower than that of PPv25 as a result of additional 10% Fe substitution (Figure 6.2).

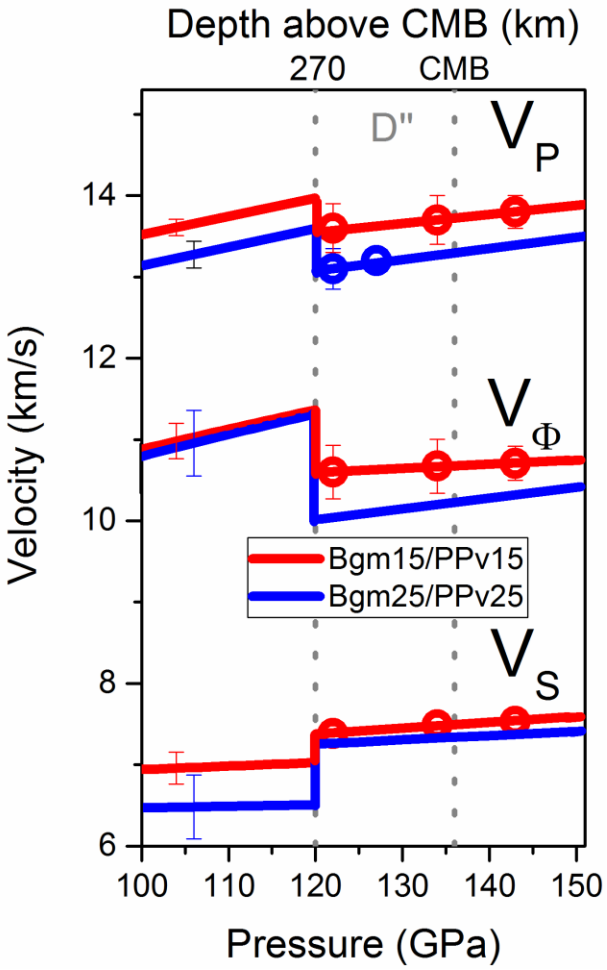


Figure 6.2: Velocity profiles of Fe-bearing PPv and Bgm at lowermost mantle pressures. Red symbols represent measured velocity for PPv15, while blue symbols are for PPv25. The measured velocity results were linearly fitted to show their pressure gradients as shown in red lines for PPv15 and blues line for $V_P$ of PPv25. For PPv15, $V_P$ results are measured from ISS experiments, $V_S$ from BLS experiments, and $V_\Phi$ results are calculated using $V_\Phi = \sqrt{{V_P}^2 - 4{V_S}^2/3}$. For PPv25, $V_P$ results are measured from ISS experiments, $V_\Phi$ line is taken from in Mao et al., 2014, and $V_S$ results are calculated using $V_S = \sqrt{3({V_P}^2 - {V_\Phi}^2)/4}$. Grey vertical dotted lines indicate the D" region ranging from the core-mantle boundary at 136 GPa at CMB to 120 GPa (~270 km above the boundary) Velocity profiles with representative error bars for Fe-bearing Bgm are modelled using literature data (See Appendix B and Table B1 for details).

Table 6.1: Sound velocities of PPv15 and PPv25 at high pressures.

| $Mg_{0.85}Fe_{0.15}O_3$ (PPv15) | | | | |
|---|---|---|---|---|
| Pressure (GPa) | $V_P$ (km/s) | $V_S$ (km/s) | $V_\Phi$ (km/s) | density(g/cm$^3$) |
| 143 | 13.8(2) | 7.54(8) | 10.7(3) | 6.152 |
| 134 | 13.7(3) | 7.44(9) | 10.7(4) | 6.021 |
| 122 | 13.6(3) | 7.38(9) | 10.6(4) | 5.794 |

| $Mg_{0.75}Fe_{0.25}SiO_3$ (PPv25) | | | | |
|---|---|---|---|---|
| Pressure (GPa) | $V_P$ (km/s) | $V_S$ (km/s) | $V_\Phi$ (km/s) | density(g/cm$^3$) |
| 127 | 13.2(1) | 7.34[b] | 10.12[a] | 5.913 |
| 122 | 13.1(2) | 7.28[b] | 10.05[a] | 5.884 |

[a]$V_\Phi$ data were interpolated from Mao et al., 2014 for PPv containing 25% of Fe [*Mao et al.*, 2014a].

[b]$V_S$ were calculated based on equations $V_\Phi = \sqrt{{V_P}^2 - 4{V_S}^2/3}$, where $V_P$ were from this study.

To evaluate the velocity contrasts and gradients across the Bgm-PPv transition, we have modeled the velocity profiles of Fe-bearing Bgm up to 120 GPa using elasticity and equation of states in literature reports [*Ballaran et al.*, 2012; *Chantel et al.*, 2012; *Li and Zhang*, 2005] (Figure 6.2 and Table B1; See Appendix B for elastic modelling details). Comparison of the velocity profiles of Fe-bearing Bgm and PPv at approximately 120 GPa shows that $\Delta V_S$ between Bgm15 and PPv15 at 120 GPa is about +5(±2)%, which is much more than the approximately +0.5% difference for the $MgSiO_3$ Bgm-PPv transition from BLS experiments [*Murakami et al.*, 2007]. $\Delta V_P$ is −2.7(±1.5)% for PPv15 and −3.0(±1.0)% for PPv25. The jump in $V_S$ and the slight decrease in $V_P$ contribute to a significant $V_\Phi$ decrease of ~7(±3) % for the PPv15 transition (Figure 6.2). We have tested the robustness of these velocity changes using available elastic parameters and EoS parameters for the thermoelastic modelling (Table B1), and have consistently found that the jump in $V_S$ across the Bgm-PPv transition is strong and positive while the discontinuity in $V_P$ is negative but could be minimal if the uncertainties of both Bgm and PPv are considered. Based on the

$V_P$ and $V_S$ extrapolation for Bgm, the pressure derivative of $V_P$ ($dV_P/dP$) for both Bgm15 and Bgm25 is ~0.023 km·s$^{-1}$·GPa$^{-1}$ at pressures between 100 and 120 GPa, which is greater than that of PPv15 and PPv25 with a $V_P$ gradient of 0.011 and 0.014 km·s$^{-1}$·GPa$^{-1}$, respectively (Table 6.2). The pressure derivative of $V_S$ ($dV_S/dP$) of Bgm15 is approximately 0.004 and ~0.002 km·s$^{-1}$·GPa$^{-1}$ for Bgm25, which are slightly less than that of the PPv15 (~0.007 km·s$^{-1}$·GPa$^{-1}$) and PPv25 (~0.005 km·s$^{-1}$·GPa$^{-1}$).

To apply our results to understand seismic features at the lowermost mantle regions, we have also calculated Poisson's ratio (ν) of Fe-bearing Bgm and PPv:

$$\nu = \frac{1}{2}\frac{(V_P/V_S)^2 - 2}{(V_P/V_S)^2 - 1}$$

Based on the calculations using measured $V_P$ and $V_S$, Poisson's ratio of PPv15 is 0.29 at ~270 km above the CMB and its pressure gradient is $-1.19\times10^{-5}$ km$^{-1}$, a slightly negative value at lowermost mantle pressures (Figure 6.3d). The reduction in Poisson's ratio across the PPv15 transition is approximately 12.1(±5.6)% which is consistent with a theoretically predicted reduction of 7% for $MgSiO_3$ PPv transition [*Wookey et al.,* 2005].

Table 6.2: Pressure gradients of $V_P$ and $V_S$ for Fe-bearing PPv and Bgm at the lowermost mantle pressures.

| $Mg_{0.75}Fe_{0.25}SiO_3$ | | | |
|---|---|---|---|
| | $dV_P/dP$ (km/s/GPa) | $dV_S/dP$ (km/s/GPa) | $dV_\Phi/dP$ (km/s/GPa) |
| PPv25 | 0.014 | 0.005 | 0.020 |
| Bgm25 | 0.023 | 0.002 | 0.026 |
| $Mg_{0.85}Fe_{0.15}SiO_3$ | | | |
| | $dV_P/dP$ (km/GPa) | $dV_S/dP$ (km/s/GPa) | $dV_\Phi/dP$ (km/s/GPa) |
| PPv15 | 0.011 | 0.007 | 0.005 |
| Bgm15 | 0.023 | 0.004 | 0.024 |

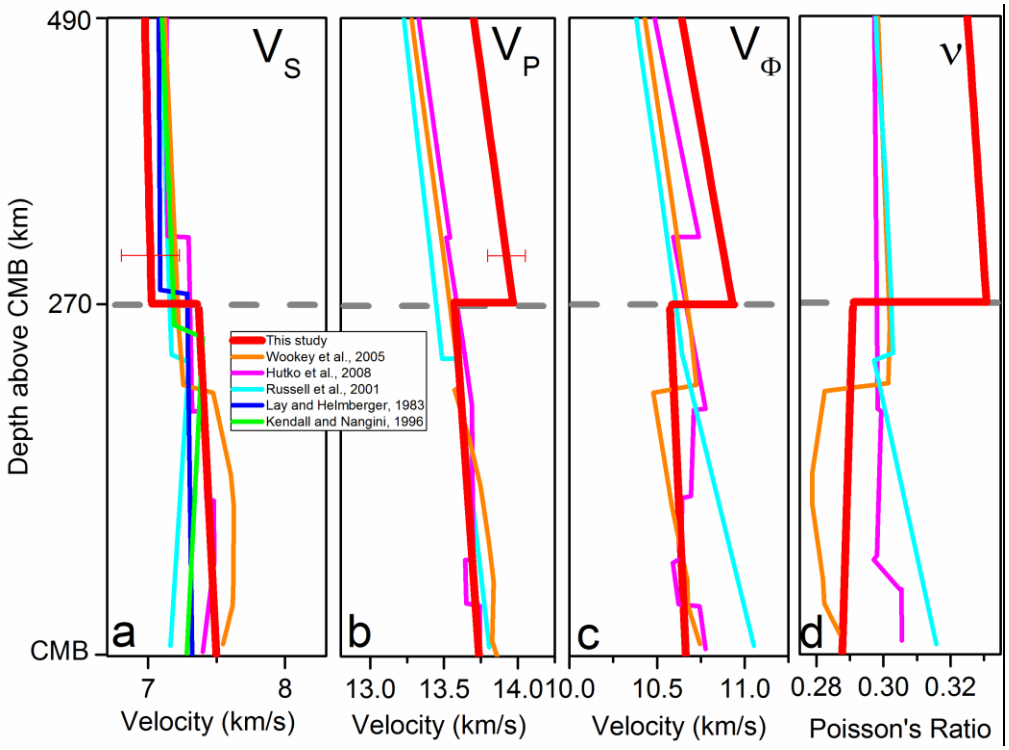


Figure 6.3: Velocity profiles and Poisson's ratio across the Fe-bearing PPv transition at the D" region. Representative seismic observations of the D″ region are also plotted for comparison (blue, pink, green and cyan lines) [*Hutko et al.*, 2008; *Kendall and Nangini*, 1996; *Lay and Helmberger*, 1983; *Russell et al.*, 2001]. The transition depth is selected to be at 2620 km depth or 270 km above the core-mantle boundary (grey dotted line). Thick red lines represent modeled velocity profiles and Poisson's ratio (ν) of PPv and Bmg containing 15% Fe at high pressure and 300 K. Orange line: theoretical data for velocity profile across the phase boundary between Bgm and PPv [*Wookey et al.*, 2005].

### 6.4 Discussion and Implication

To invoke PPv for explaining observations of the D" discontinuities, we compared the velocity contrasts to that reported by theoretical calculations [*Wookey et al.*, 2005] and observed by seismology at D" [*Hutko et al.*, 2008; *Kendall and Nangini*, 1996; *Lay and Helmberger*, 1983; *Russell et al.*, 2001] (Figure 6.3). A survey of literature on seismic studies of the D" layer shows that seismic $V_S$ discontinuities at the D" layer are more

prevalent than $V_P$ discontinuities. As shown in Figure 6.3, the occurrence of polycrystalline PPv15 alone can contribute to a $V_S$ increase of ~5(±2)%, $V_P$ decrease of ~2.7(±1.5)%, an anti-correlation between $V_S$ and $V_\Phi$, and a decrease in Poisson's ratio of ~12.1(±5.6)% at high pressure and room temperature. The anti-correlated $V_S$ and $V_\Phi$ across the PPv transition is especially interesting as this is not a common feature across a structural transition at high pressures but has been observed seismically in the D" region (Figure 6.3). To first order, our measurements are in good agreement with seismic observations beneath the Cocos plate and southeast Asia, where a large increase in $V_S$ has been seen [*Kendall and Nangini*, 1996; *Lay and Helmberger*, 1983] together with negative changes in $V_P$ and $V_\Phi$ [*Chaloner et al.*, 2009; *Hutko et al.*, 2008]. However, it contradicts seismic observations beneath the central Pacific where a positive change in both $V_S$ and $V_P$ is observed [*Russell et al.*, 2001]. On the other hand, the discontinuity magnitude predicted here is larger than the seismic observed ones. However, the coexistence of ferropericlase, the second most abundant mineral in the lower mantle, is likely to reduce the magnitude of the discontinuity for the Bgm-PPv transition alone. Assuming Bgm presents at the top of D" and completely transforms to PPv across the D", Fe and Al partitioning between the Bgm and PPv will also affect their respective velocity profiles and thus the magnitude of the discontinuities across the D" region [*Piet et al.*, 2016]. We should note that, however, the trend of the Fe and Al partitioning between Bgm-PPv remains to be further understood. If Fe preferentially partitions into Bgm over PPv [*Hirose et al.*, 2008; *Sinmyo et al.*, 2011], where the partition coefficient is ~1.8-2.7, our present study indicates that the Fe-bearing PPv transition would have a higher $V_S$ increase and insignificant $V_P$ change (Figure 6.2). If Fe preferentially partitions into PPv [*Kobayashi et al.*, 2005], the $V_S$ increase will be reduced, i.e., the $V_S$ contrast is less than ~2% if PPv25 exists in the D" region with Bgm10 on top. Our derived velocity discontinuities are for polycrystalline Fe-bearing PPv transition, but the lattice

preferred orientations of PPv in the D" region is also expected to influence the speed of seismic waves and thus the magnitudes of these velocity discontinuities [*Wu et al.*, 2017].

Figure 6.4 summarized further seismic studies of D" as well as the seismic anomalies associated with ULVZs and LLSVPs [*Ding and Helmberger*, 1997; *Gassner et al.*, 2015; *Hutko et al.*, 2008; *Kendall and Nangini*, 1996; *Kito et al.*, 2007; *Lay et al.*, 2004a; *Lay and Helmberger*, 1983; *Lay et al.*, 2006; *Reasoner and Revenaugh*, 1999; *Rost et al.*, 2005; *Schlaphorst et al.*, 2016; *Thomas et al.*, 2004; *Thorne and Garnero*, 2004; *Zhang and Lay*, 1984]. For the D" region, most $V_S$ discontinuities are positive with a jump up to ~1-3%, which are consistent with our experimental observations and previous theoretical calculations for the PPv transition, supporting the existence of the PPv in these D" regions. On the other hand, $V_P$ discontinuities in seismic observations of the D" region are not as clear, showing $V_P$ discontinuities to be either positive or negative (Figure 6.4). For example, some seismic observations of the D" discontinuity underneath Siberia/Eurasia or central Pacific have reported large-amplitude increases in $V_P$ (1-3%) [*Russell et al.*, 2001; *Thomas and Weber*, 1997; *Weber and Davis*, 1990]. However, it has been suggested that these large $V_P$ increases may still be reconciled with the phase transition between Bgm and PPv, if a proportion of PPv grains preferentially align with fast crystallographic direction due to lower mantle flow [*Thomas et al.*, 2011]. This seismic anisotropic D" layer is possibly created by the geodynamic flow of slab materials that result in development of crystallographic preferred orientations of Fe-bearing PPv with a dominant (001) texture that would produce a shear wave splitting anisotropy of ~3.7% with $V_{SH} > V_{SV}$ and likely a $V_P$ discontinuity [*Wu et al.*, 2017]. Some seismic studies have argued that PPv does not exist globally in the D" region due to the lack of seismic evidence for the velocity discontinuity [*Chambers and Woodhouse*, 2006]. The absence of the discontinuity

in the D" layer may be attributed to the broadness of the PPv transition in pyrolite lower mantle, and/or distinct compositions of PPv in different lowermost mantle regions. Based on mineral physics experiments, the transition pressure range depends strongly on the chemical composition of constituent minerals, which in turn affects the density and velocity changes [*Cobden et al.*, 2015]. Previous studies show that the pressure range for the PPv transition in a pyrolitic composition is about ~10-30 GPa, which is broader than the transition range of 3-15 GPa for a mid-ocean-ridge-basalt (MORB) composition [*Grocholski et al.*, 2012]. It is thus conceivable that the Bgm-PPv transition with a pyrolitic composition may be too broad to be detected seismically, and especially in $V_P$ that is only associated with a small change. That may be the reason why $V_S$ and $V_P$ discontinuities are commonly observed in faster-than-average-velocity regions that may be related to MORB in composition [*Grocholski et al.*, 2012; *Hutko et al.*, 2008; *Kendall and Nangini*, 1996]. Based on current understanding in mineral physics and the seismic evidence, the occurrence of the PPv phase remains the most viable candidate to explain the origin of D" seismic structures.

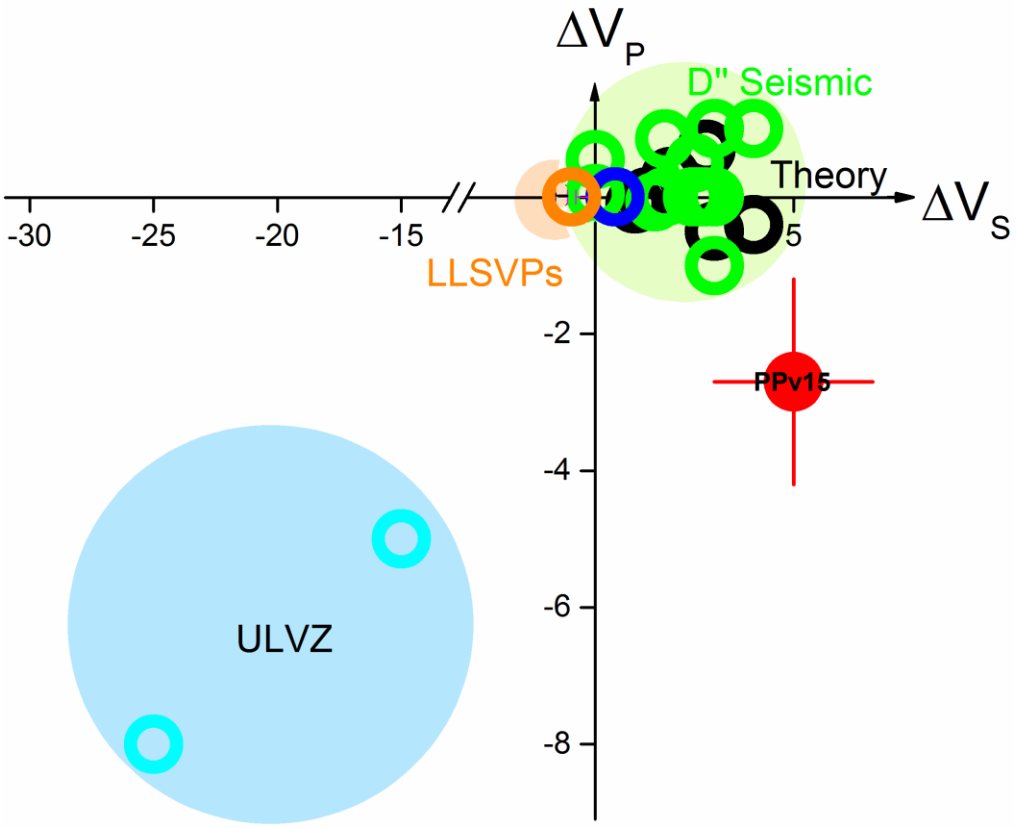


Figure 6.4: Seismic $V_P$ and $V_S$ discontinuities at the lowermost mantle compared with velocity changes across the Fe-bearing PPv transition. Three seismically distinct regions are plotted for comparison: D" discontinuity mainly under the Cocos plate (green open circles) [*Chaloner et al.*, 2009; *Ding and Helmberger*, 1997; *Hutko et al.*, 2008; *Kendall and Nangini*, 1996; *Kito et al.*, 2007; *Lay et al.*, 2004a; *Lay and Helmberger*, 1983; *Reasoner and Revenaugh*, 1999; *Schlaphorst et al.*, 2016; *Thomas et al.*, 2004; *Zhang and Lay*, 1984], LLSVPs (orange open circle)[*Lay et al.*, 2006], and ULVZs (cyan open circles) [*Gassner et al.*, 2015; *Lay et al.*, 2006; *Rost et al.*, 2005; *Thorne and Garnero*, 2004]. These regions are highlighted in larger circles with lighter corresponding colors to guide the eye. Experimental and theoretical mineral physics data for the velocity changes across the Bgm-PPv transition are plotted for comparison: theoretical calculations (black open circles) [*Caracas and Cohen*, 2005; *Iitaka et al.*, 2004; *Oganov and Ono*, 2004; *Tsuchiya and Tsuchiya*, 2006; *Wentzcovitch et al.*, 2006; *Wookey et al.*, 2005], experimental results for PPv15 and PPv25 in this study (red circles), and experimental $MgSiO_3$ PPv (blue open circle) [*Murakami et al.*, 2007].

Other enigmatic seismic features in the lowermost mantle are LLSVPs with lowered $V_S$ as well as ULVZs with strong reductions in $V_S$ by 10-30% and in $V_P$ by 5-10% (Figure 6.4) [*Garnero and McNamara*, 2008]. The seismic features for the LLSVPs have been suggested to be due to the presence of warmer-than-average, Fe-enriched, and/or primordial materials, which are surrounded by subducted slabs with cooler-than-average temperature [*Garnero et al.*, 2016]. The LLSVPs, with reduced $V_S$ and negative values of bulk to shear seismic heterogeneity ratio $R_{\Phi/S}$ [*Garnero et al.*, 2016], differ from the seismic features of the PPv transition with an elevated $V_S$ and reduced $V_\Phi$ (Figure 6.4). Although remaining uncertain, it has been suggested that the existence of Fe-rich Bgm in the area can exhibit velocity-density profiles sufficiently to explain the seismic features of the LLSVPs [*Mao et al.*, 2011a].

ULVZs are 5-40 km thick regions geographically located at the edge of or outside of LLSVPs right above the CMB [*McNamara et al.*, 2010]. The origin of ULVZs has been suggested to be most likely due to the presence of partial melt [*Lay et al.*, 2004b] which can significantly reduce *Vs*, but the presence of Fe-rich PPv (40% of Fe in PPv (PPv40)) with significantly reduced $V_S$, $V_P$, and Poisson's ratio has also been proposed to account for ULVZ seismic features [*Mao et al.*, 2006]. However, it has been recently suggested that the sound velocities and Poisson's ratio of Fe-bearing PPv and Bgm can be lower than expected due to the presence of abnormal phonon mode contribution in the low-energy spectrum of the partial phonon density of states [*McCammon et al.*, 2016]. Comparison of our measured $V_P$ and *Vs* profiles of PPv15 and PPv25 in this study shows that PPv25 has a $V_P$ reduction of ~3.5% and $V_S$ reduction of ~1.5% compared to PPv15. If Bgm contains 10% of Fe (Bgm10) in the lower mantle [*Irifune et al.*, 2010], the $V_P$ decrease between Bgm10 and PPv40 is about ~10%, however, the $V_S$ drop is only ~4%. These changes cannot

be used to explain the large $V_S$ drop in ULVZs, indicating that the existence of very Fe-rich PPv alone is unlikely to explain large reduction of $V_S$ in the ULVZs (Figure 6.4).

Our present study provides first-order mineral physics evidence that explains seismic signatures in the D" with the occurrence of Fe-bearing PPv. The occurrence of the Bgm-PPv transition in the lowermost mantle is expected to be associated with an enhanced $V_S$ discontinuity, $V_S$ splitting anisotropy, anti-correlated $V_S$ and $V_\Phi$, and low Poisson's ratio. Due to possible Fe partitioning between Bgm and PPv as well as texturing in PPv, the $V_P$ discontinuity may not be as evident. The presence of very Fe-enriched PPv, on the other hand, is unlikely to be associated with the seismic features in the ULVZs. Future studies on the seismic profiles of Fe-bearing PPv with co-existing ferropericlase at elevated pressure-temperature conditions, together with information about their two-phase textures and single-crystal elasticity, are critically needed to be decipher detailed seismic features and realistic dynamic flow patterns at the lowermost mantle.

**Acknowledgements**

We acknowledge H.C. Watson for providing the glass starting material, V. Prakapenka for experimental assistance with the synthesis of the PPv samples and XRD experiments. We appreciate E. Garnero for constructive discussions. J.F. Lin acknowledges supports from the U.S. National Science Foundation Geophysics Program, Deep Carbon Observatory of the Sloan Foundation, and the Center for High Pressure Science and Technology Advanced Research (HPSTAR). We acknowledge GSECARS of the APS for use of the diffraction and laser heating facilities. This research utilized the resources of the Advanced Photon Source, a U.S. Department of Energy (DOE) Office of Science User Facility operated for the DOE Office of Science by Argonne National Laboratory under Contract No. DE-AC02-06CH11357. Data used in this study are available upon request to Jung-Fu Lin (Email: afu@jsg.utexas.edu).

# Appendix A

## Modelling the Fraction of the High-Spin and Low-Spin States in Ferropericlase

Following the modelling procedures reported in previous studies [*Mao et al.*, 2011b; *Tsuchiya et al.*, 2006; *Wentzcovitch et al.*, 2009], we have used the pressure-volume[*Tange et al.*] relations from our X-ray diffraction measurements to evaluate the fraction of the high-spin (HS) and low-spin (LS) states of iron in ferropericlase $(Mg_{0.92}Fe_{0.08})O$ as a function of pressure and temperature (*P*-*T*) (Figures 4.1 and 4.2). The *P*-*V* data of the ferropericlase was initially compared with the *P*-*V* relation of the end-member MgO as a starting reference at high pressures and room temperature [*Tange et al.*, 2009]. The comparison permits us to clearly evaluate the volume reduction over the pressure range across the spin transition [*Mao et al.*, 2011b]. Since the HS ferropericlase exhibits a similar equation of state (EoS) behavior to that of MgO, such comparison also helps establish the EoS parameters for the HS state [*Mao et al.*, 2011b]. With the width of the transition and the thermal EoS parameters of the HS state initially established, the fraction of the LS state ($n_{LS}$) at a given *P*-*T* condition can be obtained using the following equations [*Tsuchiya et al.*, 2006; *Wentzcovitch et al.*, 2009] (Figure 4.2):

$$n_{LS} = \frac{1}{1 + \exp\left(\frac{\Delta G(P,T)^*}{T}\right)} \quad [1]$$

$$\Delta G(P,T)^* = b_0(T) + b_1(T)P_n \quad [2]$$

$$P_n = \frac{P - P_{HS}}{P_{LS} - P_{HS}} \quad [3]$$

where $\Delta G(P,T)^*$ is the difference in the Gibbs free energy between the LS and HS states, $P_n$ is the normalized pressure as determined by the ending pressure of the HS state ($P_{HS}$) and the onset pressure of the LS state ($P_{LS}$), and $b_0$ and $b_1$ are two temperature-dependent constants. Using the non-linear least squares fit of the $n_{LS}$ to the *P*-*V* data at 300 K, we have obtained $b_0$ = 1220 (25) and $b_1$= −2341 (46).

Based on the solid-solution mixing of the HS and LS states in the ferropericlase lattice as well as the derived LS fraction ($n_{LS}$), the unit cell volume of ferropericlase ($V$) across the spin transition is expressed as the ratio between the unit cell volume of the HS state ($V_{HS}$) and the LS state ($V_{LS}$) at a given pressure and 300 K (Figure 4.2) [*Wentzcovitch et al.*, 2009]:

$$V = (1 - n_{LS})V_{HS} + nV_{LS} \quad [4]$$

It follows that the isothermal bulk modulus ($K_T$) of the system across the spin transition can be described using the ratio of the HS and LS states [*Wentzcovitch et al.*, 2009]:

$$\frac{V}{K_T} = n_{LS}\frac{V_{LS}}{K_{LS}} + (1 - n_{LS})\frac{V_{HS}}{K_{HS}} - (V_{LS} - V_{HS})\left(\frac{\partial n_{LS}}{\partial P}\right)_T \quad [5]$$

$$V_\emptyset = \sqrt{\frac{K_T}{\rho}} \quad [6]$$

where $K_{HS}$ and $K_{LS}$ are the $K_T$ of the HS and LS state, respectively, $\rho$ is the density, and $V_\Phi$ is the bulk sound velocity (Figures 4.2 and 4.3).

**Derivation of the Full Elastic Constants of the Single-Crystal Ferropericlase**

The ferropericlase platelet with the (100) orientation allows us to measure $V_P$ and $V_S$ velocities along principle [100] and [110] crystallographic axes using the BLS and ISS techniques in a DAC. Together with the *P*-*V* data from synchrotron X-ray diffraction measurements (Figures 4.1 and 4.2), here we have combined the $V_S$ data from BLS measurements and the $V_P$ data from ISS measurements (Figure 4.4) to derive the elastic constants ($C_{11}$, $C_{12}$, $C_{44}$) of the single-crystal ferropericlase using the following equations [*Every*, 1980] (Figure 4.5 and Figure A1):

$$V_P\,[100] = (C_{11}/\rho)^{1/2} \quad [7]$$

$$V_S\,[100] = (C_{44}/\rho)^{1/2} \quad [8]$$

$$V_P\,[110] = [(C_{11} + C_{12} + 2C_{44})/2\rho)^{1/2} \quad [9]$$

$$V_S\,[110] = [(C_{11} - C_{12})/2\rho)^{1/2} \quad [10]$$

where [*uvw*] represents the crystallographic direction for the acoustic wave propagation. Since the method for deriving the full elastic constants involves multiple experimental data sets and the use of multiple equations listed above, the elastic constants reported here are derived from internally-consistent numerical iterations through minimization of the uncertainties in the derived parameters using the aforementioned equations as well as the finite-strain equations discussed below [*Yang et al.*, 2014]. In finite-strain modelling, the pressure derivatives of $K_S$ and $G$ at a given temperature ($(\partial K_S/\partial P)_T$ and $(\partial G/\partial P)_T$ ) are obtained by fitting the moduli at high pressure using the third-order Eulerian finite-strain equation of state (EoS)[*Birch*, 1978]:

$$K_S = K_{S0}(1+2f)^{5/2}\{1+[3(\partial K_S/\partial P)_T - 5]f\} \quad [11]$$

$$G = (1+2f)^{5/2}\{G_0 + [3(\partial G/\partial P)_T K_{S0} - 5G_0]f\} \quad [12]$$

$$f = \left(\frac{1}{2}\right)[(V_0/V)^{\frac{2}{3}} - 1] \quad [13]$$

where $f$ is the Eulerian strain, and $V_0$ and $V$ are the unit-cell volumes at ambient conditions and high pressures, respectively. The derived $K_S$ and $(\partial K_S/\partial P)_T$ are converted to the isotherm bulk modulus ($K_T$) and its pressure derivative at constant temperature ($(\partial K_T/\partial P)_T$) using the following thermodynamic relations [*Poirier*, 2000]:

$$K_{T0} = K_{S0}/(1+\alpha\gamma T) \quad [14]$$

$$(\partial K_T/\partial P)_T = (1+\alpha\gamma T)^{-1}[\left(\frac{\partial K_S}{\partial P}\right)_T - (\frac{\gamma T}{K_{T0}})(\partial K_T/\partial T)_P] \quad [15]$$

where $(\partial K_T/\partial T)_P$ is the temperature derivative of the $K_T$ at constant pressure, $K_{T0}$ is the isothermal bulk modulus at ambient conditions, $\alpha$ is the thermal expansion coefficient, and $\gamma$ is the Grüneisen parameter. Literature values for these parameters ($(\partial K_T/\partial T)_P = -0.017$ GPa $K^{-1}$, $\alpha = 3.76\times10^{-5}$ $K^{-1}$, and $\gamma = 1.443$) are used for the conversion [*Mao et al.*, 2011b; *Tange et al.*, 2009]. The aforementioned procedures were iterated numerically until both $K_T$ and $(\partial K_T/\partial P)_T$ values were self-consistent with the input *P*-*V* relation. The derived $K_T$ and $(\partial K_T/\partial P)_T$ values were then used to construct the isothermal EoS of the ferropericlase at high *P*-*T*.

We have also followed procedure reported in the literature to model the $C_{ij}$ of ferropericlase across the spin transition as a function of pressure [*Wu et al.*, 2013]. Initially, the Eulerian finite-strain theory is applied to model the $C_{ij}$ of the HS state up to 40 GPa and

the LS state above 60 GPa, respectively, at ambient temperature. These elastic constants and their pressure derivatives for the HS and LS states are then used to evaluate the $C_{ij}$ of the mixed-spin (MS) state using the derived $n_{LS}$ and thermoelastic equations described below in which the elastic compliances, $S_{ij}$, at a given *P-T* condition are defined as [*Wu et al.*, 2013]:

$$S^{ij} = -\frac{1}{V}\frac{\partial^2 G}{\partial\sigma_i \partial\sigma_j}|_{P,T} \quad [16]$$

where $G$ is the total Gibbs free energy of the system, and $\sigma_i$ and $\sigma_j$ are the $i_{th}$ and $j_{th}$ stress components, respectively, in the Voigt notation. The elastic compliances for the cubic ferropericlase are given as [*Wu et al.*, 2013]:

$$S^{11}V = nS^{11}_{LS}V_{LS} + (1-n)S^{11}_{HS}V_{HS} - 1/9(V_{LS} - V_{HS})\frac{\partial n}{\partial P} \quad [17]$$

$$S^{12}V = nS^{12}_{LS}V_{LS} + (1-n)S^{12}_{HS}V_{HS} - 1/9(V_{LS} - V_{HS})\frac{\partial n}{\partial P} \quad [18]$$

$$S^{44}V = nS^{44}_{LS}V_{LS} + (1-n)S^{44}_{HS}V_{HS} \quad [19]$$

The relationships between the elastic constants and the compliances are described as:

$$C_{11} = \frac{S^{11} + S^{12}}{(S^{11})^2 + S^{11}S^{12} - 2(S^{12})^2} \quad [20]$$

$$C_{12} = \frac{-S^{12}}{(S^{11})^2 + S^{11}S^{12} - 2(S^{12})^2} \quad [21]$$

$$C_{44} = \frac{1}{S^{44}} \quad [22]$$

Comparison of the modelled elastic constants with experimental results shows consistent agreement with each other in the HS, MS, and LS states, confirming the

thermoelastic theory for the elasticity across the spin transition [*Wu et al.*, 2013] (Figure 4.5).

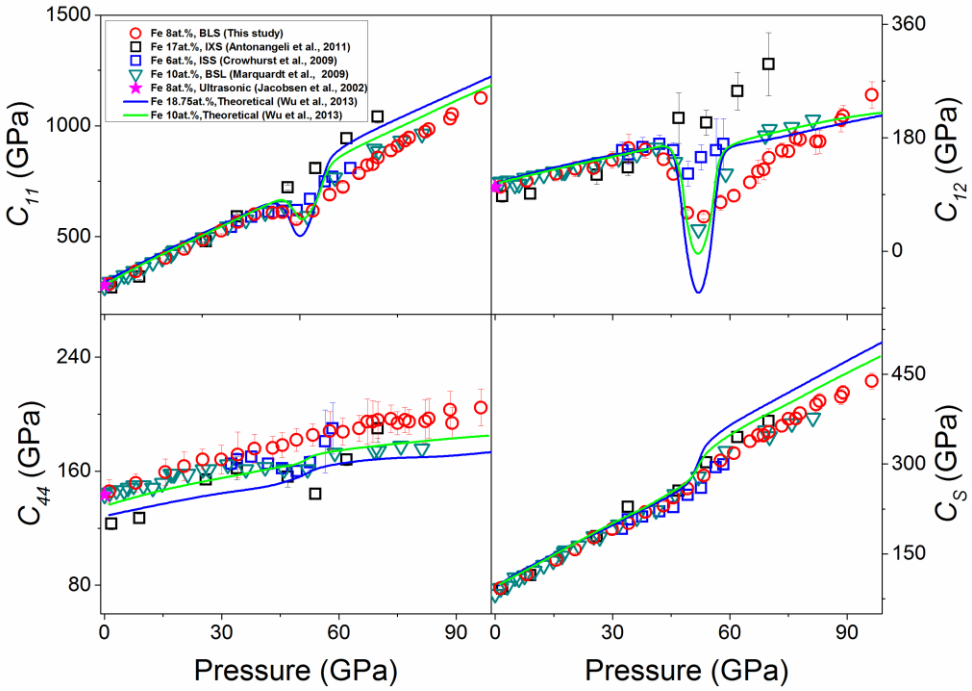


Figure A1: Comparison of the elastic constants of ferropericlase as a function of pressure. $C_S$ is defined as $(C_{11}–C_{12})/2$. Red circles: combined BLS and ISS measurements with 8% iron in this study; black squares: IXS study with 17% iron content [*Antonangeli et al.*, 2011]; green circles: BLS study below 20 GPa with 6% iron content [*Jackson et al.*, 2006]; blue triangles: ISS measurements with 6% iron [*Crowhurst et al.*, 2008]; dark cyan down triangles: BLS study with 10% iron [*Marquardt et al.*, 2009b]; magenta stars: ultrasonic measurements with 8% iron [*Jacobsen et al.*, 2002]; blue and green lines: theoretical results with 18.75% and 10% iron content, respectively [*Wu et al.*, 2013].

**Comparison of the Velocity Results at High Pressure**

Our measured $V_S$ values along [100] and [110] directions are mostly consistent with that in previous BLS measurements for ferropericlase with 10 at.% iron for the high-spin state [*Marquardt et al.*, 2009b], but are slightly higher within the spin transition and in the low-spin state (Figure A2). The difference within the spin transition can be explained as a result of different iron contents in these measurements as higher iron content is expected to contribute to a stronger effect on the velocity. Comparison of our measured $V_P$ with previous BLS measurements below 20 GPa shows great consistency within uncertainties [*Jackson et al.*, 2006], whereas there is a significant discrepancy within the spin transition and in the low-spin state (Figure A2). Our present results show a stronger softening within the spin transition and a lower velocity in the low spin state than that in the previous ISS measurements for ferropericlase with 6% iron. These differences may be explained by the different iron contents, pressure media, as well as experimental uncertainties including the orientation of the crystal used in the experiments.

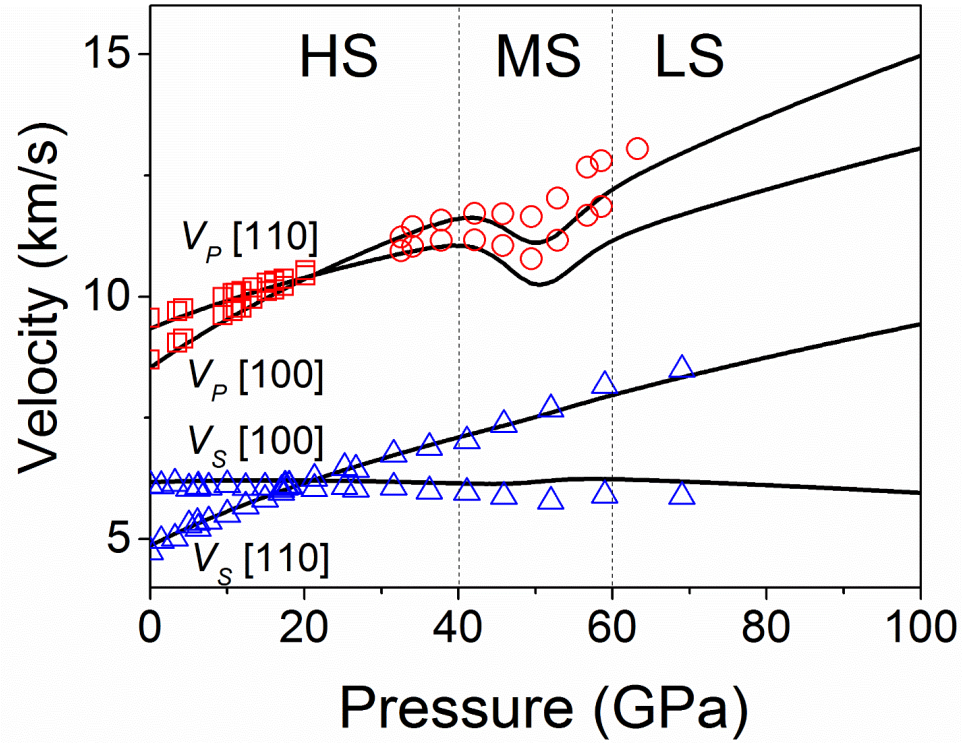


Figure A2: Comparison of our results with previously reported velocities of ferropericlase at high pressures. Solid lines are modelled experimental results in this study; red squares are BLS measurement for $X_{Fe}$ = 0.06 up to 20 GPa [*Jackson et al.*, 2006]; red circles are ISS measurement for $X_{Fe}$ = 0.06 up to 60 GPa [*Crowhurst et al.*, 2008]; blue triangles are BLS measurement for $X_{Fe}$ = 0.1 up to 70 GPa [*Marquardt et al.*, 2009b].

**Modelling Thermoelastic Parameters across the Spin Crossover in the Lower Mantle**

Using the experimentally-derived thermal EoS parameters and the elastic constants at high pressures and 300 K, we have further modelled the elasticity of ferropericlase ($(Mg_{0.92}Fe_{0.08})O$) at high *P*-*T* conditions relevant to the lower mantle along an expected geotherm [*Brown and Shankland*, 1981] (Figure 4.11 and Figure 4.10).

Literature results for the spin crossover of ferropericlase ($(Mg_{0.75}Fe_{0.25})O$) are used to construct the spin crossover diagram for our ferropericlase with 8 at.% iron. To reconstruct the spin crossover diagram for our sample, the spin transition pressure of 40-60 GPa at 300 K is used for our ferropericlase sample, instead of 50-75 GPa for ferropericlase with 25 at.% Fe content [*Mao et al.*, 2011b]. Based on previous studies [*Lin et al.*, 2007b; *Tsuchiya et al.*, 2006], elevated temperature widens the spin crossover toward higher pressures. Assuming the thermoelastic properties of ferropericlase can be scaled linearly as a function of the iron concentration, the parameters $b_0$ and $b_1$ in the equation (2) can be derived from the non-linear least squares fit to the derived $n_{LS}$ as a function of *P*-*T*:

$$b_0 = -262.5 + 4.9T - 3.0 \times 10^{-4}T^2 \quad [23]$$

$$b_1 = 3155.1 - 16.4T - 8.5 \times 10^{-4}T^2 \quad [24]$$

Together with the literature values for the thermal expansion coefficient of ferropericlase in the HS and LS state ($\alpha_{HS}$ and $\alpha_{LS}$) and the temperature derivative of the elastic constants [*Karki et al.*, 2001], we have used the modelled spin crossover diagram and the elastic compliances at high pressures and 300 K to calculate the elastic constants at high P-T using MATLAB (Figure 4.10 and Figure 4.11) [*Wu et al.*, 2013].

# Appendix B

**Modelling Velocity Profiles of Fe-bearing Bridgmanite and PPv at High Pressures**

The following procedure has been used to model the equation of state (EoS), compressional wave velocity ($V_P$) and shear wave velocity ($V_S$) of Fe-bearing Bgm at lowermost-mantle pressures to evaluate the velocity contrast between Fe-bearing Bgm and PPv across the phase boundary. Third-order Eulerian finite-strain equations (S1-S3) were used to derive the adiabatic bulk modulus $K_S$ and shear modulus $G$ at high pressure using reported adiabatic bulk and shear moduli at ambient conditions ($K_{S0}$ and $G_0$) [*Chantel et al.*, 2012; *Li and Zhang*, 2005]:

$$K_S = K_{S0}(1+2f)^{5/2}\{1+[3K_S' - 5]f\} \quad \text{S1)}$$

$$G = (1+2f)^{5/2}\{G_0 + [3G'K_{S0} - 5G_0]f\} \quad \text{S2)}$$

$$f = \left(\frac{1}{2}\right)[(\rho/\rho_0)^{\frac{2}{3}} - 1] \quad \text{S3)}$$

where $K_S'$ is the pressure derivative of the adiabatic bulk modulus, $G'$ is the pressure derivative of the shear modulus, and *f* is the Eulerian finite strain. The aggregate $V_P$ and $V_S$ can be calculated using the following equations (S4-S5) at each given pressure or density:

$$V_P = \sqrt{(4K_S/3 + G)G/\rho} \quad \text{S4)}$$

$$V_S = \sqrt{G/\rho} \quad \text{S5)}$$

Here high-pressure density of Bgm was calculated using the third-order Birch-Murnaghan EoS and previously reported EoS parameters obtained in previous X-ray

diffraction measurements [*Ballaran et al.*, 2012; *Chantel et al.*, 2012] (Equation S6) (Table B1):

$$P = 3K_{T0}[(\rho/\rho_0)^{7/3} - (\rho/\rho_0)^{5/3}]\{1 + {}^{3}/_{4}\,(K_T' - 4)[(\rho/\rho_0)^{2/3} - 1]\} \quad \text{S6)}$$

where $K_{T0}$ is the isothermal bulk modulus at ambient conditions, $K_T'$ is the pressure derivative of the isothermal bulk modulus, and $\rho_0$ is the density at ambient conditions. For the Fe-bearing Bgm, datasets for the aforementioned elasticity parameters [*Chantel et al.*, 2012] are limited to the bridgmanite with $MgSiO_3$ pure end-member and ($Mg_{0.95}Fe_{0.05}SiO_3$) with 5% Fe. Although elastic parameters of Bgm with 10% Fe and 10% Al are also available in a recent Brillouin study [*Kurnosov et al.*, 2017], the extrapolation of this set of data show significant velocity differences especially in $V_S$ when compared with that reported in Chantel et al., 2012 above 30 GPa (Figure B2). The differences may be due to the presence of $Fe^{3+}$ and/or $Al^{3+}$. Thus, this set of data for Fe, Al-bearing bridgmanite was not employed in any extrapolations in this study as our study here focuses on sound velocity profiles of Fe-bearing Bgm and PPv. We have used a linear extrapolation for the Fe substitution effects on the EoS and elastic parameters to obtain velocity profiles ($V_P$ and $V_S$) for Bgm15 and Bgm25 up to 120 GPa:

$$dV_{P.S}/dX_{Fe} = [V_{P,S}(bgm5) - V_{P.S}(bgm0)]/5 \quad \text{S7)}$$

$$V_{P,S}(P) = V_{P,S}(km/s) - dV_{P,S}/dX_{Fe} \times X_{Fe} \quad \text{S8)}$$

Uncertainties in these calculations are obtained through standard error propagations. The calculated compositional gradient of velocity $dV_P/dX_{Fe}$ and $dV_P/dX_{Fe}$ are ~−0.046 and −0.016 at ambient conditions, respectively, and are −0.039 and −0.038 at 120 GPa for Bgm. The estimated velocity differences between Bgm and PPv depend on the choice of the input thermoelastic parameters of Bgm for the modelling.

Although input data are rather limited, several iterations were performed based on the datasets reported (Table B1). All of the data used for the modelling consistently show an increased $V_S$ and decreased $V_P$ across the PPv phase transition when the velocities of Bgm and PPv are compared at 120 GPa. With the extrapolated data, we plotted the Bgm15 and PPv15 velocities as a function of density as shown in Figure B3. It shows that a drastic density increase across the Bgm and PPv transition is accompanied by $V_S$ increase as well as $V_P$ and $V_\Phi$ decrease.

Within the investigated pressure range, the $V_P$ and $V_S$ values as a function of pressure for PPv15 and PPv25 are linearly fitted to evaluate the velocity gradient at lowermost mantle pressures with a starting pressure chosen at 120 GPa (Figure 6.2, Table B1):

$$V_S^{PPv15} = 7.37(km/s) + 0.007 \times P(GPa) \quad \text{S9)}$$

$$V_P^{PPv15} = 13.55(km/s) + 0.011 \times P(GPa) \quad \text{S10)}$$

$$V_S^{PPv25} = 7.26(km/s) + 0.005 \times P(GPa) \quad \text{S11)}$$

$$V_P^{PPv25} = 13.07(km/s) + 0.014 \times P(GPa) \quad \text{S12)}$$

The pressure derivative for Bgm15 and Bgm25 is $dV_P/dP$ ~0.020 km·s$^{-1}$·GPa$^{-1}$ from 100 to 120 GPa, which is greater than that of the PPv15 and PPv25. The pressure derivative $dV_S/dP$ for Bgm15 and Bgm25 is slightly less than the PPv15 and PPv25 (Table 6.2).

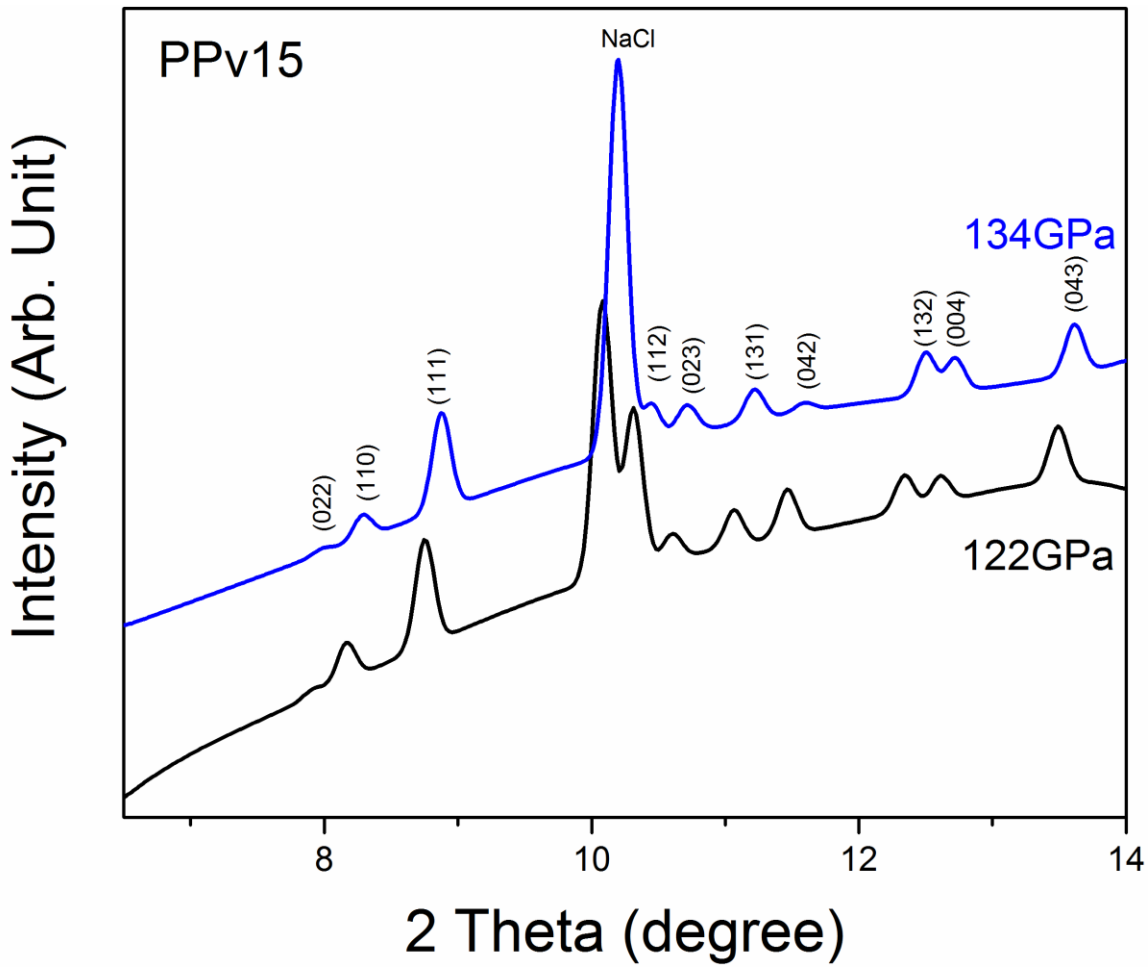


Figure B1: Representative X-ray diffraction patterns of PPv15 at 122 GPa and 134 GPa. NaCl was used as the pressure medium and calibrant. Incident X-ray wavelength was 0.3344 Å. X-ray diffraction patterns were taken at 13IDD beamline of the GSECARS using MAR CCD detector.

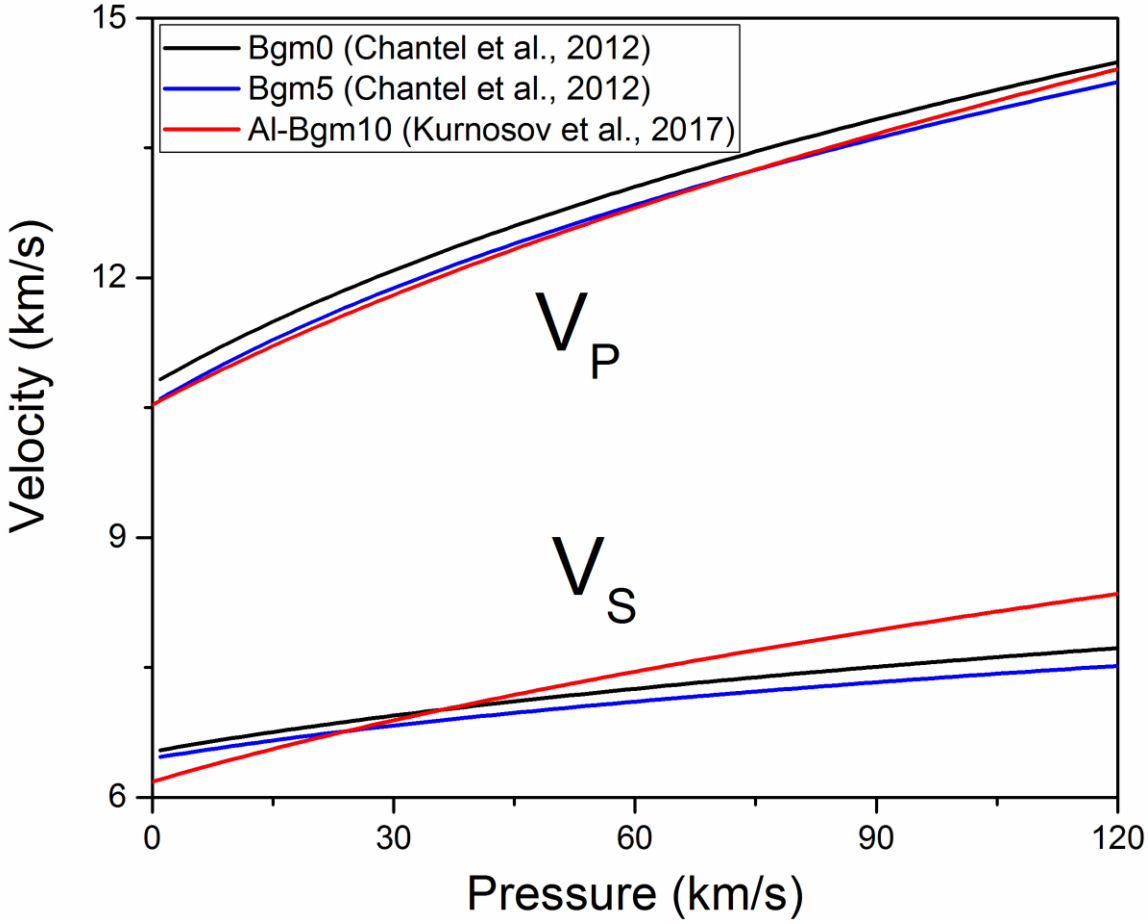


Figure B2: Extrapolations of sound velocities of bridgmanite using reported thermoelastic properties [*Chantel et al.*, 2012; *Kurnosov et al.*, 2017] of pure end member (Bgm0), 5% of Fe bridgmanite (Bgm5) and 10% of Fe with 10% of Al (Al-Bgm). The Al-bearing Bgm *Vs* profile is very different from Fe-bearing counterpart and is not used in our modelling.

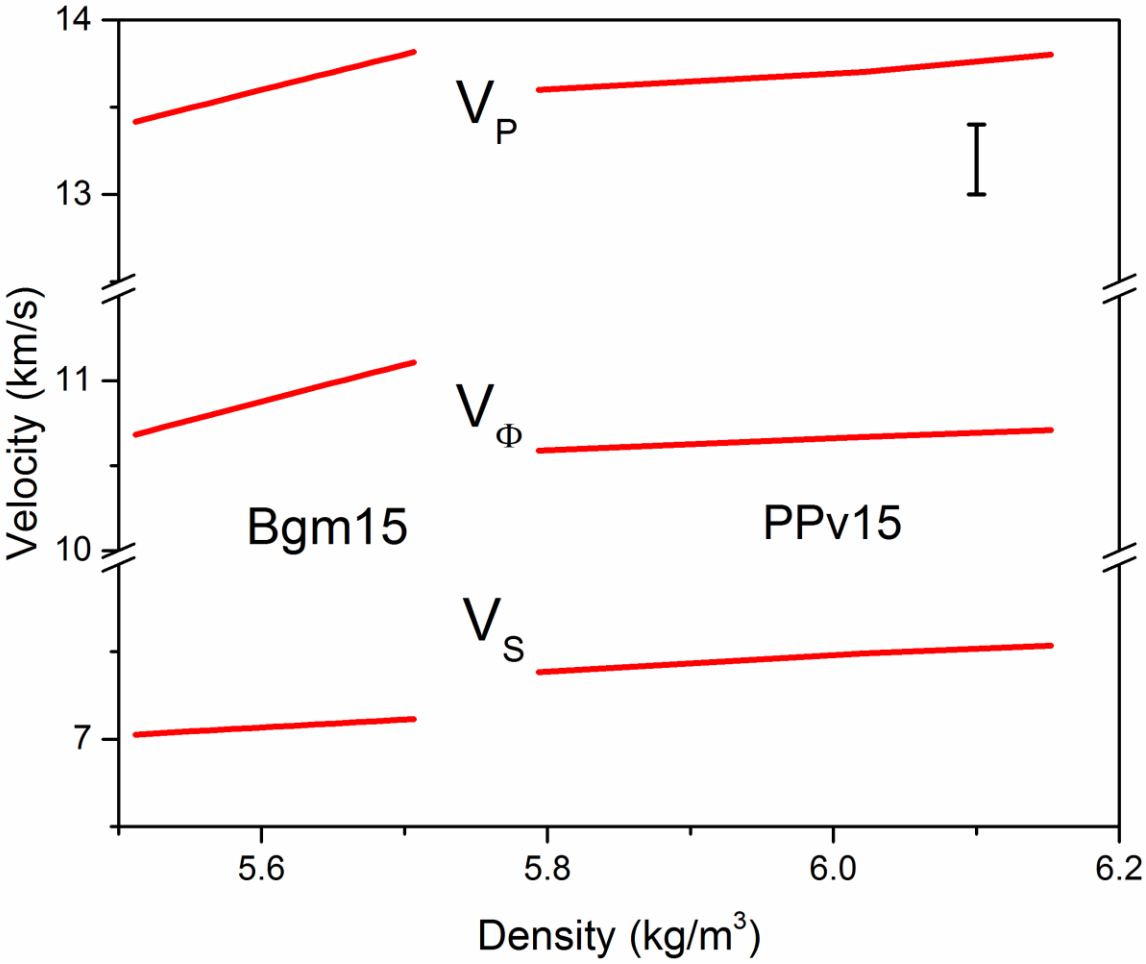


Figure B3: Velocity profiles of Fe-bearing PPv (PPv15) and Bgm as a function of density at lowermost mantle pressures.

Table B1: Elastic properties of bridgmanite at high pressures. These values were used in the modelling of the sound velocities of Fe-bearing bridgmanite.

| | $MgSiO_3$ (bmg0) | | $(Mg_{0.95},Fe_{0.05})SiO_3$ (bgm5) | |
|---|---|---|---|---|
| $K_{S0}$ (GPa) | 247(4)[a] | 252(1)[b] | 236(2)[a] | 236(2)[a] |
| $K_S'$ | 4.5(2)[a] | 4.1(1)[b] | 4.7(1)[a] | 4.7(1)[a] |
| $G_0$ (GPa) | 176(2)[a] | 175(1)[b] | 174(1)[a] | 174(1)[a] |
| $G'$ | 1.6(1)[a] | 1.7(1)[b] | 1.56(5)[a] | 1.56(5)[a] |
| $\rho_0$(g/cm$^3$) | 4.11[a] | 4.11[b] | 4.16[a] | 4.15[c] |
| $K_{T0}$ | 257(2)[a] | 251(2)[c] | 246(2)[a] | 253(2)[c] |
| $K_T'$ | 4(fixed)[a] | 4.11(7)[c] | 4(fixed)[a] | 3.99(7)[c] |

[a]Results from ultrasonic measurements and X-ray diffraction measurements from Chantel et al. 2012

[b]Results were obtained by combining the data in Chantel et al, 2012 and low-pressure data in Li and Zhang, 2005.

[c]Results data from XRD measurements in Boffa Ballaran et al., 2012

## References


Antonangeli, D., J. Siebert, C. M. Aracne, D. L. Farber, A. Bosak, M. Hoesch, M. Krisch, F. J. Ryerson, G. Fiquet, and J. Badro (2011), Spin crossover in ferropericlase at high pressure: A seismologically transparent transition?, *Science*, *331*(6013), 64.

Auzende, A. L., J. Badro, F. J. Ryerson, P. K. Weber, S. J. Fallon, A. Addad, J. Siebert, and G. Fiquet (2008), Element partitioning between magnesium silicate perovskite and ferropericlase: new insights into bulk lower-mantle geochemistry, *Earth Planet. Sci. Lett.*, *269*(1-2), 164-174.

Badro, J., G. Fiquet, F. Guyot, J.-P. Rueff, V. V. Struzhkin, G. Vankó, and G. Monaco (2003), Iron partitioning in Earth's mantle: toward a deep lower mantle discontinuity, *Science*, *300*(5620), 789-791.

Badro, J., J.-P. Rueff, G. Vankó, G. Monaco, G. Fiquet, and F. Guyot (2004), Electronic transitions in perovskite: Possible nonconvecting layers in the lower mantle, *Science*, *305*(5682), 383-386.

Ballaran, T. B., A. Kurnosov, K. Glazyrin, D. J. Frost, M. Merlini, M. Hanfland, and R. Caracas (2012), Effect of chemistry on the compressibility of silicate perovskite in the lower mantle, *Earth Planet. Sci. Lett.*, *333*, 181-190.

Bass, J. D. (2007), 2.10 - Theory and Practice – Techniques for Measuring High P/T Elasticity A2 - Schubert, Gerald, in Treatise on Geophysics, edited, pp. 269-291, Elsevier, Amsterdam.

Birch, F. (1947), Finite elastic strain of cubic crystals, *Phys. Rev.*, *71*(11), 809.

Birch, F. (1978), Finite strain isotherm and velocities for single-crystal and polycrystalline NaCl at high pressures and 300 K, *J. Geophys. Res.*, *83*(B3), 1257-1268.

Brillouin, L. (1922), Diffusion of Light and X-rays by a Transparent Homogeneous Body, *Ann. Phys.(Paris)*, *17*, 88.

Brown, J., and T. Shankland (1981), Thermodynamic parameters in the Earth as determined from seismic profiles, *Geophys. J. Roy. Astron. Soc.*, *66*(3), 579-596.

Burke, K., B. Steinberger, T. H. Torsvik, and M. A. Smethurst (2008), Plume generation zones at the margins of large low shear velocity provinces on the core–mantle boundary, *Earth Planet. Sci. Lett.*, *265*(1), 49-60.

Cammarano, F., H. Marquardt, S. Speziale, and P. J. Tackley (2010), Role of iron-spin transition in ferropericlase on seismic interpretation: A broad

thermochemical transition in the mid mantle?, *Geophys. Res. Lett.*, *37*(3), L03308.
Caracas, R., and R. Cohen (2005), Effect of chemistry on the stability and elasticity of the perovskite and post-perovskite phases in the $MgSiO_3$-$FeSiO_3$-$Al_2O_3$ system and implications for the lowermost mantle, *Geophys. Res. Lett.*, *32*(16).
Chaloner, J. W., C. Thomas, and A. Rietbrock (2009b), P-and S-wave reflectors in D″ beneath southeast Asia, *Geophys. J. Int.*, *179*(2), 1080-1092.
Chambers, K., and J. Woodhouse (2006), Transient D″ discontinuity revealed by seismic migration, *Geophys. Res. Lett*, *33*(17).
Chantel, J., D. J. Frost, C. A. McCammon, Z. Jing, and Y. Wang (2012), Acoustic velocities of pure and iron-bearing magnesium silicate perovskite measured to 25 GPa and 1200 K, *Geophys. Res. Lett.*, *39*(19).
Cobden, L., C. Thomas, and J. Trampert (2015), Seismic detection of post-perovskite inside the Earth, in *The Earth's Heterogeneous Mantle*, edited, pp. 391-440, Springer.
Crowhurst, J., J. Brown, A. Goncharov, and S. Jacobsen (2008), Elasticity of (Mg,Fe)O through the spin transition of iron in the lower mantle, *Science*, *319*(5862), 451.
Davies, D., S. Goes, and H. Lau (2015), Thermally dominated deep mantle LLSVPs: a review, in *The Earth's Heterogeneous Mantle*, edited by F. D. Amir Khan, pp. 441-477, Springer, New York.
Dias, R. P., and I. F. Silvera (2017), Observation of the Wigner-Huntington transition to metallic hydrogen, *Science*, *355*(6326), 715-718.
Ding, X., and D. V. Helmberger (1997), Modelling D″ structure beneath Central America with broadband seismic data, *Phys. Earth Planet. Inter.*, *101*(3), 245-270.
Dubrovinsky, L., N. Dubrovinskaia, V. B. Prakapenka, and A. M. Abakumov (2012), Implementation of micro-ball nanodiamond anvils for high-pressure studies above 6 Mbar, *Nat. commun. 3*, 1163.
Dziewonski, A. M., and D. L. Anderson (1981), Preliminary reference Earth model, *Phys. Earth Planet. Inter.*, *25*(4), 297-356.
Every, A. (1980), General closed-form expressions for acoustic waves in elastically anisotropic solids, *Phys. Rev. B*, *22*(4), 1746.

Fei, Y., A. Ricolleau, M. Frank, K. Mibe, G. Shen, and V. Prakapenka (2007a), Toward an internally consistent pressure scale, *Proc. Natl. Acad. Sci. USA*, *104*(22), 9182-9186.
Fei, Y., L. Zhang, A. Corgne, H. Watson, A. Ricolleau, Y. Meng, and V. Prakapenka (2007b), Spin transition and equations of state of (Mg, Fe)O solid solutions, *Geophys. Res. Lett.*, *34*(17), L17307.
Forte, A. M. (2000), Seismic-Geodynamic Constraints on Mantle Flow: Implications for Layered Convection, Mantle Viscosity, and Seismic Anisotropy in the Deep Mantle, *Earth's Deep Interior: Mineral Physics and Tomography from the Atomic to the Global Scale*, 3-36.
Forte, A. M., R. L. Woodward, and A. M. Dziewonski (1994), Joint inversions of seismic and geodynamic data for models of three-dimensional mantle heterogeneity, *J. Geophys. Res. Solild Earth*, *99*(B11), 21857-21877.
Frost, D. J., C. Liebske, F. Langenhorst, C. A. McCammon, R. G. Trønnes, and D. C. Rubie (2004), Experimental evidence for the existence of iron-rich metal in the Earth's lower mantle, *Nature*, *428*(6981), 409-412.
Fu, S., J. Yang, and J.-F. Lin (2017), Abnormal Elasticity of Single-Crystal Magnesiosiderite across the Spin Transition in Earth's Lower Mantle, *Phys. Rev. Lett.*, *118*(3), 036402.
Fukui, H., et al. (2016), Effect of cation substitution on bridgmanite elasticity: A key to interpret seismic anomalies in the lower mantle, *Sci. Rep.*, *6*, 33337.
Garnero, E. J., and A. K. McNamara (2008), Structure and dynamics of Earth's lower mantle, *science*, *320*(5876), 626-628.
Garnero, E. J., A. K. McNamara, and S.-H. Shim (2016), Continent-sized anomalous zones with low seismic velocity at the base of Earth's mantle, *Nature Geosci*, *9*(7), 481-489.
Gassner, A., C. Thomas, F. Krüger, and M. Weber (2015), Probing the core–mantle boundary beneath Europe and Western Eurasia: A detailed study using PcP, *Phys. Earth Planet. Inter.*, *246*, 9-24.
Grocholski, B., K. Catalli, S.-H. Shim, and V. Prakapenka (2012), Mineralogical effects on the detectability of the postperovskite boundary, *Proc. Natl. Acad. Sci. USA*, *109*(7), 2275-2279.
Hager, B. H., R. W. Clayton, M. A. Richards, R. P. Comer, and A. M. Dziewonski (1984), Lower mantle heterogeneity, dynamic topography and the geoid, *Nature*, *313*(14).
Hill, R. (1952), The elastic behaviour of a crystalline aggregate, *Proc. Phys. Soc., Sect. A.*, *65*, 349.

Hirose, K., Y. Fei, Y. Ma, and H.-K. Mao (1999), The fate of subducted basaltic crust in the Earth's lower mantle, *Nature*, *397*(6714), 53-56.

Hirose, K., R. Sinmyo, N. Sata, and Y. Ohishi (2006), Determination of post‐perovskite phase transition boundary in $MgSiO_3$ using Au and MgO pressure standards, *Geophys. Res. Lett.*, *33*(1).

Hirose, K., N. Takafuji, K. Fujino, S. R. Shieh, and T. S. Duffy (2008), Letter. Iron partitioning between perovskite and post-perovskite: A transmission electron microscope study, *Am. Mineral.*, *93*(10), 1678-1681.

Hirose, K., N. Takafuji, N. Sata, and Y. Ohishi (2005), Phase transition and density of subducted MORB crust in the lower mantle, *Earth Planet. Sci. Lett.*, *237*(1–2), 239-251.

Houser, C., G. Masters, P. Shearer, and G. Laske (2008), Shear and compressional velocity models of the mantle from cluster analysis of long-period waveforms, *Geophys. J. Int.*, *174*(1), 195-212.

Huang, C., W. Leng, and Z. Wu (2015), Iron-spin transition controls structure and stability of LLSVPs in the lower mantle, *Earth Planet. Sci. Lett.*, *423*, 173-181.

Hummer, D. R., and Y. Fei (2012), Synthesis and crystal chemistry of $Fe^{3+}$-bearing $(Mg, Fe^{3+})(Si, Fe^{3+})O_3$ perovskite, *Am. Mineral.*, *97*(11), 1915.

Hutko, A. R., T. Lay, J. Revenaugh, and E. J. Garnero (2008), Anticorrelated seismic velocity anomalies from post-perovskite in the lowermost mantle, *Science*, *320*(5879), 1070-1074.

Iitaka, T., K. Hirose, K. Kawamura, and M. Murakami (2004), The elasticity of the $MgSiO_3$ post-perovskite phase in the Earth's lowermost mantle, *Nature*, *430*(6998), 442-445.

Irifune, T. (1994), Absence of an aluminous phase in the upper part of the Earth's lower mantle, *Nature*, *370*, 131-133

Irifune, T., T. Shinmei, C. A. McCammon, N. Miyajima, D. C. Rubie, and D. J. Frost (2010), Iron partitioning and density changes of pyrolite in Earth's lower mantle, *Science*, *327*(5962), 193-195.

Ishii, M., and J. Tromp (2004), Constraining large-scale mantle heterogeneity using mantle and inner-core sensitive normal modes, *Phys. Earth Planet. Inter.*, *146*(1), 113-124.

Jackson, J. M., S. V. Sinogeikin, S. D. Jacobsen, H. J. Reichmann, S. J. Mackwell, and J. D. Bass (2006), Single-crystal elasticity and sound velocities of $(Mg_{0.94}Fe_{0.06})$ O ferropericlase to 20 GPa, *J. Geophys. Res.*, *111*.

Jackson, J. M., J. Zhang, J. Shu, S. V. Sinogeikin, and J. D. Bass (2005), High-pressure sound velocities and elasticity of aluminous $MgSiO_3$ perovskite to 45 GPa: implications for lateral heterogeneity in Earth's lower mantle, *Geophys. Res. Lett.*, *32*(21), L21305.

Jacobsen, S. D., H.-J. Reichmann, H. A. Spetzler, S. J. Mackwell, J. R. Smyth, R. J. Angel, and C. A. McCammon (2002), Structure and elasticity of single-crystal (Mg,Fe)O and a new method of generating shear waves for gigahertz ultrasonic interferometry, *J. Geophys. Res.*, *107*(B2), 2037.

Jacobsen, S. D., H. Spetzler, H. J. Reichmann, and J. R. Smyth (2004), Shear waves in the diamond-anvil cell reveal pressure-induced instability in (Mg, Fe)O, *Proc. Nat. Acad. Sci. U.S.A.*, *101*(16), 5867-5871.

Kaneshima, S., and G. Helffrich (1999), Dipping low-velocity layer in the mid-lower mantle: evidence for geochemical heterogeneity, *Science*, *283*(5409), 1888-1892.

Kaneshima, S., and G. Helffrich (2010), Small scale heterogeneity in the mid-lower mantle beneath the circum-Pacific area, *Phys. Earth Planet. Inter.*, *183*(1), 91-103.

Kantor, I., V. Prakapenka, A. Kantor, P. Dera, A. Kurnosov, S. Sinogeikin, N. Dubrovinskaia, and L. Dubrovinsky (2012), BX90: A new diamond anvil cell design for X-ray diffraction and optical measurements, *Rev. Sci. Instrum.*, *83*(12), 125102-125102-125106.

Karato, S. i. (1993), Importance of anelasticity in the interpretation of seismic tomography, *Geophys. Res. Lett.*, *20*(15), 1623-1626.

Karato, S. i., and B. B. Karki (2001), Origin of lateral variation of seismic wave velocities and density in the deep mantle, *J. Geophys. Res. Solild Earth*, *106*(B10), 21771-21783.

Karki, B., R. Wentzcovitch, S. De Gironcoli, and S. Baroni (1999), First-principles determination of elastic anisotropy and wave velocities of MgO at lower mantle conditions, *Science*, *286*(5445), 1705-1707.

Karki, B. B., L. Stixrude, S. J. Clark, M. C. Warren, G. J. Ackland, and J. Crain (1997), Elastic properties of orthorhombic $MgSiO_3$ perovskite at lower mantle pressures, *Am. Mineral.*, *82*(5), 635-638.

Karki, B. B., L. Stixrude, and R. M. Wentzcovitch (2001), High-pressure elastic properties of major materials of Earth’s mantle from first principles, *Rev. Geophys.*, *39*(4), 507–534.

Kellogg, L. H., B. H. Hager, and R. D. van der Hilst (1999), Compositional stratification in the deep mantle, *Science*, *283*(5409), 1881-1884.

Kendall, J., and C. Nangini (1996), Lateral variations in D" below the Caribbean, *Geophys. Res. Lett.*, *23*(4), 399-402.
Kennett, B., E. Engdahl, and R. Buland (1995), Constraints on seismic velocities in the Earth from traveltimes, *Geophys. J. Int.*, *122*(1), 108-124.
Kito, T., S. Rost, C. Thomas, and E. J. Garnero (2007), New insights into the P-and S-wave velocity structure of the D″ discontinuity beneath the Cocos plate, *Geophys. J. Int.*, *169*(2), 631-645.
Klotz, S., J. Chervin, P. Munsch, and G. Le Marchand (2009), Hydrostatic limits of 11 pressure transmitting media, *Journal of Physics D: Applied Physics*, *42*(7), 075413.
Kobayashi, Y., T. Kondo, E. Ohtani, N. Hirao, N. Miyajima, T. Yagi, T. Nagase, and T. Kikegawa (2005), Fe‐Mg partitioning between (Mg, Fe)$SiO_3$ post‐perovskite, perovskite, and magnesiowüstite in the Earth's lower mantle, *Geophys. Res. Lett.*, *32*(19).
Koelemeijer, P., J. Ritsema, A. Deuss, and H.-J. van Heijst (2016), SP12RTS: a degree-12 model of shear-and compressional-wave velocity for Earth's mantle, *Geophys. J. Int.*, *204*(2), 1024-1039.
Kurnosov, A., H. Marquardt, D. Frost, T. B. Ballaran, and L. Ziberna (2017), Evidence for a $Fe^{3+}$-rich pyrolitic lower mantle from (Al, Fe)-bearing bridgmanite elasticity data, *Nature*.
Labrosse, S., J. Hernlund, and N. Coltice (2007), A crystallizing dense magma ocean at the base of the Earth's mantle, *Nature*, *450*(7171), 866-869.
Lay, T., E. Garnero, and S. Russell (2004a), Lateral variation of the D″ discontinuity beneath the Cocos Plate, *Geophys. Res. Lett.*, *31*(15).
Lay, T., E. J. Garnero, and Q. Williams (2004b), Partial melting in a thermo-chemical boundary layer at the base of the mantle, *Phys. Earth Planet. Inter.*, *146*(3), 441-467.
Lay, T., and D. V. Helmberger (1983), A lower mantle S-wave triplication and the shear velocity structure of D″ ,*Geophys. J. Int.*, *75*(3), 799-837.
Lay, T., J. Hernlund, E. J. Garnero, and M. S. Thorne (2006), A post-perovskite lens and D" heat flux beneath the central Pacific, *science*, *314*(5803), 1272-1276.
Lay, T., Q. Williams, E. J. Garnero, L. Kellogg, and M. E. Wysession (1998), Seismic wave anisotropy in the D″ region and its implications, *The core-mantle boundary region*, 299-318.

Lee, C.-T. A., P. Luffi, T. Höink, J. Li, R. Dasgupta, and J. Hernlund (2010), Upside-down differentiation and generation of a 'primordial' lower mantle, *Nature*, *463*(7283), 930-933.

Li, B., and J. Zhang (2005), Pressure and temperature dependence of elastic wave velocity of $MgSiO_3$ perovskite and the composition of the lower mantle, *Phys. Earth Planet. Inter.*, *151*(1–2), 143-154.

Li, L., J. P. Brodholt, S. Stackhouse, D. J. Weidner, M. Alfredsson, and G. D. Price (2005), Elasticity of (Mg, Fe)(Si, Al)$O_3$-perovskite at high pressure, *Earth Planet. Sci. Lett.*, *240*(2), 529-536.

Lin, J.-F., S. Speziale, Z. Mao, and H. Marquardt (2013), Effects of the electronic spin transitions of iron in lower mantle minerals: implications for deep mantle geophysics and geochemistry, *Rev. Geophys.*, *51*(2), 244-275.

Lin, J., S. T. Weir, D. D. Jackson, W. J. Evans, Y. K. Vohra, W. Qiu, and C. Yoo (2007a), Electrical conductivity of the lower-mantle ferropericlase across the electronic spin transition, *Geophys. Res. Lett.*, *34*(16), 16305.

Lin, J. F., Z. Mao, J. Yang, J. Liu, Y. Xiao, P. Chow, and T. Okuchi (2016), High-spin $Fe^{2+}$ and $Fe^{3+}$ in single-crystal aluminous bridgmanite in the lower mantle, *Geophys. Res. Lett.*, *43*(13), 6952-6959.

Lin, J. F., V. V. Struzhkin, S. D. Jacobsen, M. Y. Hu, P. Chow, J. Kung, H. Liu, H. Mao, and R. J. Hemley (2005), Spin transition of iron in magnesiowüstite in the Earth's lower mantle, *Nature*, *436*(7049), 377-380.

Lin, J. F., G. Vankó, S. D. Jacobsen, V. Iota, V. V. Struzhkin, V. B. Prakapenka, A. Kuznetsov, and C. S. Yoo (2007b), Spin transition zone in Earth's lower mantle, *Science*, *317*(5845), 1740.

Lin, J. F., S. T. Weir, D. D. Jackson, W. J. Evans, Y. K. Vohra, W. Qiu, and C. S. Yoo (2007c), Electrical conductivity of the lower-mantle ferropericlase across the electronic spin transition, *Geophys. Res. Lett.*, *34*(16).

Lu, C., Z. Mao, J. F. Lin, K. K. Zhuravlev, S. N. Tkachev, and V. B. Prakapenka (2013), Elasticity of single-crystal iron-bearing pyrope up to 20 GPa and 750K, *Earth Planet. Sci. Lett.*, *361*, 134-142.

Mainprice, D., G. Barruol, and W. B. Ismail (2000), The seismic anisotropy of the Earth's mantle: from single crystal to polycrystal, *Geophysical Monograph, American Geophysical Union*, *117*, 237-264.

Mao, H., J.-A. Xu, and P. Bell (1986), Calibration of the ruby pressure gauge to 800 kbar under quasi-hydrostatic conditions, *J. Geophys. Res. Solild Earth*, *91*(B5), 4673-4676.

Mao, W. L., H.-k. Mao, W. Sturhahn, J. Zhao, V. B. Prakapenka, Y. Meng, J. Shu, Y. Fei, and R. J. Hemley (2006), Iron-rich post-perovskite and the origin of ultralow-velocity zones, *Science*, *312*(5773), 564-565.

Mao, Z. (2009), Single-crystal elasticity of hydrous mantle minerals, Princeton University.

Mao, Z., D. Fan, J.-F. Lin, J. Yang, S. N. Tkachev, K. Zhuravlev, and V. B. Prakapenka (2015), Elasticity of single-crystal olivine at high pressures and temperatures, *Earth Planet. Sci. Lett.*, *426*, 204-215.

Mao, Z., J.-F. Lin, J. Yang, H. Bian, J. Liu, H. C. Watson, S. Huang, J. Chen, V. B. Prakapenka, and Y. Xiao (2014a), (Fe, Al)-bearing post-perovskite in the Earth's lower mantle, *Earth Planet. Sci. Lett.*, *403*, 157-165.

Mao, Z., J.-F. Lin, J. Yang, J. Wu, H. C. Watson, Y. Xiao, P. Chow, and J. Zhao (2014b), Spin and valence states of iron in Al-bearing silicate glass at high pressures studied by synchrotron Mössbauer and X-ray emission spectroscopy, *Am. Mineral.*, *99*(2-3), 415-423.

Mao, Z., J. Lin, C. Jacobs, H. Watson, Y. Xiao, P. Chow, E. Alp, and V. Prakapenka (2010), Electronic spin and valence states of Fe in $CaIrO_3$-type silicate post-perovskite in the Earth's lowermost mantle, *Geophys. Res. Lett.*, *37*, L22304.

Mao, Z., J. Lin, H. Scott, H. Watson, V. Prakapenka, Y. Xiao, P. Chow, and C. McCammon (2011a), Iron-rich perovskite in the Earth's lower mantle, *Earth Planet. Sci. Lett.*, *309*(3-4), 179-184.

Mao, Z., J. F. Lin, J. Liu, and V. B. Prakapenka (2011b), Thermal equation of state of lower-mantle ferropericlase across the spin crossover, *Geophys. Res. Lett.*, *38*(23), L23308.

Mao, Z., F. Wang, J.-F. Lin, S. Fu, J. Yang, X. Wu, T. Okuchi, N. Tomioka, V. B. Prakapenka, and Y. Xiao (2017), Equation of state and hyperfine parameters of high-spin bridgmanite in the Earth's lower mantle by synchrotron X-ray diffraction and Mössbauer spectroscopy, *Am. Mineral.*, *102*(2), 357-368.

Marquardt, H., S. Speziale, H. J. Reichmann, D. J. Frost, and F. R. Schilling (2009a), Single-crystal elasticity of $(Mg_{0.9}Fe_{0.1})$ O to 81 GPa, *Earth Planet. Sci. Lett.*, *287*(3-4), 345-352.

Marquardt, H., S. Speziale, H. J. Reichmann, D. J. Frost, F. R. Schilling, and E. J. Garnero (2009b), Elastic shear anisotropy of ferropericlase in Earth's lower mantle, *Science*, *324*(5924), 224.

Masters, G., G. Laske, H. Bolton, and A. Dziewonski (2000), The relative behavior of shear velocity, bulk sound speed, and compressional velocity in the

mantle: implications for chemical and thermal structure, *Earth's deep interior: mineral physics and tomography from the atomic to the global scale*, 63-87.

Matas, J., J. Bass, Y. Ricard, E. Mattern, and M. Bukowinski (2007), On the bulk composition of the lower mantle: predictions and limitations from generalized inversion of radial seismic profiles, *Geophys. J. Int.*, *170*(2), 764-780.

Matas, J., and M. S. Bukowinski (2007), On the anelastic contribution to the temperature dependence of lower mantle seismic velocities, *Earth Planet. Sci. Lett.*, *259*(1), 51-65.

Matzel, E., M. K. Sen, and S. P. Grand (1996), Evidence for anisotropy in the deep mantle beneath Alaska, *Geophys. Res. Lett.*, *23*(18), 2417-2420.

McCammon, C., R. Caracas, K. Glazyrin, V. Potapkin, A. Kantor, R. Sinmyo, C. Prescher, I. Kupenko, A. Chumakov, and L. Dubrovinsky (2016), Sound velocities of bridgmanite from density of states determined by nuclear inelastic scattering and first-principles calculations, *Progress in Earth and Planetary Science*, *3*(1), 10.

McCammon, C., I. Kantor, O. Narygina, J. Rouquette, U. Ponkratz, I. Sergueev, M. Mezouar, V. Prakapenka, and L. Dubrovinsky (2008), Stable intermediate-spin ferrous iron in lower-mantle perovskite, *Nature Geosci*, *1*(10), 684-687.

McNamara, A. K., E. J. Garnero, and S. Rost (2010), Tracking deep mantle reservoirs with ultra-low velocity zones, *Earth Planet. Sci. Lett.*, *299*(1), 1-9.

Miyagi, L., and H.-R. Wenk (2016), Texture development and slip systems in bridgmanite and bridgmanite+ ferropericlase aggregates, *Phys. Chem. Minerals*, *43*(8), 597-613.

Mosca, I., L. Cobden, A. Deuss, J. Ritsema, and J. Trampert (2012), Seismic and mineralogical structures of the lower mantle from probabilistic tomography, *J. Geophys. Res. Solild Earth*, *117*(B6).

Muir, J. M. R., and J. P. Brodholt (2016), Ferrous iron partitioning in the lower mantle, *Phys. Earth Planet. Inter.*, *257*, 12-17.

Murakami, M., K. Hirose, K. Kawamura, N. Sata, and Y. Ohishi (2004), Post-perovskite phase transition in $MgSiO_3$, *Science*, *304*(5672), 855.

Murakami, M., Y. Ohishi, N. Hirao, and K. Hirose (2012), A perovskitic lower mantle inferred from high-pressure, high-temperature sound velocity data, *Nature*, *485*(7396), 90-94.

Murakami, M., S. V. Sinogeikin, H. Hellwig, J. D. Bass, and J. Li (2007), Sound velocity of $MgSiO_3$ perovskite to Mbar pressure, *Earth Planet. Sci. Lett.*, *256*(1-2), 47-54.

Oganov, A. R., and S. Ono (2004), Theoretical and experimental evidence for a post-perovskite phase of $MgSiO_3$ in Earth's D″ layer, *Nature*, *430*(6998), 445-448.

Okuchi, T., N. Purevjav, N. Tomioka, J.-F. Lin, T. Kuribayashi, L. Schoneveld, H. Hwang, N. Sakamoto, N. Kawasaki, and H. Yurimoto (2015), Synthesis of large and homogeneous single crystals of water-bearing minerals by slow cooling at deep-mantle pressures, *Am. Mineral.*, *100*(7), 1483-1492.

Ono, S., E. Ito, and T. Katsura (2001), Mineralogy of subducted basaltic crust (MORB) from 25 to 37 GPa, and chemical heterogeneity of the lower mantle, *Earth Planet. Sci. Lett.*, *190*(1), 57-63.

Ono, S., and A. R. Oganov (2005), In situ observations of phase transition between perovskite and CaIrO3-type phase in $MgSiO_3$ and pyrolitic mantle composition, *Earth Planet. Sci. Lett.*, *236*(3-4), 914-932.

Piet, H., J. Badro, F. Nabiei, T. Dennenwaldt, S.-H. Shim, M. Cantoni, C. Hébert, and P. Gillet (2016), Spin and valence dependence of iron partitioning in Earth's deep mantle, *Proc. Natl. Acad. Sci. USA*, 201605290.

Poirier, J.-P. (2000), *Introduction to the Physics of the Earth's Interior*, Cambridge University Press, Cambridge, England.

Pulliam, J., and M. K. Sen (1998), Seismic anisotropy in the core-mantle transition zone, *Geophys. J. Int.*, *135*(1), 113-128.

Reasoner, C., and J. Revenaugh (1999), Short-period P wave constraints on D″ reflectivity, *J. Geophys. Res. Solild Earth*, *104*(B1), 955-961.

Ringwood, A. E. (1975), *Composition and Petrology of the Earth's Mantle*, McGraw-Hill New York.

Ringwood, A. E. (1982), Phase transformations and differentiation in subducted lithosphere: Implications for mantle dynamics, basalt petrogenesis, and crustal evolution, *The Journal of Geology*, 611-643.

Ritsema, J., A. Deuss, H. Van Heijst, and J. Woodhouse (2011), S40RTS: a degree-40 shear-velocity model for the mantle from new Rayleigh wave dispersion, teleseismic traveltime and normal-mode splitting function measurements, *Geophys. J. Int.*, *184*(3), 1223-1236.

Ritsema, J., H. J. van Heijst, and J. H. Woodhouse (1999), Complex shear wave velocity structure imaged beneath Africa and Iceland, *Science*, *286*(5446), 1925-1928.

Robertson, G., and J. Woodhouse (1996), Ratio of relative S to P velocity heterogeneity in the lower mantle, *J. Geophys. Res. Solild Earth*, *101*(B9), 20041-20052.

Rost, S., E. J. Garnero, Q. Williams, and M. Manga (2005), Seismological constraints on a possible plume root at the core–mantle boundary, *Nature*, *435*(7042), 666-669.

Russell, S. A., C. Reasoner, T. Lay, and J. Revenaugh (2001), Coexisting shear- and compressional-wave seismic velocity discontinuities beneath the central Pacific, *Geophys. Res. Lett*, *28*(11), 2281-2284.

Sakai, T., E. Ohtani, H. Terasaki, N. Sawada, Y. Kobayashi, M. Miyahara, M. Nishijima, N. Hirao, Y. Ohishi, and T. Kikegawa (2009), Fe-Mg partitioning between perovskite and ferropericlase in the lower mantle, *Am. Mineral.*, *94*(7), 921-925.

Saltzer, R. L., E. Stutzmann, and R. D. van der Hilst (2004), Poisson's ratio in the lower mantle beneath Alaska: Evidence for compositional heterogeneity, *J. Geophys. Res. Solild Earth*, *109*(B6).

Sandercock, J. (1971), The design and use of a stabilised multipassed interferometer of high contrast ratio, paper presented at Proceedings of the Second International Conference on Light Scattering in Solids, 1Flammarion, Paris.

Schlaphorst, D., C. Thomas, R. Holme, and R. Abreu (2016), Investigation of core–mantle boundary topography and lowermost mantle with P4KP waves, *Geophys. J. Int.*, *204*(2), 1060-1071.

Sidorin, I., M. Gurnis, and D. V. Helmberger (1999), Evidence for a ubiquitous seismic discontinuity at the base of the mantle, *Science*, *286*(5443), 1326-1331.

Simmons, N. A., A. M. Forte, L. Boschi, and S. P. Grand (2010), GyPSuM: A joint tomographic model of mantle density and seismic wave speeds, *J. Geophys. Res. Solild Earth*, *115*(B12).

Sinmyo, R., K. Hirose, S. Muto, Y. Ohishi, and A. Yasuhara (2011), The valence state and partitioning of iron in the Earth's lowermost mantle, *J. Geophys. Res. Solild Earth*, *116*(B7).

Sinogeikin, S. V., and J. D. Bass (2000), Single-crystal elasticity of pyrope and MgO to 20 GPa by Brillouin scattering in the diamond cell, *Phys. Earth Planet. Inter.*, *120*(1-2), 43-62.

Sinogeikin, S. V., J. Zhang, and J. D. Bass (2004), Elasticity of single crystal and polycrystalline $MgSiO_3$ perovskite by Brillouin spectroscopy, *Geophys. Res. Lett*, *31*(6), L06620.

Speziale, S., A. Milner, V. E. Lee, S. M. Clark, M. P. Pasternak, and R. Jeanloz (2005), Iron spin transition in Earth's mantle, *Proc. Nat. Acad. Sci. U.S.A.*, *102*(50), 17918.

Su, W.-j., and A. M. Dziewonski (1997), Simultaneous inversion for 3-D variations in shear and bulk velocity in the mantle, *Phys. Earth Planet. Inter.*, *100*(1), 135-156.

Tackley, P. J. (2000), Mantle convection and plate tectonics: Toward an integrated physical and chemical theory, *Science*, *288*(5473), 2002-2007.

Tange, Y., Y. Nishihara, and T. Tsuchiya (2009), Unified analyses for P-V-T equation of state of MgO: A solution for pressure-scale problems in high P-T experiments, *J. Geophys. Res. Solild Earth*, *114*(B3).

Thomas, C., E. J. Garnero, and T. Lay (2004), High-resolution imaging of lowermost mantle structure under the Cocos plate, *J. Geophys. Res. Solild Earth*, *109*(B8).

Thomas, C., and M. Weber (1997), P velocity heterogeneities in the lower mantle determined with the German Regional Seismic Network: improvement of previous models and results of 2D modelling, *Phys. Earth Planet. Inter.*, *101*(1), 105-117.

Thomas, C., J. Wookey, J. Brodholt, and T. Fieseler (2011), Anisotropy as cause for polarity reversals of D″ reflections, *Earth Planet. Sci. Lett.*, *307*(3 – 4), 369-376.

Thorne, M. S., and E. J. Garnero (2004), Inferences on ultralow-velocity zone structure from a global analysis of SPdKS waves, *J. Geophys. Res. Solild Earth*, *109*(B8).

Tong, X. (2014), *Single-crystal elasticity of the lower-mantle ferropericlase* $(Mg_{0.92}Fe_{0.08})O$, University of Texas, Austin, Texas.

Trampert, J., F. Deschamps, J. Resovsky, and D. Yuen (2004), Probabilistic tomography maps chemical heterogeneities throughout the lower mantle, *Science*, *306*(5697), 853-856.

Tsuchiya, T. (2011), Elasticity of subducted basaltic crust at the lower mantle pressures: Insights on the nature of deep mantle heterogeneity, *Phys. Earth Planet. Inter.*, *188*(3), 142-149.

Tsuchiya, T., and J. Tsuchiya (2006), Effect of impurity on the elasticity of perovskite and postperovskite: Velocity contrast across the postperovskite transition in (Mg,Fe,Al)(Si,Al)$O_3$, *Geophys. Res. Lett.*, *33*(12), L12S04.

Tsuchiya, T., J. Tsuchiya, K. Umemoto, and R. M. Wentzcovitch (2004a), Elasticity of post-perovskite $MgSiO_3$, *Geophys. Res. Lett.*, *31*(14), L14603.

Tsuchiya, T., J. Tsuchiya, K. Umemoto, and R. M. Wentzcovitch (2004b), Phase transition in $MgSiO_3$ perovskite in the earth's lower mantle, *Earth Planet. Sci. Lett.*, *224*(3-4), 241-248.

Tsuchiya, T., R. M. Wentzcovitch, C. R. S. da Silva, and S. de Gironcoli (2006), Spin transition in magnesiowüstite in Earth's lower mantle, *Phys. Rev. Lett.*, *96*(19), 198501.

van der Hilst, R. D., and H. Kárason (1999), Compositional heterogeneity in the bottom 1000 kilometers of Earth's mantle: toward a hybrid convection model, *Science*, *283*(5409), 1885-1888.

Wang, X., T. Tsuchiya, and A. Hase (2015), Computational support for a pyrolitic lower mantle containing ferric iron, *Nature Geosci*, *8*(7), 556-559.

Weber, M., and J. Davis (1990), Evidence of a laterally variable lower mantle structure from P-and S-waves, *Geophys. J. Int.*, *102*(1), 231-255.

Wentzcovitch, R., J. Justo, Z. Wu, C. R. da SILVA, D. Yuen, and D. Kohlstedt (2009), Anomalous compressibility of ferropericlase throughout the iron spin cross-over, *Proc. Natl. Acad. Sci. USA*, *106*(21), 8447-8452.

Wentzcovitch, R., B. Karki, M. Cococcioni, and S. De Gironcoli (2004), Thermoelastic Properties of $MgSiO_3$-Perovskite: Insights on the Nature of the Earth's Lower Mantle, *Phys. Rev. Lett.*, *92*(1), 018501.

Wentzcovitch, R. M., B. B. Karki, S. Karato, and C. R. S. Da Silva (1998), High pressure elastic anisotropy of MgSiO3 perovskite and geophysical implications, *Earth Planet. Sci. Lett.*, *164*(1–2), 371-378.

Wentzcovitch, R. M., T. Tsuchiya, and J. Tsuchiya (2006), $MgSiO_3$ postperovskite at D″ conditions, *Proc. Natl. Acad. Sci. USA 103*(3), 543-546.

Wookey, J., S. Stackhouse, J.-M. Kendall, J. Brodholt, and G. D. Price (2005), Efficacy of the post-perovskite phase as an explanation for lowermost-mantle seismic properties, *Nature*, *438*(7070), 1004-1007.

Wu, X., J.-F. Lin, P. Kaercher, Z. Mao, J. Liu, H.-R. Wenk, and V. B. Prakapenka (2017), Seismic anisotropy of the D″ layer induced by (001) deformation of post-perovskite, *Nat. Commun.,8*, 14669.

Wu, Z., J. F. Justo, and R. M. Wentzcovitch (2013), Elastic anomalies in a spin-crossover system: ferropericlase at lower mantle conditions, in *Phys. Rev. Lett.*, edited, p. 228501.
Wu, Z., and R. M. Wentzcovitch (2014), Spin crossover in ferropericlase and velocity heterogeneities in the lower mantle, *Proc. Natl. Acad. Sci. USA*, *111*(29), 10468-10472.
Xu, S., J. F. Lin, and D. Morgan (2017), Iron partitioning between ferropericlase and bridgmanite in the Earth's lower mantle, *J. Geophys. Res. Solild Earth*, *122*(2), 1074-1087.
Yamazaki, D., and S.-i. Karato (2001), Some mineral physics constraints on the rheology and geothermal structure of Earth's lower mantle, *Am. Mineral.*, *86*(4), 385-391.
Yamazaki, D., and S.-i. Karato (2002), Fabric development in (Mg,Fe)O during large strain, shear deformation: implications for seismic anisotropy in Earth's lower mantle, *Phys. Earth Planet. Inter.*, *131*(3–4), 251-267.
Yang, J., J. F. Lin, S. D. Jacobsen, N. M. Seymour, S. N. Tkachev, and V. B. Prakapenka (2016), Elasticity of ferropericlase and seismic heterogeneity in the Earth's lower mantle, *J. Geophys. Res. Solild Earth,121*(12), 8488-8500.
Yang, J., Z. Mao, J.-F. Lin, and V. B. Prakapenka (2014), Single-crystal elasticity of the deep-mantle magnesite at high pressure and temperature, *Earth Planet. Sci. Lett.*, *392*, 292-299.
Yang, J., X. Tong, J.-F. Lin, T. Okuchi, and N. Tomioka (2015), Elasticity of ferropericlase across the spin crossover in the Earth's lower mantle, *Sci. Rep.*, *5,*1788.
Yeganeh-Haeri, A. (1994), Synthesis and re-investigation of the elastic properties of single-crystal magnesium silicate perovskite, *Phys. Earth Planet. Inter.*, *87*(1), 111-121.
Zhang, J., and T. Lay (1984), Investigation of a lower mantle shear wave triplication using a broadband array, *Geophys. Res. Lett.*, *11*(6), 620-623.